UNIVERSITAT POLITÈCNICA DE CATALUNYA
BARCELONATECH
Departament de Teoria del Senyal
i Comunicacions

Terahertz Integrated Antenna Arrays for Imaging Applications

Author
Maria Alonso del Pino

Thesis Advisors
Lluís Jofre Roca
Nuria Llombart Juan

A thesis submitted to the Universitat Politècnica de Catalunya (UPC)
in partial fulfillment of the requirements for the degree of
DOCTOR OF PHILOSOPHY

Ph.D. program on Signal Theory and Communications
AntennaLab Group
Barcelona, September 2013

Thesis written by Maria Alonso del Pino

THz Integrated Antenna Arrays for Imaging Applications

Ph.D. program on Signal Theory and Communications

The work presented in this thesis has been supported in part by the Spanish Interministerial Commision on Science and Technology (CICYT) under projects TEC2007-66698-C04-01, TEC2010-20841-C04-02 and CONSOLIDER CSD2008-68.

Only when you see the invisible
you can do the impossible.

– Frank Gaines

Abstract

Terahertz is the portion of the spectrum that covers a frequency range between 300 GHz - 3 THz. This frequency band has proven its potential for imaging applications thanks to the good compromise between spatial resolution and penetration; however, this push towards high frequencies contains many technological difficulties in all the subsystems involved in the signal generation, transmission and detection. The power budget restrictions and high losses that sources and receivers currently suffer at these frequencies require systems with a high level of integration among all the devices and components of the systems and subsystems. Therefore, the antennas needed for these systems require to be integrated within the same fabrication processes and technologies as the sensing and power converting devices that are used at their terminals.

This doctoral thesis has focused on the development of integrated antenna arrays at Terahertz frequencies for imaging applications, for both near-field and focal-plane geometries, with a special emphasis on the technologies and the fabrication capabilities that can be potentially used and are currently available. The current imaging systems require large arrays of antennas in order to achieve the high-speed image acquisition that is required in most THz applications. This fact increases considerably the difficulty and complexity to achieve highly integrated and efficient antennas. This thesis has characterized and analyzed these difficulties and provided solutions to the development of antenna arrays at millimeter and submillimeter wave frequencies.

The first part of this thesis has focused on the study of a planar antenna array, called retina, for a specific near-field imaging system based on the Modulated Scatterer Technique (MST) at millimeter and submillimeter-wave frequencies. This system has been selected for its capabilities to perform high-speed imaging and because it does not require a high frequency distribution line network. However, it is hindered by many technological difficulties: the selection of an antenna geometry that achieves high efficiency, the selection of the adequate active element and its integration with the antenna. In this thesis, these challenges have been addressed and studied in-depth, and a design methodology that integrates all the different aspects of the system has been developed. Because planar antennas at millimeter and submillimeter wave frequencies suffer from high losses due to the surface wave modes inside substrate, these losses have been analyzed and quantified for different antennas, and an antenna geometry that reduces significantly this problem has been developed. Different switching technologies currently or potentially available at these high frequencies have been considered in order to study and analyze their capabilities and their integration possibilities: PIN diodes, Schottky diodes and RF-MEMS.

These technologies have been studied through the development of three retina prototypes, which have been fabricated using high precision fabrication processes such as laser micromachining and photolithographic. Different measurement set ups were fabricated and assembled to validate the different premises presented.

The second part of the thesis is devoted to the study of integrated Focal Plane Arrays (FPA). The development of FPA at submillimeter wave frequencies is highly on demand due to the enormous progress in designing integrated heterodyne receivers. These receivers integrate arrays of submillimeter-wave diode-based mixers and multipliers with Monolithically Integrated Circuit (MIC) amplifiers on the same wafer stack. For this stackable multi-pixel terahertz camera technology to work, a leaky wave antenna with silicon micro-lenses has been developed, which allows wafer level integration compatible with silicon micro-fabrication techniques for bulk array manufacturing and has high directivity in order to illuminate a reflector efficiently. Detailed and thorough design guidelines for this antenna are presented. Two antenna prototypes were built in order to evaluate the two fabrication possibilities: advanced laser micro-fabrication and photolithographic fabrication. A study of the aberrations of the lens has been developed in order to evaluate the performance of the lens profile fabricated. Moreover, a set of radiation pattern measurements of the fabricated prototypes was performed in order to evaluate the performance of the antenna and its possibilities to be used as a FPA.

Preface

This doctoral thesis comprises the research performed by the author within the AntennaLab group of the Signal Theory and Communications Department (TSC) of the Universitat Politècnica de Catalunya (UPC). I would like to acknowledge the many people that have contributed to this thesis through their support, collaboration, work and advice.

First and foremost, I would like to thank Prof. Lluís Jofre for giving me the opportunity to work on this doctoral thesis under the framework of the TeraSense project; and also for his trust in my work and his advice.

I especially want to express my sincere gratitude to Prof. Nuria Llombart for her unconditional support and advice during these years. Her contribution and expertise have been essential for the development of this research.

I would like to thank and acknowledge the following for their contribution to this thesis: for their help and contribution with the Schottky characterization, Prof. Thomas Bryllert from Chalmers University; for their assistance and support with the RF-MEMs fabrication process, Prof. Bedri Cetiner, Dr. Mehmet Unlu and Dr. Yassin Damgaci from Utah State University; and for their collaboration and support with the micro-lens design and fabrication process the SWAT team of the Jet Propulsion Laboratory.

I would like to acknowledge the occasional support received from the professors of the Signal Theory Department, especially Prof. Jordi Romeu and Prof. Antoni Broquetas; the laboratory technicians, Joaquim Giner, Josep Pastor, Ruben Tardio and Albert Marton; and the administrative staff, Teresa Pons and Aynie Khoe.

I would also like to thank my colleagues of the department for their continuous support, practical help and the good moments spent: Enrique Nova, Marta Guardiola, Dani Rodrigo, Gemma Roqueta, Marc Imbert, Edgar Diaz, Jordi Balcells, Jordi Abril, Bea Monsalve and Raquel Serrano. Special thanks go to Santiago Capdevila for the time shared, his generous help and discussions.

On a more personal note, I give thanks to my parents and friends for their unconditional emotional support. And last but not the least, special thanks go to Agnès for her support and contributions in the final corrections and touches of the thesis.

Contents

1

Chapter 1
Introduction

Terahertz is the portion of the spectrum that covers a frequency range between 300 GHz - 3 THz (it is extended from 100GHz to 10THz by some authors). This portion, sometimes referred as THz Gap, falls in between two mature and highly technologically developed spectral bands: the microwaves and the optical regime. There are two main approaches that have been adopted to fill this gap. One approach is to up-scale the technology developed in microwaves, where the aim is to detect the electromagnetic field of a propagating wave using an antenna. The other solution is to down-scale the developed optics technology where the power of the phonon radiation is measured. New developments of nanotechnology and photonics, specially with the combination and melding of these two technologies and viewpoints, have led to many technology advances in the terahertz range, mitigating the gap between both [1].

In comparison with microwaves, infrared and optical bands where its applications and technologies are already highly developed and well-known, terahertz technology has still not deeply been investigated and it is still captivating and attracting new members in the scientific community [2]. During the past decade, with the advancement of various

THz technologies, sensing and imaging have impacted a broad range of interdisciplinary fields, in particular: security, with the ability of detecting concealed weapons, explosives or drugs [3]; biomedical, where imaging and spectroscopy play an important role [4]; astronomy and space exploration, with the study of the universe and its origin [5].

1.1 Terahertz Imaging Systems

The THz frequency band has proven its potential for imaging applications thanks to the good compromise between spatial resolution and penetration. The enabler of this development is the advancement of different technologies capable of generating or detecting THz radiation. The current technology for THz generation or detection is based on either pulsed time domain or frequency domain systems.

Time domain systems cover the broad THz spectra by the use of a laser pulse radiating into a photo conductive antenna. The sampling of the pulse is performed in the time domain and therefore the spectrum is recovered in amplitude and phase. There are different types of photoconductive switches available based in different technologies; however, photoconductive (Auston) switches are increasing popularity. They produce high bandwidth radiation, though it requires expensive apparatus and the power provided is still very low. These systems are commonly employed when it is required to perform imaging for processes that occur very fast in time, for example, of chemical reactions.

Frequency domain systems can be characterized as the ones that use microwave technology in the form of radiometers (commonly implemented using direct detectors), active heterodyne transceivers or the photo-mixing of two lasers. Direct detector devices such as bolometers [6], Golay cells [7], Kinetic Inductance Detectors (KIDs) [8], etc. are able to measure the power of the THz radiation (incoherent detection) and cryogenic cooling is required among the most sensitive detectors. The common photo-mixing lasers employed are the Quantum Cascade Laser (QCL); photo-mixing is done by mixing two CW lasers into a photoconductive antenna. They provide a single sharp laser line with a relatively cheaper technology; however, it currently requires cryogenic cooling. Heterodyne receivers, on the other hand, are capable of retaining amplitude and phase of the transceivers fields (coherent detection) offering a great advantage for imaging applications because they open the possibility for modulating the signal and doing three dimensional and tomographic imaging. These transceivers consist mainly of a mixer which multiplies the incoming radiation with a reference frequency that is afterwards filtered to extract the intermediate frequency. There are different mixer technologies currently available such as Schottky diodes [9], Superconductor Insulator Superconductors (SISs) [10], Hot Electron Bolometers (HEBs) [11], etc. Schottky diodes are currently the mixers leading to the lowest noise without the need of cryogenic cooling. This thesis is going to be focused on imaging systems that require non-cryogenic diodes as they can be potentially integrated with Monolithic Integrated Circuits (MIC) in order to perform commercial systems. Moreover, it will also concentrate in active systems (a source will be used to illuminate the target and collect the reflection from the object) in order to perform three dimensional tomographic imaging.

Considering the power budget restrictions and high losses that sources and receivers suffer at these frequencies it is important to achieve a high level of integration among all

the devices of the systems in order to avoid unnecessary additional losses. MIC can be referred as one of the key technological achievements of the last decade because of the ability to integrate multifunction analog as well as digital circuits on a single chip to improve performance and reduce the size of electronic devices. Specifically from the antenna point of view, it is important that the antennas can be fabricated and integrated in the same fabrication process as the sensing or power converting devices that are used at their terminals [12]. Moreover, realizing specific impedance matching, frequency bandwidth and high efficiencies remain also significant challenges.

The antenna topology requirements can be broadly classified into two different areas depending on what type of imaging system topology we are aiming for:

- **Near-field imaging systems.** These systems perform the imaging within the near-field region of the imaging system. The system is located at a distance closer than the Fraunhofer (the Fraunhofer distance is defined as $2D^2/\lambda$, where D is the main dimension of the imaging system antenna and λ is the wavelength) from the object. These near-field systems are designed with non-directive antennas, i.e. antennas in the order of half wavelength. The main reason is that these systems require that the antenna itself does not perturb the response of the sample being imaged. The imaging resolution of these systems is not dictated by the antenna's dimensions, but by the Nyquist sampling of the received field (usually in the order of half wavelength).

  Near-field systems are widely used at microwave frequencies like in [13, 14] and the antennas employed are planar antennas. When scaling these antennas to the THz frequencies, the substrates become too thin and fragile to fabricate or if they are not scaled, they suffer from high losses due to the trapped surface waves inside.

- **Far-field imaging systems.** These systems perform the imaging within the far-field region, which goes from the Fraunhofer distance all the way to infinity. Big optical systems employing reflectors or lenses are commonly used to achieve the proper resolution. High directivity is required for the antennas that feed these optics.

  In the submillimeter wave band, conductor materials suffer from high losses. Therefore, phased arrays are rarely seen. The typically employed antennas for illuminating these optical systems are lenses or horns. Lenses suffer from multiple internal reflections because of the use of high dielectric materials. Horns represent a challenge to fabricate. While in microwaves traditional fabrication methods of milling and turning are still used, at THz frequencies, horns become very small structures and machines with much higher accuracy are needed, increasing the cost significantly.

The image acquisition time for both types of systems is directly proportional to the number of receiving antennas. Thus, large arrays of antennas will be required in order to fulfill the incoming requirements of high speed image acquisition of future THz imaging systems [15]. Such large arrays increase considerably the difficulty and complexity of the overall process in terms of integration and fabrication of the antennas. All in all, these constraints are forcing the investigators towards new or simplified forms of traditional antennas, towards a large variety of new planar antennas (i.e designed to take advantage of wafer scale integration) and towards new fabrication technologies, in order to provide high integrated and high efficiency antenna arrays.

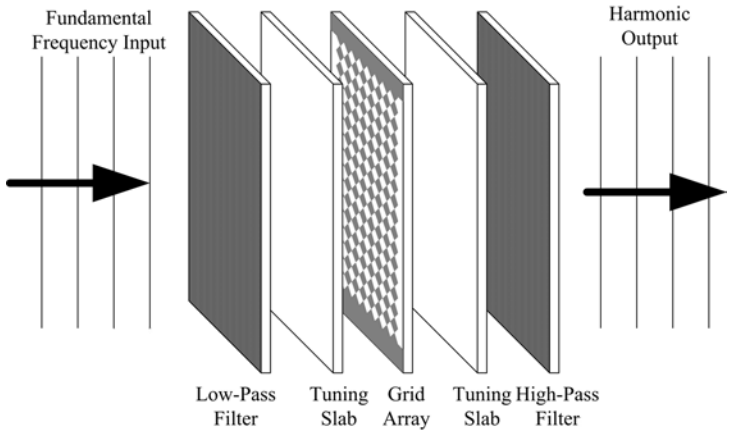

Figure 1.1: Sketch of a frequency doubler from 500 GHz to 1 THz from Rutledge [16].

1.2 State of the Art in Terahertz Integrated Arrays

This section will introduce the state of the art of the current arrays of integrated antennas that can be found at THz frequencies. The arrays can be divided into two main technology areas as it has been introduced in the previous section: non directive arrays and directive arrays corresponding to near-field and far-field imaging systems, respectively.

1.2.1 Non-Directive Antenna Arrays

Non-Directive antenna arrays where each of the antennas operate independently from the others are usually referred in the literature as antenna grids [16–18]. They are compounded of multiple non directive antennas, i.e. planar slots or dipoles. In the submillimeter wave band, these antenna grids are used to sample a plane wave (usually in the form of a collimated field in practical systems) and perform a certain active function on this field. This function can be a modulation, amplification or a mixing of two fields [16, 18, 19].

These arrays do not contain a feeding network that combines the signal coming from all the antennas into a single port, but instead, an active component is integrated directly on each of the antenna output terminals [16, 17]. This method avoids the high losses and fabrication problems associated with waveguide structures at THz. A maximum spacing between elements of $\lambda/2$ is required to accomplish the Nyquist sampling theory necessary to recover the image information from the target. In the microwave regime, these antennas are usually fabricated in thin substrates or surrounded by metallic pins in order to avoid the excitation of substrate modes. This integration is critical at high frequencies in order to avoid the high ohmic losses associated with transmission lines.

Figure 1.1 shows an sketch of a frequency doubler published by Rutledge [16]. The grid array is composed of dipole antennas loaded with Schottky diodes in a GaAs substrate of 30 μm thick delivering a frequency of 1 THz for an input frequency of 500 Ghz. It is also a good example of how quasi-optics technology can blend with microwave technol-

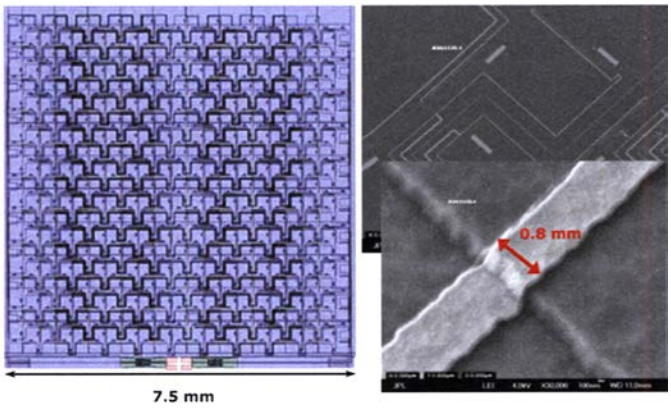

Figure 1.2: (Left) Layout of the array (Right) picture of the fabricated array from [20]

ogy allowing the combination of output powers of many amplifiers in free space without significant ohmic losses.

1.2.2 Directive Antenna Arrays

The directive antenna arrays found at submillimeter wave band are based on phased arrays, horns and lenses. These antenna arrays are commonly used to illuminate an optical system like a reflector.

1.2.2.1 Phased Arrays

Phased arrays are able to achieve high gain in the THz band only when the feeding network is made of a superconducting material. These superconducting lines avoid conductor losses, so significant at these high frequencies. The superconducting effect occurs only below the superconducting frequency gap of the material and this gap frequency depends on the actual material. Moreover, these antennas can be fabricated with lithographic techniques and therefore easily fabricated in large arrays.

In [20] an example of a phased array of a dual polarization slot antenna fabricated with superconducting lines is presented (see Figure 1.2). The same microstrip made of a regular conductor would have a -5 dB loss for a length of just $\lambda/2$.

However, this material requires cryogenic cooling in order to operate as a superconducting material. Because this thesis focuses on non cryogenic imaging systems, these antennas will not be suitable for our purposes.

1.2.2.2 Horn Arrays

While horn arrays are typically used at microwaves, there are only few examples at THz frequencies, specially above 300GHz. This is because the fabrication of horn arrays is complex and requires high precision methods. The most common horn arrays are found

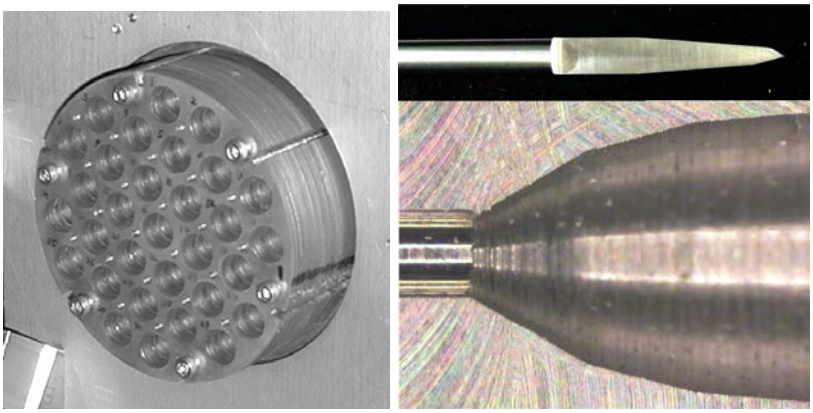

Figure 1.3: (Left) 31-pixel 100 GHz platelet array prototype shown in [21]. (Right) Machine tool used for the horn drilling (top) and side view a half drilled horn (bottom) from [22] (the input waveguide on the left has a diameter of 1.24 mm).

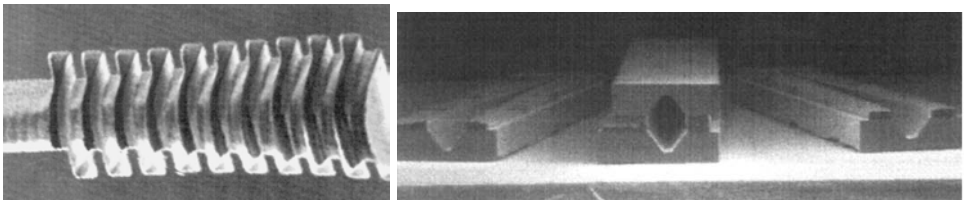

Figure 1.4: (Left) SEM photograph of a 2 THz corrugated feed horn milled with laser micro-fabrication from [23]. (Right) SEM photograph of a 585 GHz pyramidal horn fabricated using silicon etching at 35 degree angle from [23].

at the lower end of the terahertz band and are typically fabricated using micromachining techniques. High precision milling techniques have been proposed in [21,22]. One example is shown in Figure 1.3(Left), where a W-band corrugated horn array is presented. It is formed by bass plates milled holes using a Computer Numerical Control (CNC) machine and stacked together with screws and pins [21]. A similar approach relies on a drilling technique that has control of the flare-angle in order to provide smooth-walled horns [22]. This technique uses a custom drill bit (see the top figure of Figure 1.3(Right)) to fabricate a multiple flare-angle horn (see the bottom figure of Figure 1.3(Right)).

An emerging fabrication technique that has allowed the fabrication of horns at higher frequencies is a silicon micro-machining laser [23]. This technique uses a computer-controlled argon-ion laser that locally heats a portion of a silicon substrate in a chlorine environment. The melted silicon reacts to the chlorine and it is removed from the substrate. For example, Figure 1.4(Left) shows a corrugated horn fabricated using this process and it is suitable for operating at 810 GHz and 2 THz [23].

In order to reduce the cost and time of the fabrication of large arrays of horns using laser micro-fabrication, techniques based on photolithographic processes are a better option [23]. There are two different approaches that researchers are following:

Figure 1.5: (Left) View of silicon platelets before the gold metallization and (Right)view of the fabricated array of horns from [24]

- One approach is to use of selective etching silicon techniques to fabricate pyramidal horn antennas as proposed by [23]. It consists on using photolithographic processes to etch a pair of silicon wafers at 35 degrees (silicon can only be etched in a 90 or 35 degree angle due to the crystal structure). After applying a gold platted layer on the silicon both wafers are assembled together. Lubecke in [23] shows an example of pyramidal antennas suitable for working at 585 GHz (see Figure1.4(Right)). However, horns fabricated with a 35 degree angle have low directivity and therefore they would not be suited for instance as a Focal Plane Array (FPA) where directive antennas are required.
- Another approach is to stack thin gold plated silicon wafers with tapered holes etched at 90 degree angle. An example is shown in [24] where an array of 84 corrugated horns with an aperture diameter of 55 mm working at 130 to 170 GHz has been fabricated and measured (see Figure 1.5). The tapered holes are obtained by applying a deep reactive ion etch (DRIE) to the silicon wafers achieving vertical sidewalls. This technique is strongly limited by the tolerances of the fabrication process. This tolerance depends on the photolithographic process, the number of wafers employed and the alignment process of those wafers. Consequently, the larger the directivity, the longer the horn and the larger the number of wafers. Since the tolerance problem is related to the excitation of higher order modes in the horn and this process is accumulative, the larger the number of the wafers, the tighter the tolerances need to be.

All in all, even by using photolithographic processes, there has not been developed an integrated and efficient method to fabricate arrays of horns. Simpler antenna designs made of a small number of wafers are required in order to reduce the impact of the alignment tolerances that occur when a high number of wafers are used.

1.2.2.3 Lens Arrays

Integrated lens antennas are the most suited antennas for THz applications for their focusing capabilities and fabrication techniques for manufacturing. Even though at THz it is common the adoption of single lenses as a focusing element for a single detector,

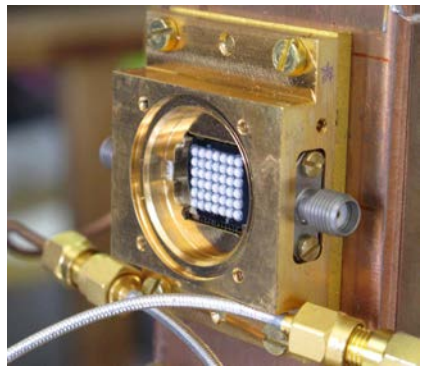

Figure 1.6: Forty-two elements array of sapphire ball lenses at 350 GHz from [25].

it is still hard to see them in large arrays. There are a few examples of lenses arrays fabricated at THz as in [25] where every lens is assembled manually (one by one). Figure 1.6 shows an example of an array found in [25] of 42 (6x7) sapphire ball lenses coupled to an array of Kinetic Inductance Devices (KIDs) placed in the focal plane array of the IRAM telescope [26] working at 350 GHz.

1.3 Thesis Goal

In this past section, several restrictions from the antenna point of view have been identified that currently limit the size and the electromagnetic performance of arrays of antennas at terahertz frequencies. The goals of this doctoral thesis are mainly divided into two parts, both of them leading to the study of integrated antenna arrays for imaging applications. The objectives are divided as follows:

- **Integrated Planar Antenna Arrays**

  This research has focused in the study of an integrated planar array called retina for a near-field imaging system. This retina consists of an array of antennas printed on an electrically thick substrate. The array antenna element is designed to cancel the surface waves that propagate within this substrate and also to be integrated with the rest of elements in the system.

  The imaging system is based on a near-field Modulated Scatterer Technique (MST) system. This system has been characterized and general formulation and quality parameters have been defined. An assessment of different technologies available for the fabrication of the antenna arrays has been studied and different approaches have been followed.

  The main research including the design and fabrication of the prototypes has been conducted primarily at the Universitat Politecnica de Catalunya (UPC). One of the array prototypes which is based on an antenna with Radio-Frequency Micro-electromechanical Systems (RF-MEMS) device integrated was carried out in close collaboration with the Utah State University (USU), USA, and its fabrication was carried out at Cornell Nanoscale Science and Technology Facilities (CNF), USA.

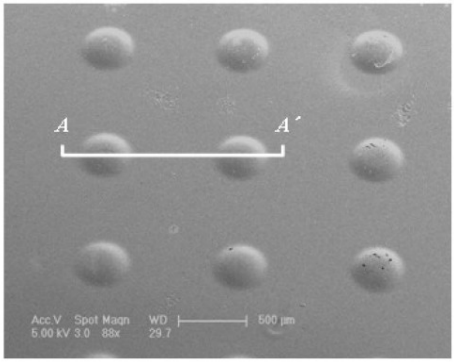

Figure 1.7: SEM image of a fabricated micro-lens array of 500 μm diameter from [30].

Another prototype based on antenna with Schottky diodes was carried out in close collaboration with Chalmers University, Sweden.

- **Integrated Focal Plane Antenna Arrays**

  This research is a joint collaboration with the Jet Propulsion Laboratory (JPL), USA. The goal is to design an array of high number of antennas to be used as a FPA of a reflector, and consistent with the silicon fabrication capabilities and technologies that are currently being developed at JPL.

  The idea was to provide simple antenna designs made of a small number of wafers in order to reduce the impact of the alignment tolerances (specially in the case of horns) that could be integrated in an array of detectors fed by waveguides.

  One approach considered was to design and to fabricate an array of horn antennas by stacking gold plated silicon wafers with tapered holes. But in this case, the silicon is selectively etched with a 5 degree angle (instead of 35 or 90 degree). This etching allowed a reduction in the total number of wafers and therefore an improvement of the wafer alignment tolerances. This technique was still in an early stage of development and an improvement in this angle controllability was required. The idea was briefly presented in [27] but it has not been developed further.

  The approach followed in this thesis was the design and fabrication of an array of silicon lenses antennas. The whole antenna is designed to be consistent with two fabrication processes developed: one based on silicon laser micro-machining and another using silicon photolithographic micro-machining. Silicon laser micro-machining was already used in [28] and [29] to fabricate hemispherical lenses. And on the other hand, silicon photolithographic micro-machining is a technique used in the optics regime like in [30]. In Figure 1.7 an array of 500 μm diameter lenses fabricated using this method is shown. In this thesis the goal is to explore its capabilities at THz frequencies.

1.4 Thesis Outline

The main contents of this thesis are divided in seven chapters including the concluding chapter. The contents of each chapter are summarized as follows:

Part I studies an array of antennas suited for a near-field imaging system based on MST.

Chapter 2 begins with an introduction and background of the near-field imaging system that has been studied in this thesis. The chapter provides a full characterization of the overall system and how each element is optimized to obtain a maximum response. It concludes with the study of the images that were obtained with the system and provides different imaging techniques that enhance its performance.

Chapter 3 shows the different prototypes that have been designed, built or that are currently under development based on the design guidelines provided in Chapter 2. Three prototypes are shown: a retina prototype working at 100 GHz using PIN diodes, one element probe antenna characterization at 300 GHz using Schottky diodes and a 2-D retina prototype using RF-MEMS. The fabrication and measurements performed of these prototypes are included also in this chapter at the end of each prototype section.

Part II studies an array of antennas suited for far-field imaging, specifically in FPAs.

Chapter 4 characterizes the design of an antenna that is consistent with silicon micromachining techniques and can be integrated in a FPA. The design guidelines of each part of the antenna are studied item by item.

Chapter 5 models an array of antennas working as a FPA for an imaging system. A theoretical description and simulations are developed to provide the antenna requirements. This theoretical study is performed assuming different aperture illumination of the FPA. The overall FPA design and the performance in the system is evaluated for the antenna described in chapter 4.

Chapter 6 presents the antenna prototypes fabricated, the fabrication process and measurements. The tolerance and performance of the fabrication techniques are evaluated as well as their impact in the antenna performance.

Chapter 7 shows the main conclusions that have been obtained from this work. Possible future developments and research lines are drawn as a continuation of this thesis.

An appendix with additional information is included at the end of the thesis as well as a complete list of the general bibliography and the publications from the author.

Part I

Integrated Planar Antenna Arrays

2

Chapter 2
Planar Antenna arrays for Near-Field Imaging Systems

This part of the thesis studies the design of a planar antenna array for a specific near-field imaging system at submillimeter-wave frequencies. In a near-field imaging system, the key is to sample a sufficient number of scattered field values in space to obtain a good estimation of the existing scattered field distribution necessary to recover the currents induced inside the object produced by the incident or illuminating field. This electromagnetic field sensing requires the use of probe antennas that minimize distortions in the measured field. A well known technique to sample field distributions is the MST. This technique was first introduced in 1955 [31, 32] to perform indirect measurements of the electric field distribution . It consisted on measuring the field distribution by observing a scattered field of a probe placed at a certain position. In order to discriminate the field scattered by the probe from others, the scattering properties of the probe are modulated during the time of the measurement. Originally, this modulation was generated by a

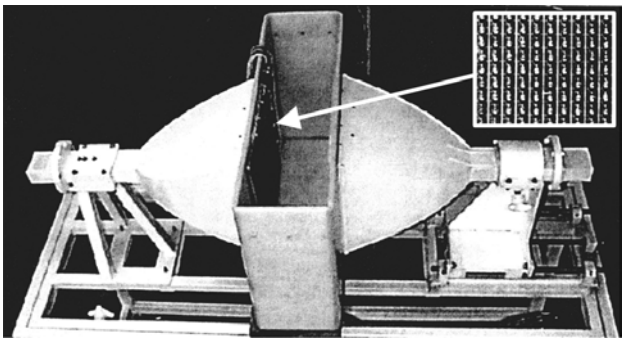

Figure 2.1: Microwave camera working at 2.45 GHz presented in [38]

mechanical rotation or a displacement of the probe, which limited the applicability of the technique. An alternative and now more commonly employed technique is the loading of the probe with some electronic device with two differentiated impedances by using a PIN diode [32] or a photodiode [33].

In the early developments, a single probe was used to perform the measurements. Later on, the development of arrays of MST probes called retina reduced the measurement time, allowing the development of fast antenna radiation pattern measurement systems [34] and the development of real-time microwave cameras that can be used in material characterization [35] or tomography applications [36, 37]. Figure 2.1 shows a photograph of the setup of a microwave camera and a photograph inset of the retina working at 2.45 GHz from [38].

The push towards higher frequencies pursued in this thesis is hindered by many technological difficulties in all the subsystems involved in the generation, transmission and detection of signals, making very difficult to attain a sufficiently high Signal to Noise Ratio (SNR) for tomography imaging. This system has been chosen because of its capabilities to perform high speed imaging, the absence of microwave transmission line distribution networks, and technology available at such frequencies. This system will be employed to evaluate and study the design and fabrication of planar antenna arrays (retina) at THz frequencies.

The retina is usually a planar antenna array which is compounded of non-directive antennas, where each antenna operates independently from the others, placed over a dielectric substrate. The major existing problem at submillimeter wave frequencies regarding the antenna efficiency is associated with this dielectric substrate. While in microwaves the substrate thickness is by far below the size of a wavelength, at millimeter and submillimeter wave frequencies the substrates available have a thickness in the order of the wavelength, and a substantial power loss appears, degrading the overall antenna efficiency.

This chapter is divided as follows: the next section presents the near-field imaging system and its key design parameters; it is followed by the analysis and characterization of the retina; after that, the efficiency of planar antennas associated with the surface-wave propagation within the substrate is studied; last, the tomographic imaging algorithm and its imaging capabilities are presented.

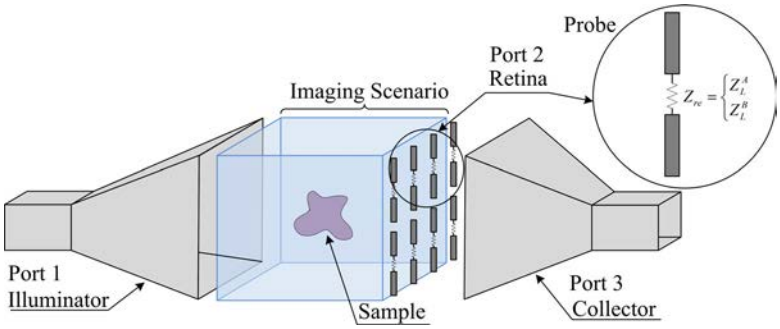

Figure 2.2: Scheme of the system proposed.

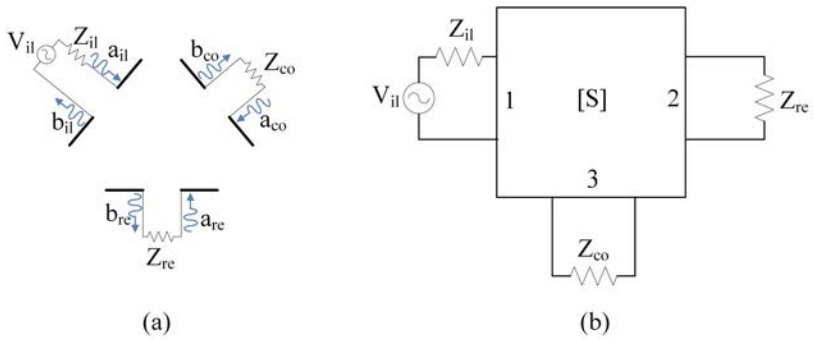

Figure 2.3: Three port scenario of the system proposed.

2.1 Near-Field Imaging System Design

As it has already been introduced, in order to evaluate the performance of these planar arrays, a near field imaging system based on MST has been designed (see Figure 2.2). This technique consists on illuminating the target with an antenna which will be called illuminator and measure its scattered field along a probing plane or also called retina. The retina reradiates this field to another antenna that will be called collector, which gather all the fields. Because each probe of the retina is modulated at a different low frequency, the signal received at each probe can be retrieved. A switching element is placed in each probe antenna port and provides two different load impedances to the probe antenna (each of the two possible states of the switching element will be referred as A or B states).

There are two main advantages of this system. First, the obtention of a multi-pixel image using a single high frequency receiver which increases the acquisition time of the image. The second advantage is the absence of microwave line distribution networks in the system which reduces the conductor losses that are so significant at THz frequencies.

In this section the quality parameters that are required to design an efficient near-field imaging system at millimeter and submillimeter wave frequencies are presented. For the design simplicity and controllability we are performing the study for a one element retina

within a known scenario. The scenario consists in the scheme of Figure 2.3 where the three basic elements of the system (illuminator, retina and collector) are modeled as a three-port system [39]:

$$b = \begin{pmatrix} b_{il} \\ b_{re} \\ b_{co} \end{pmatrix} = \begin{pmatrix} S_{11} & S_{12} & S_{13} \\ S_{21} & S_{22} & S_{23} \\ S_{31} & S_{32} & S_{33} \end{pmatrix} \begin{pmatrix} a_{il} \\ a_{re} \\ a_{co} \end{pmatrix} = \boldsymbol{S}\, a \tag{2.1}$$

where a_i is the power wave incident upon the port i; b_i is the power wave reflected or received at the port i; and S_{ij} is the S-parameter between ports i and j. Port 1 is the illuminator port represented by the subindex il; port 2 is the retina port which corresponds to the subindex re; and port 3 is the collector port represented by the subindex co.

The optimization of the reflection coefficient from the illuminator to the collector in order to provide the maximum power to the receiver is usually the most common technique for maximizing the performance of a system. However, in this system, the key parameter of the system performance will be obtained by coherently subtract the received power at the collector when the probe is loaded in each state impedance (Z_L^A and Z_L^B). This parameter defined as the differential transmission coefficient $\Delta\tau$ will determine the SNR of the system and the dynamic range of the image ($SNR = P_S - P_N - \Delta\tau$ being P_S the signal power and P_N the noise level). In this case:

$$\Delta\tau_{co,il} = \left|\tau_{co,il}^A - \tau_{co,il}^B\right|^2 \tag{2.2}$$

where $\tau_{co,il}^A = \frac{b_{co}}{a_{il}}|_{Z_{re}=Z_L^A}$ is the amount of power received at the collector relative to the power input of the illuminator when the probe is loaded in state A; and $\tau_{co,il}^B = \frac{b_{co}}{a_{il}}|_{Z_{re}=Z_L^B}$ is the amount of power received at the collector relative to the power input of the illuminator when the probe is loaded in state B. $\Delta\tau$ is maximized when τ_A and τ_B are in phase opposition and it is bounded by $0 \leq \Delta\tau_{co,il} \leq 1$, being the maximum value $\Delta\tau_{co,il} = 1$ (or 0 dB).

2.2 Retina Design

The retina is a planar array of N probe antennas fixed against the collector aperture. The maximum spacing between probes is $\lambda/2$ to properly sample the scattered field distribution according to the Nyquist theorem. As it has been previously introduced, each probe is composed of an antenna of impedance Z_T with a switching element of impedance Z_{re} that produces the low frequency modulation by changing the impedance between two states A and B ($Z_{re} = Z_L^A$ and $Z_{re} = Z_L^B$ respectively).

From the previous section, it is straightforward to consider the differential transmission coefficient as the representative index of this MST system. In order to understand the implications of this parameter in the design of the retina, this formulation is developed applying reciprocity. Considering a matched illuminator at port 1 ($Z_{il} = Z_0$) and a matched collector at port 3 ($Z_{co} = Z_0$), equation 2.1 can be developed into:

$$b = \boldsymbol{S}\begin{pmatrix} a_{il} \\ \rho_L^i b_{re} \\ 0 \end{pmatrix} = \boldsymbol{S}\begin{pmatrix} a_{il} \\ 0 \\ 0 \end{pmatrix} + \boldsymbol{S}\begin{pmatrix} 0 \\ \rho_L^i b_{re} \\ 0 \end{pmatrix} \tag{2.3}$$

defining the reflection coefficient of the switching impedance as $\rho_L^i = \frac{Z_L^i - Z_0}{Z_L^i + Z_0}$, being $i = A, B$ the state A and B of the switching element. Then, developing equation 2.3:

$$b = \left[I - \boldsymbol{S}\, diag\begin{pmatrix} 0 & \rho_L^i & 0 \end{pmatrix}\right]^{-1} \boldsymbol{S}\begin{pmatrix} a_{il} \\ 0 \\ 0 \end{pmatrix} = \frac{a_{il}}{1 - \rho_L^i S_{22}}\begin{pmatrix} S_{11} + \rho_L^i S_{21} \\ S_{21} \\ \rho_L^i S_{32} + S_{31} \end{pmatrix} \tag{2.4}$$

Next, the transmission coefficient in the i state can be defined as:

$$\tau_{co,il}^i = \frac{b_{co}}{a_{il}} \mid_{Z_{re}=Z_L^i} = S_{31} + \frac{S_{32}S_{21}\rho_L^i}{1 - \rho_L^i S_{22}} \tag{2.5}$$

Taking the difference of the transmission coefficients:

$$\Delta\tau_{co,il} = \tau_{co,il}^A - \tau_{co,il}^B = S_{31} + \frac{S_{32}S_{21}\rho_L^A}{1 - \rho_L^A S_{22}} - S_{31} + \frac{S_{32}S_{21}\rho_L^B}{1 - \rho_L^B S_{22}} \tag{2.6}$$

Finally, the final expression of the $\Delta\tau_{co,il}$ can be defined

$$\Delta\tau_{co,il} = S_{32}S_{21}\frac{\rho_L^A - \rho_L^B}{(1 - \rho_L^A S_{22})(1 - \rho_L^B S_{22})} = S_{32}S_{21}\frac{(Z_T + Z_0)^2}{2Z_0}\frac{Z_L^A - Z_L^B}{(Z_T + Z_L^A)(Z_T + Z_L^B)} \tag{2.7}$$

As it can be observed, $\Delta\tau_{co,il}$ can be fragmented in the different elements of the systems, i.e the Z_T which is the impedance of the physical probe antenna, Z_0 which are the impedances of the illuminator and collector, Z_L^A and Z_L^B which are the impedances of the switching element in state A and B, and S_{32} and S_{21} are the coupling factors between the elements retina-collector and illuminator-retina respectively.

From the point of view of the retina design, a quality parameter defining the matching between the probe antenna and switching element can be extracted from expression 2.7. Taking the absolute value of $\Delta\tau_{co,il}$:

$$|\Delta\tau|^2 = |S_{32}S_{21}|^2 \left|\frac{(Z_T + Z_0)^2}{2Z_0}\right|^2 \frac{ME}{4R_T^2} \tag{2.8}$$

being $R_T = \Re e\{Z_T\}$

The difference in the reflection coefficient due to the two states (A-B) of the switching element impedances is known as the Modulation Efficiency (ME) [39–41]. The ME represents the differential signal level received at the collector and it is defined as:

$$ME = \frac{4R_T^2 \left|Z_L^A - Z_L^B\right|^2}{\left|Z_T + Z_L^A\right|^2 \left|Z_T + Z_L^B\right|^2} \tag{2.9}$$

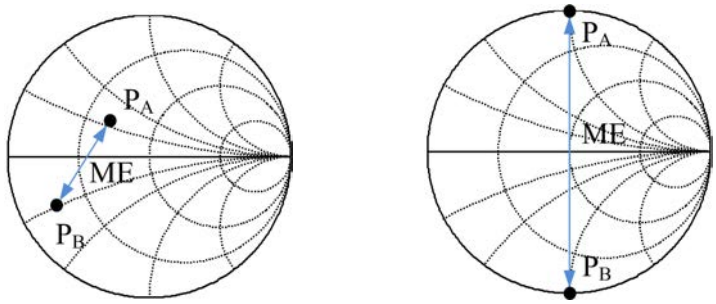

Figure 2.4: Smith chart plots of the two impedance states represented by point P_A and P_B respectively. (a) Random impedance states (b) Maximum ME.

The probe reflection factor $\tilde{\rho}_L$ is the reflection coefficient of the probe, and takes into consideration the antenna and the switching element impedances:

$$\tilde{\rho}_L^i = \frac{Z_L^i - Z_T^*}{Z_L^i + Z_T} \tag{2.10}$$

where i can be each of the two possible states of the switching element that will be referred as A or B states,

$$ME = |\Delta\tilde{\rho}_L(Z_{L_A}, Z_{L_B})|^2 = \left|\tilde{\rho}_L^A - \tilde{\rho}_L^B\right|^2 \tag{2.11}$$

The ME values are bounded to $0 \leq ME \leq 4$ or $ME_{dB} \leq 6\,\text{dB}$. ME is maximized when $\tilde{\rho}_L^A$ and $\tilde{\rho}_L^B$ are in phase opposition. Therefore, in a design process the goal is to approach the 6 dB ME value for a combination of probe and loads. A representation of $\Delta\tilde{\rho}_L$ on a Smith chart is useful to evaluate the difference in the ME modifying the load impedance Z_{re}. The two impedance states $\tilde{\rho}_L^A$ and $\tilde{\rho}_L^B$ can be located in the Smith chart normalized to the probe antenna impedance (see Figure 2.4). In this case $\Delta\tilde{\rho}_L$ will be the square distance between point P_A and P_B.

All in all, the design of the retina and the rest of the elements in the system should maximize the parameter $\Delta\tau_{co,il}$ which is the representative index of the MST system. This parameter can be dissected among three other quality parameters previously described:

Modulation Efficiency The aim of the ME is to allow to measure how well the probe antenna of the retina couples to the switching element. At millimeter wave frequencies the impedance states given by the available devices can be far from this condition and they cannot be freely chosen by the designer. In this case the optimization process is based in designing an antenna with a given Z_T that maximizes the ME for the given switching element.

Surface Wave Efficiency At submillimeter-wave frequencies, the major problem of planar antenna arrays is associated with the dielectric substrate losses. This efficiency constitutes a power loss that falls within the overall $\Delta\tau_{co,il}$ and corresponding S_{32} and S_{21} parameters. As it will be discussed in the following section, the antenna of

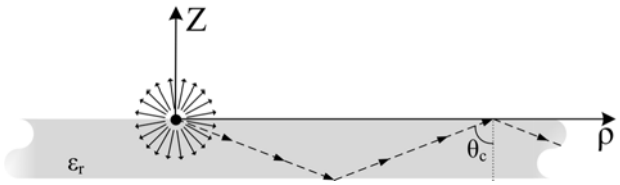

Figure 2.5: Representation of a surface wave travelling inside a dielectric surface.

the retina has to be carefully chosen in order to minimize the effect of the substrate thickness in the overall system efficiency.

Coupling Efficiency This parameter describes the losses due the coupling between the illuminator-retina-collector. It depends on the matching of the illuminator, retina and collector impedances Z_T and Z_0 and the S_{32} and S_{21} parameters.

In many cases, because of the large size of the retina (if there is a high number of elements), the collector and illuminator cannot be able to be simulated within the system. In this case the design of the retina can be adapted to the maximization of the surface wave efficiency, modulation efficiency, and depending only in the impedance of the probe antenna and switching element.

2.3 Surface-Waves Analysis

At millimeter and submillimeter wave frequencies, planar antennas suffer from high losses due to the propagation of surface waves inside the dielectric. When a source is placed in a dielectric surface the rays propagate through the surface reaching the dielectric-air edge. At that point, the rays that interface the edge with an angle above the critical angle $\sin\theta_c = 1/\sqrt{\epsilon_r}$ are completely reflected back into the substrate generating successive zigzag reflections along the transversal axis of the dielectric (see Figure 2.5). The propagation constant of these propagating surface waves is larger compared to the free space. Therefore, they are trapped waves that do not radiate in the free space and will take a certain percentage of the power and consequently an efficiency loss.

There are a few approaches used to mitigate the effect of the surface waves losses. The first one is to reduce the thickness of the substrate until it is electrically thin (around one hundredth of the dielectric wavelength thick). In this case the antenna will couple weakly into the dielectric as it happens at microwave frequencies. Table 2.1 illustrates the small dimensions that electrically thin substrates have at millimeter and submillimeter wave frequencies. The fabrication of planar antennas on such thin substrates or also called membranes is quite difficult, although there are some results published in [42], where for instance, a membrane of 1 μm of silicon-oxynitride was fabricated for an antenna working at 700 GHz.

The second approach is to use an infinite thick substrate ending with a lens that couples the radiation within the substrate into free space [43]. In this case, the antenna sees two infinite medium, one top and one on the bottom, and in order to focus all the radiation into a directive beam, the top of the dielectric is curved. The front to back ratio

	100 GHz	300 GHz	500 GHz	1 THz
$\epsilon_r = 4$	15 μm	5 μm	3 μm	1.5 μm
$\epsilon_r = 12$	8.6 μm	2.8 μm	1.7 μm	0.8 μm

Table 2.1: Examples of electrically thin substrates (thickness $< \lambda_g/100$) at different millimeter and submillimeter wave frequencies.

of planar antennas between air and a dielectric can be approximated as $\epsilon_r^{3/2}$. Therefore, in order to focus all the antenna radiation into de dielectric, high substrate permittivities are required. This approach will be studied in detail in part II of this thesis.

Other approaches include the use of Electromagnetic Band Gap (EBG) substrates. This substrates consist on all sort of periodic arrangements that control the properties of the propagation of electromagnetic waves inside the dielectric. Some preliminary results at 500 GHz are shown in [44]. Another solution is the use of metallic bias in the substrate to prevent the propagation of the surface waves as it has been implemented in the microwave regime [45]. However, this solution is not feasible to implement it at submillimeter wave bands because they cannot be implemented with the fabrication methods currently available. The last approach comprises a solution which uses an antenna geometry that do not excite surface waves modes inside, like the double arc slot from [46, 47]. This approach has been studied in this section as it can be implemented and fabricated at high frequencies.

In this part of the thesis, the use of planar, electrically thick substrates for planar antennas is studied [48]. The emphasis of the following discussion is on the use of simple antenna geometries and dielectric substrates, which make the fabrication of an efficient millimeter and submillimeter wave planar antenna structure as simple as possible.

In order to evaluate the efficiency of an antenna printed on a thick dielectric, first, we are going to define the surface wave efficiency of an antenna as the ratio:

$$\eta_{SW} = 1 - \frac{P_{SW}}{P_{rad} + P_{SW}} = \frac{P_{rad}}{P_{rad} + P_{SW}} \tag{2.12}$$

being P_{SW} the power radiated by the antenna inside the dielectric and P_{rad} as power radiated by the antenna into free space. Considering only the dielectric losses, the input power can be defined as:

$$P_{in} = P_{rad} + P_{SW} + |S_{11}|^2 P_{in} \tag{2.13}$$

being S_{11} the reflection coefficient of the antenna. Therefore, the surface wave efficiency can be defined as:

$$\eta_{SW} = 1 - \frac{P_{SW}}{P_{in}(1 - |S_{11}|^2)} \tag{2.14}$$

The power delivered within the substrate previously named as P_{SW} can be calculated by integrating the Poynting vector in a cylindric surface around the antenna:

$$P_{SW} = \frac{1}{2} \int_{S_{SW}} Re\left\{\mathbf{E_{SW}}(\rho, \phi, z) \times \mathbf{H_{SW}}(\rho, \phi, z)^*\right\} \mathbf{dS} \tag{2.15}$$

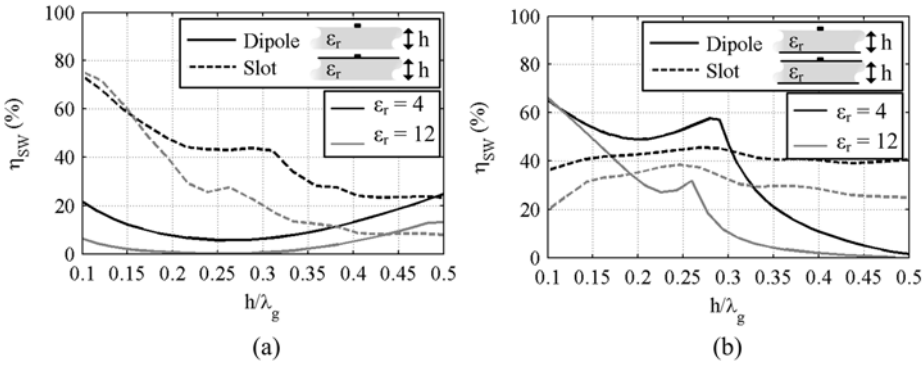

Figure 2.6: Surface wave efficiency of a dipole (solid line) and slot (dashed line) as a function of the substrate thickness for $\epsilon_r = 4$ (black line) and $\epsilon_r = 12$ (grey line) for non grounded (a) and grounded (b) substrates.

being E_{SW} and H_{SW} the electric field and magnetic field of the surface wave. Considering the elementary surface element $\mathbf{dS} = \hat{\rho}\rho dz d\phi$:

$$P_{SW} = \frac{1}{2}\int_{S_{SW}} Re\left\{\mathbf{E_{SW}}(\rho,\phi,z) \times \mathbf{H_{SW}}(\rho,\phi,z)^*\right\}\hat{\rho}\rho dz d\phi \tag{2.16}$$

The efficiency of a single slot and a single dipole antennas on grounded substrates as a function of substrate thickness is shown in Figure 2.6. Both graph has been obtained by simulating in CST a small dipole/slot and integrating the Poynting vector within a cylindric surface as it has been referred in Equation 2.16. This approach will allow the evaluation of the further antenna designs for different non elemental geometries. The degradation of the radiation pattern as a function of the substrate thickness can be observed in Figure 2.7. Both E and H plane suffer from high rippling when the surface wave efficiency increases. This effect happens as a result of the trapped surface wave, i.e the surface-wave eventually arrives to the border of the substrate and it is radiated in an non-controlled way, which it strongly affects the radiation pattern of the antenna. Note that the substrate thickness has been normalized by the dielectrics wavelength $\lambda_g = \lambda_0/\sqrt{\epsilon_r}$.

This behavior can be understood by studying the propagation of the different surface wave modes excited inside the dielectric. The propagation constant of the different modes has been characterized by looking into the spectral properties of the Green's function as in [48, 49]. The analysis used here calculates the radiated fields from an infinitesimal element. The propagation constant of a magnetic source placed on a grounded dielectric of and thickness h is shown in Figure 2.8. It can be observed that all the modes start to propagate with a dielectric constant equal to k_0 and at a certain substrate thickness they start to grow until a a maximum which is equal to the propagation constant of the medium $k_0\sqrt{\epsilon_r}$. The first TM_0 mode has a zero cut off frequency due to the fact that it is independent of the multiple bounds of the wave within de dielectric. Note that the TE_0 mode is not propagated due to the presence of the ground plane. These plots would correspond to propagation constant of an infinitesimal slot or also, to a grounded dipole.

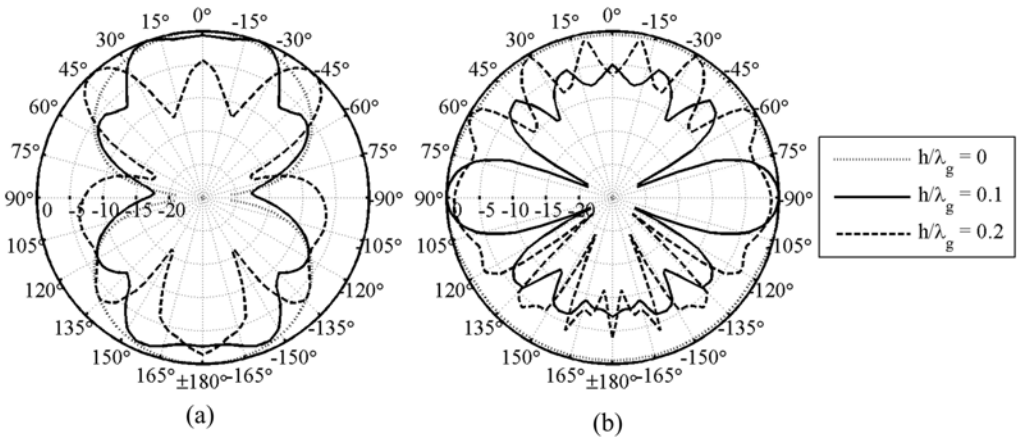

Figure 2.7: Radiation patterns of a dipole over a substrate of $\epsilon_r = 4$ for different thickness: (Left) E-Plane (Right) H-Plane.

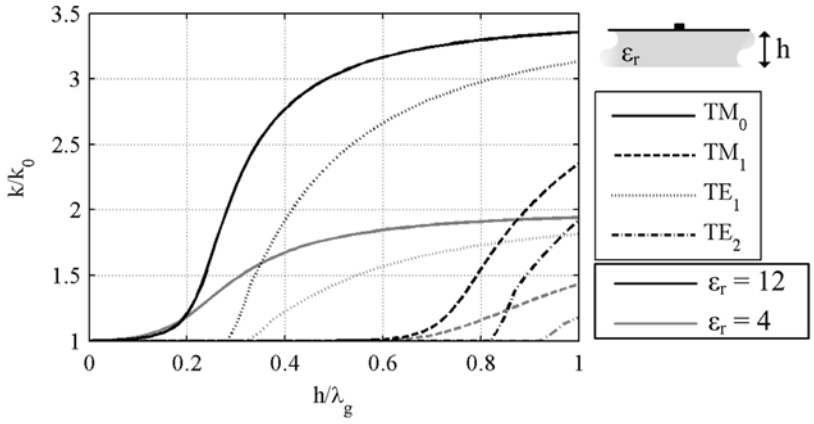

Figure 2.8: Propagation constants of the different TE and TM modes propagated inside a grounded dielectric substrate excited by a magnetic source.

In the case of an infinitesimal dipole on a substrate, the functions are similar to the slots, except that the TE_0 does propagate with a 0 cut off frequency as well as the TM_0 mode. After that, the same TE and TM modes are also present but interchanged.

On the other hand, the modes of a double grounded substrate are shown in Figure 2.9. In this case, the first mode TM_0 propagates with a constant propagation of $k = k_0/\sqrt{\epsilon_r}$ and the following modes propagate with $k = 0$ because it is a closed structure and there is no radiation to free space. Moreover, the TM_0 mode propagating with a zero cutoff frequency the propagating is constant and the TE_1 propagates at a substrate thickness of 0.5 λ_g. Therefore, by selecting a proper antenna geometry which reduces the excitation of this TM_0 mode, a good efficiency could be achieved until a dielectric thickness of $\lambda_g/2$ instead of the $\lambda_g/4$ that can be achieved in the previous case. Note that a dipole cannot obtain this behavior as it cannot achieve this parallel plate effect.

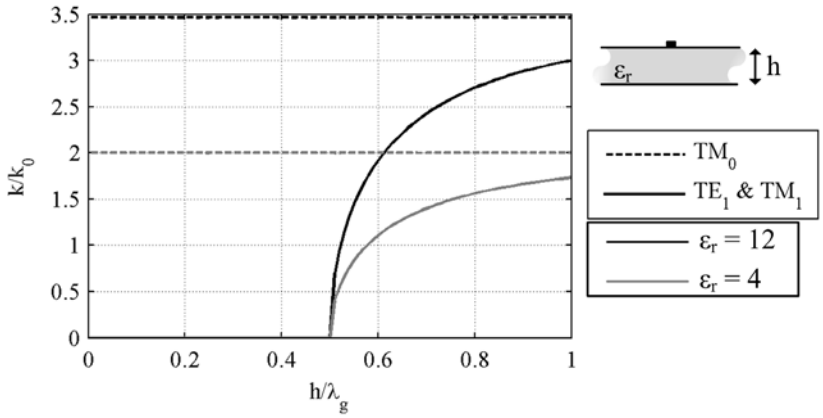

Figure 2.9: Propagation constants of the different TE and TM modes propagated inside a double grounded dielectric substrate excited by a magnetic source.

Note that Figures 2.8 and 2.9 show the results of two dielectrics with different permittivities $\epsilon_r = 12$ (approximation to the permittivity of silicon, commonly employed at these frequencies) and $\epsilon_r = 4$ (which is close to quartz) have been calculated in order to illustrate how the behavior for different substrate materials is consistent: they are both scaled to its permittivity. Therefore, as it is shown in Figure 2.6, it is convenient to work with a low permittivity dielectric in order to couple less radiation into the substrate.

A technique consisting on using twin elements antennas has been studied in [50, 51] that increases the efficiency for antennas placed on electrically thick double grounded substrates. This approach consists on reducing the amount of power delivered to the TM_0 mode by placing two slot elements broadside to each other properly spaced and driven in phase. The optimal inter element distance is close to half a wavelength $\lambda_g/2$ where it produces the phase cancellation along the broadside axis of the slots (see Figure 2.10a). Therefore, if the TM_0 is reduced, the antenna can now have a good performance for substrate thicknesses until $\lambda_g/2$ (where the next modes TE_1 and TM_1 start to propagate) as it is shown in Figure 2.10b. Note that higher efficiency can be obtained for longer double slots l_ds, where the optimal lengths is λ_m, being $\lambda_m = \lambda_0/\sqrt{(\epsilon_r + 1)/2}$. In case of our system, because the inter element spacing is $\lambda_0/2$, the arm length is limited by this dimension. In the case of a dipole element, however, this placement of two elements do not have the same effect because the direction that the dipoles radiate the TM_0 mode power is off the ends of the element and not in the endfire direction.

The purpose of this array is to couple the radiation to both sides (from the illuminator to the collector, going through this radiating element of the retina) of the array. Therefore, even if one could use a dipole with thinner substrates, one could not achieve an even front to back ratio. Taking as a reference the double slot of Figure 2.10, by placing a double slot in the ground plane of this antenna, the radiation can go through and an even front-to-back ratio can be obtained (see the radiation pattern in Figure 2.11). Moreover, the surface waves efficiency can as well be improved in for a wide range of dielectric thickness (see Figure 2.12). Considering the the quasi-cylindrical nature of the surface waves, by curving the arms of the double slot into a curved shape, a considerable improvement in

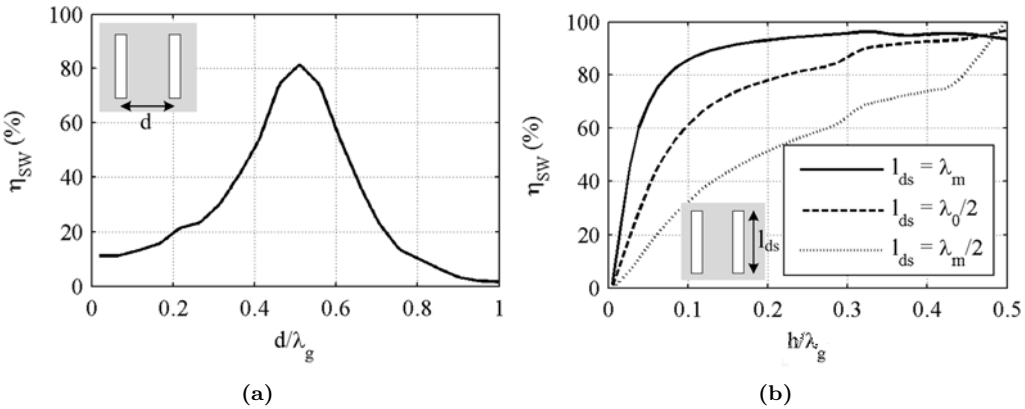

Figure 2.10: Surface wave efficiency of double-slot with ground plane as a function of: (a) the arm slot separation d and substrate thickness of $h = 0.25\lambda_g$ (b) the substrate thickness for $\epsilon_r = 4$.

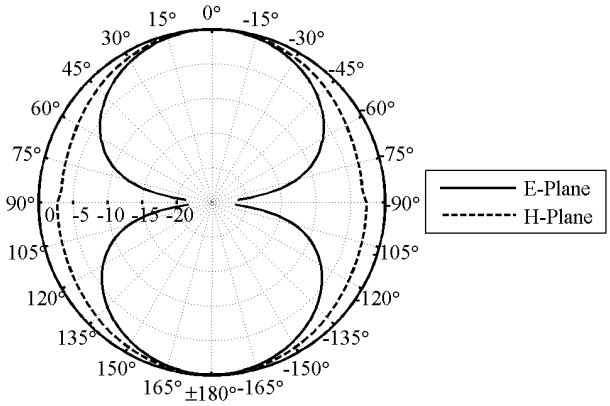

Figure 2.11: Radiation pattern of the double-slot placed on a substrate of thickness $\lambda_g/4$ grounded with another double-slot.

the efficiency is obtained as shown in Figure 2.12. Moreover, a good frequency behavior can be obtained over a bandwidth of 25% as is shown in Figure 2.10b.

All in all, there has been demonstrated in this section how surface waves losses are a significant problem for planar antennas at THz, although the efficiency of these antennas can be significantly improved by choosing the correct antenna geometry. Dipoles and slots are not a suitable to work for substrates above $0.1\lambda_g$. On the other hand, grounded double-slots can be optimized to work in substrates of thicknesses up to $0.5\lambda_g$. These considerations will be taken into account for the further design of the antenna array prototypes in our system.

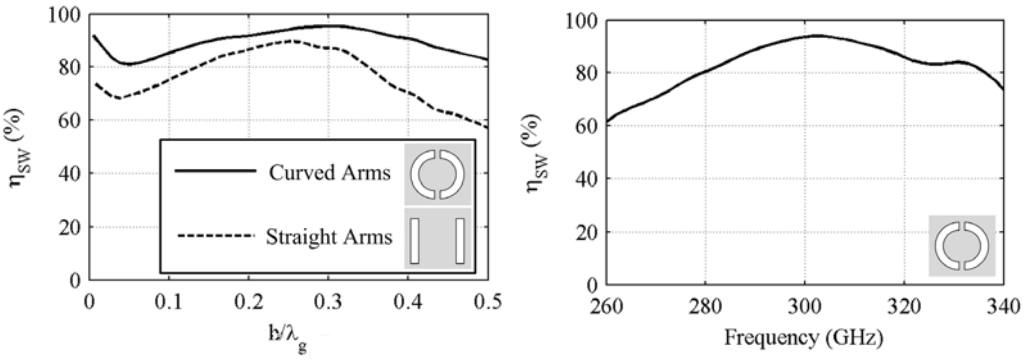

Figure 2.12: Surface wave efficiency of a: (a) Curved/Straight arm double-slot as a function of the substrate thickness of $\epsilon_r = 4$ grounded with a double-slot. (b) Curved arm double-slot placed on a substrate of thickness $\lambda/4$ and $\epsilon_r = 4$ grounded with a double-slot as a function of the frequency.

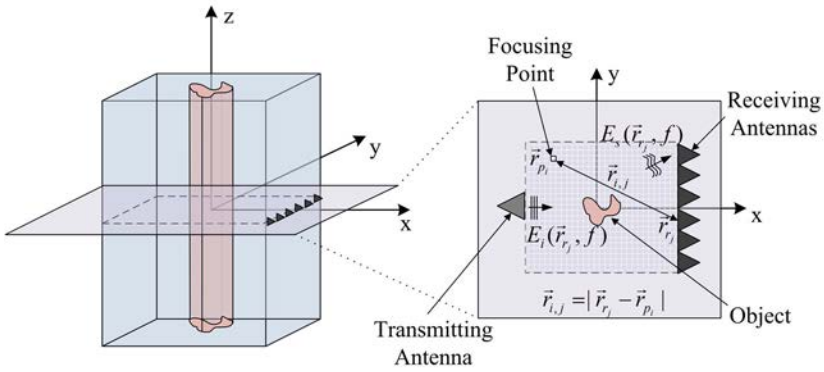

Figure 2.13: 2-D planar tomography sensing geometry for the reconstruction of an object.

2.4 Tomography Imaging Techniques

In a tomographic imaging system, the key is to sample a sufficient number of scattered field values in space to recover the currents induced inside the object by the incident or illuminating field. This problem is known as the inverse scattering problem. The object that we want to image needs to be illuminated by a plane wave generated by a transmitter; and then the scattered field by the object requires to be measured in an array of points (i.e. output ports). This multiport measurement can be achieved by either virtually generating it with the movement of one antenna, or by using a real array of multiplexed antennas. Even though with the first approach the coupling between antennas is not present and the receiving system is more simple, the second one is certainly advantageous for a real time system requirement. The imaging system proposed in this research corresponds to a planar imaging scenario with a real array of antennas in order to perform high speed imaging.

The reconstruction algorithm employed for the reconstruction is based on a technique called mono-focusing [52, 53], which is used for systems of multiple receivers and a plane wave illuminator as a transmitter. This algorithm is based on the reconstruction of the local electrical properties of the object by means of synthesis of a receiver focusing operator. This focusing operator provides a compensation of the amplitude and the phase variations suffered by a wave due to the presence of the object. In Figure 2.13, the reconstruction scheme of the mono-focusing algorithm is shown.

A given amount of antennas N_r acting as receivers are placed along a line. When a transmitter transmits an incident field $E_i(\vec{r}_{r_j}, f)$ towards the object, this wave impinges on the object generating a diffracting field or scattered field $E_s(\vec{r}_{r_j}, f)$ that is captured by the receiver $E_r(\vec{r}_{r_j}, f)$. The vector $\vec{r}$ represents the position vectors within the object. The total electric field received $E_r(\vec{r}_{r_j}, f)$ measured at the receiver position $\vec{r}_j$ is related to the scattered field $E_s(\vec{r}_{r_j}, f)$ and to the incident field in absence of the object $E_i(\vec{r}_{r_j}, f)$ through the following equation:

$$E_r(\vec{r}_{r_j}, f) = E_s(\vec{r}_{r_j}, f) + E_i(\vec{r}_{r_j}, f) \tag{2.17}$$

The reconstruction algorithm forms every image point of the local electrical properties of the object by the synthesis of one focus group (mono-focusing) of antennas (receivers) [52]. The received scattered fields are weighted by a focusing operator in order to be focused on a unique point. Thus, under Born approximation, which supposes low scattering objects, the following equation reconstructs the image form the scattered field:

$$\Psi(\vec{r}_{p_i}, f) = \sum_{j=0}^{N_r} E_s(\vec{r}_{r_j}, f) e^{jk\vec{r}_{i,j}} \tag{2.18}$$

where $\vec{r}_{i,j}$ is the distance between the receiving antenna j and the pixel i. Therefore, only when the focused point corresponds to the object position the focusing operator will perfectly compensate the real path of the signal and the maximum value of the reconstruction will be obtained. Applying this mono-focusing operator to every pixel of the image, a replica of the extended object is obtained.

In order to predict the performance of the system employed, a canonical scenario has been simulated of the image reconstruction algorithm. It consists in the calculation of the theoretical scattered field distribution that a metallic cylinder scatters [54] over an array of N_r receiving antennas in an air medium (see Apendix A). Once obtained this field, the image can be reconstructed with procedure previously explained. This scenario has been chosen as it is easily replicable in reality, and therefore the evaluation of the imaging capabilities of the array can be evaluated.

Figure 2.14 shows the analytically reconstructed images of a Perfect Electric Conductor (PEC) cylinder placed in front of a retina of $N_r = 16$ elements in different positions and for different radius. The retina is placed in $x = 0$ (right axis) and centered vertically at $y = 0$. The cylinder surface is marked with a black circle. In Figures 2.14a,b and c the cylinder is displaced 2λ vertically and sweeps horizontally at 6λ, 4λ and 2λ. In Figure 2.14d,c and f the cylinder is placed in the middle of the retina vertically and sweeps horizontally at 6λ, 4λ and 2λ. Note that because the retina has 16 elements and the spacing between elements is $\lambda/2$, the reconstructed image has an available reconstructing

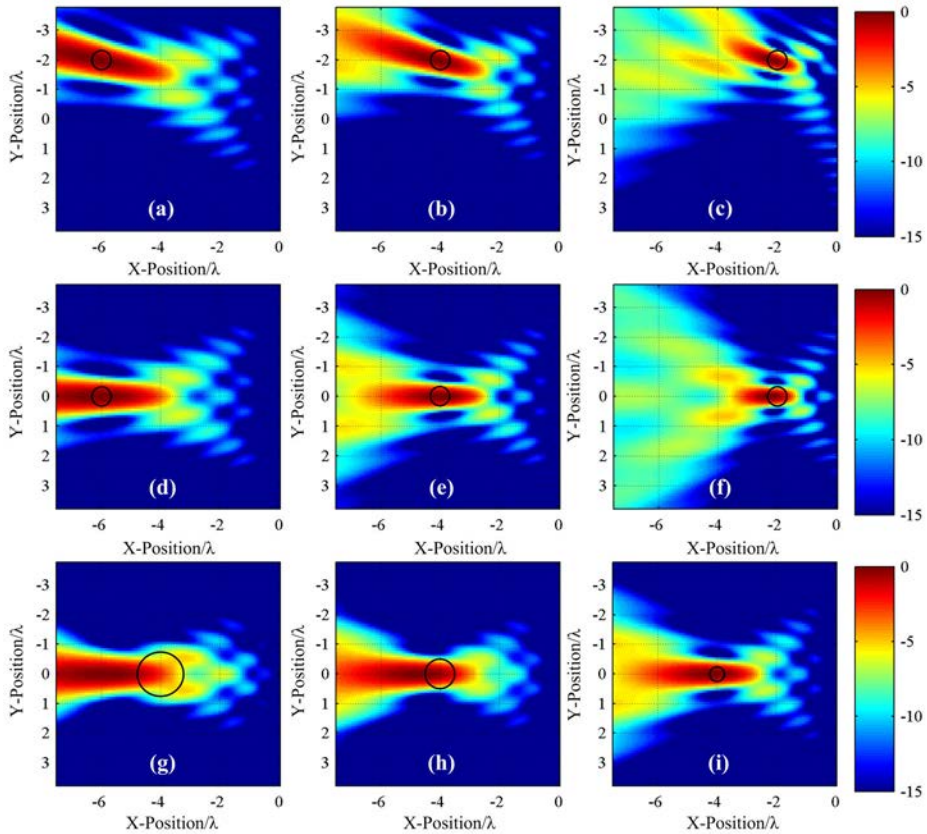

Figure 2.14: 2-D planar tomography reconstruction images of a PEC cylinder with a retina of $N_r = 16$ for different scenarios: (a), (b). (c) Cylinder of diameter $\lambda/3$ placed at $y = 2\lambda$ and $x = 6\lambda$, $x = 4\lambda$ and $x = 2\lambda$ respectively. (d), (e). (f) Cylinder of diameter $\lambda/3$ placed at $y = 0$ and $x = 6\lambda$, $x = 4\lambda$ and $x = 2\lambda$ respectively. (g), (h), (i) Cylinder of diameter $3\lambda/4$, $\lambda/2$ and $\lambda/4$ respectively in the center position ($x = 0$ and $y = 0$) of the imaging scenario.

area of dimensions $(N_r - 1)\lambda/2 \times (N_r - 1)\lambda/2$ which in this case is $7.5\lambda \times 7.5\lambda$. It can be observed that the cylinder can be distinguished in the image, however it contains multiple and high-contrast scattering factors. Figures 2.14g, h and i show the image of a cylinder for different radius $3\lambda/4$, $\lambda/2$ and $\lambda/4$ respectively. A displacement of the cylinder in the horizontal direction can be observed due to the multiple scattering effect that appear when the visualization angle is reduced.

In order to smooth the non linear and frequency dependent phenomena present in the previous images, the combination of different images at different frequencies and from different points of view can provide accurate spatial and electrical information of the electrically extended object. By using multi-frequency and multi-view, these non linear and frequency dependent phenomena will be smoothed and reduced as it is presented in the following section.

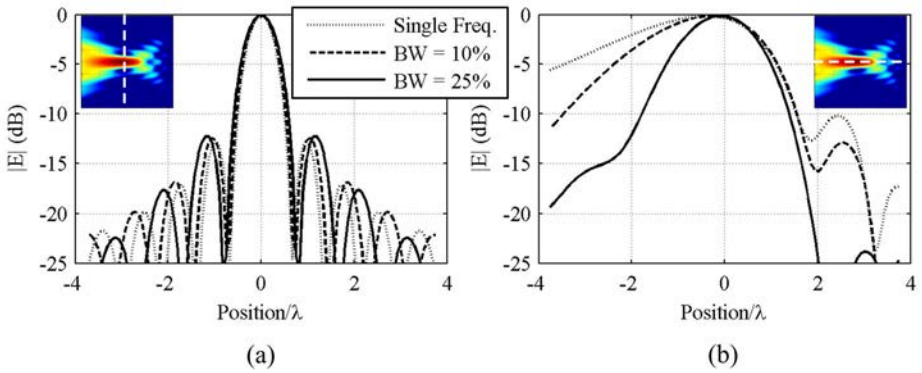

Figure 2.15: (a) Transversal (b) Longitudinal cross-section of the 2-D reconstructed image of a PEC cylinder for using a frequency sampling with a bandwidth of 25%, 10%, and a single frequency sampling.

2.4.1 Frequency sampling criteria

In order to improve the quality of the image, multiple frequencies can be combined, allowing the acquisition of a high number of spatial frequency components of the spectrum. A coherent combination of the different images at each frequency is used to enhance the features of interest of the individual images without having the destructive interference between images [53]. The frequency domain sampling is chosen to avoid aliasing according to:

$$\Delta f \leq \frac{c_{re}}{4R_s} \tag{2.19}$$

where c_{re} is the propagation velocity in the background medium, in this case $c_{re} = c_0$ as the medium is air; R_s corresponds to the imaginary radius of a circle that circumscribes the obtect with the transmitter and receiver. This sampling criteria is hold for impenetrable and penetrable objects.

In Figure 2.15a and b, the transversal and longitudinal sections (the insets of the figure show the image vertical and horizontal cuts respectively) of the reconstructed image for a frequency bandwidth of 10% and 25% are shown. The image for a single frequency is also included as a reference. A PEC cylinder of radius $\lambda/3$ is centered in front of a $N_r = 16$ element retina. While the transversal section (Figure 2.15a) remains still in both cases, the longitudinal section (Figure 2.15b) improves significantly when multiple-view is applied.

2.4.2 Space sampling criteria

In Multi-View, the system rotates around the scenario in order to obtain multiple views of the sample. It makes a complete 360-degree rotation around the subject obtaining a complete set of data from which images may be reconstructed covering all the views. The minimum number of views that are required to avoid loss information [55] and guarantees

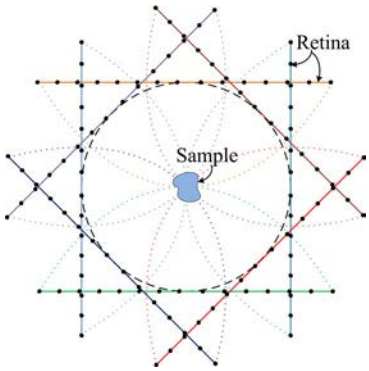

Figure 2.16: Space sampling basic scheme for $N_\phi = 6$.

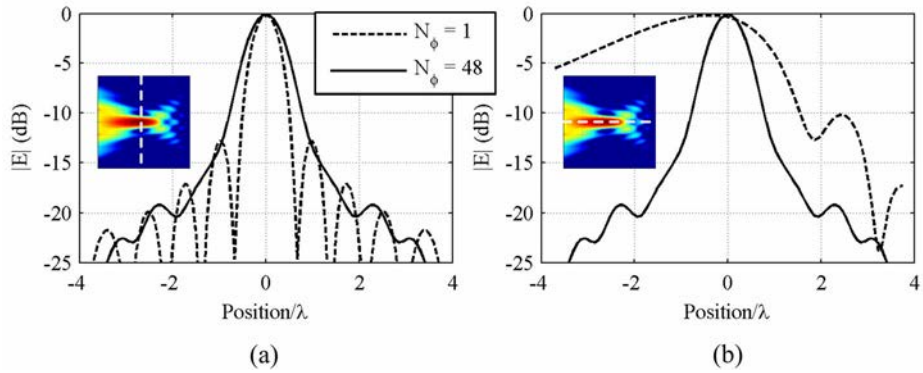

Figure 2.17: (a) Transversal (b) Longitudinal cross-section of the 2-D reconstructed image of a PEC cylinder for using a space sampling of $N_\phi = 1$ and $N_\phi = 48$.

an image resolution of $\lambda/2$ are:

$$N_\phi \geq \frac{4\pi R_s}{\lambda_{re}} \tag{2.20}$$

where λ_{re} is the wavelength in the external medium at the highest operating frequency. Therefore, the maximum angular step can be written as:

$$\Delta\phi \leq \frac{\lambda_{re}}{2R_s} \tag{2.21}$$

In the example previously used where a retina of $N_r = 16$ (then $Rs = 7.5\lambda/2$) is considered, the minimum number of steps is $N_\phi \geq 48$. In Figure 2.17a and b, the transversal and longitudinal sections of the reconstructed image for 1 view and 48 views of the object are shown. While the transversal section (Figure 2.17a) is maintained the same in both cases, the longitudinal section (Figure 2.17b) improves significantly when multiple-view is applied. This method can be interpreted as a way to create a uniform equivalent illuminating field inside the object.

3

Chapter 3
Retina Prototypes - Fabrication and Measurements

Technology at millimeter and submillimeter band is limited by the power budget restrictions and high losses that sources and receivers suffer at such high frequencies. Therefore, a high level of integration is required among all the system components to avoid unnecessary additional losses. From the antenna point of view, the geometry of an antenna or an array of antennas compatible with Monolithic Microwave Integrated Circuits (MIC) technology is a technological goal of the current era. This is due to the many significant challenges that still remain in the design and fabrication of such antennas due to the difficulty to achieve high efficiencies and broad bandwidths.

The system employed to evaluate the performance of these planar arrays has been analyzed in the previous chapter and the requirements from the design point of view are translated into the maximization of the ME, the minimization of the surface wave efficiency or maximization of the radiation efficiency, the minimization of the coupling effi-

ciency and the mutual coupling among all the antennas of the retina, and the definition of certain scanning parameters (number of probes, spacing, frequency span, multi-view, etc). In this chapter we will see that there is a high compromise between the performance of these elements, and a tradeoff will be achieved to obtain the highest performance with the technology and fabrication processes currently available at millimeter and submillimeter wave frequencies.

This chapter presents a series of prototypes built as an experimental validation of the system characterization and the analysis obtained in the previous chapter. One of the prototypes is an MST imaging system which could be employed at millimeter and submillimeter wave frequencies. This prototype has been designed and fabricated at 100 GHz due to the availability of the technology at that moment. However, this prototype was designed facing all the challenges that occur at higher frequencies like the surface wave propagation losses. Therefore, even if a thinner substrate could be obtained commercially, the design was performed with a thicker one in order for the design to be scalable at THz frequencies. Another prototype at submillimeter wave frequency 300 GHz was designed with the technology available in that regime. And last, the potential of RF-MEMS technology was analyzed as a potential candidate for millimeter and submillimeter-wave frequencies. Besides the different nature of the prototypes providing a specific individual analysis and design, each one is characterized by the use of different technologies and fabrication processes adding additional and individual requirements to the design process.

3.1 MST Imaging System Prototype at 100 GHz

The system implemented in this section corresponds to a tomographic system with planar geometry where, in this case, the object is illuminated by a plane wave and the scattered field is measured along a probing line. In Figure 3.1 the basic scheme of the near field system proposed is shown. An illuminator or transmitter based on a horn antenna emits millimeter wave radiation that produces a local plane wave that illuminates the sample. The scattered field produced by the object is sampled at the retina. The retina is able to mark the value of the electric field at the position of each element using MST. Specifically, the field is marked by using a low frequency (LF) modulation of the probe. By using a different LF modulation frequency for each probe it is possible to multiplex the measurements of all the probes and reduce the measurement time. Once the electric field has been marked at the retina, it is gathered by the collector that is followed by the receiving system. After this, the image can be calculated by postprocessing the measured scattered fields.

The retina prototype designed is based on a printed circuit with a 1-D array of 16 probe antennas over a dielectric substrate fixed against the collector aperture. Because the operating frequency of the prototype is 100 GHz, the maximum spacing between probes is 1.5 mm ($\lambda/2$) that properly sample the scattered field distribution according to the Nyquist theorem. Each probe is composed of an antenna that receives and reradiates the scattered field, a switching element that modulates the signal and a filter that reduces the coupling between the probe and the modulation circuit. The antenna geometry is selected in order to minimize the mutual coupling between probes and to avoid its interference with the filter.

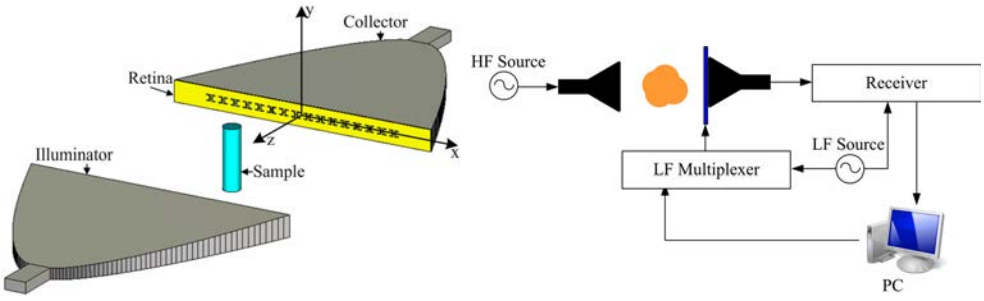

(a) (b)

Figure 3.1: (a) Imaging scheme of the system. (b) Global diagram of the imaging system.

As it has been described on the previous chapter, at millimeter wave frequencies and submillimeter wave frequencies, the major problem regarding the antenna efficiency is associated with the surface waves propagating within the dielectric substrate. As demonstrated, by choosing a double-slot antenna geometry over a grounded dielectric this efficiency can be significantly improved to work for substrates below $\lambda_g/2$. Therefore, for the design of this prototype, a double-slot geometry was employed to perform the optimization over an electrically thick substrate of thickness around $\lambda_g/4$. Moreover, if this array of double slots is placed in the H-plane the mutual coupling between the antennas is minimized. This could not be achieved with a linear array of dipole antennas in the H-plane, as it would be difficult to place the filter in between the dipoles located at $\lambda/2$ between each other. Therefore, a system composed a double-slot antenna and a collector opening aperture in the H-plane has been chosen for this prototype.

A switching element is placed in each probe antenna port that is modulated at a certain low frequency. This switching element provides two different load impedances to the probe antenna. The characterization of this switch is an important step to ensure the performance of the antenna. The switch that has been employed for this prototype is a PIN diode. PIN diodes are the main semiconductor switching components that are used in microwaves because of their reliability, low cost and compatibility with standard Printed Circuit Board (PCB) assembly processes. This diodes are commercially available at higher frequencies however beam-lead packaging rises significantly the device and assembly cost. In the following section a full detail of the characterization of this switch is performed.

3.1.1 Switching Element Characterization - PIN Diode

For this prototype at 100 GHz a commercial PIN diode has been chosen due to its small dimensions and its cost. It corresponds to the model MA4AGBLP912 from MACOM Technologies [56] (see Figure 3.2a). The switch characterization has been performed using calibrated data provided by the manufacture regarding the dimensions and behavior.

The objective of the characterization of the PIN diode is to obtain the impedance of the core of its P-N junction. The core of a PIN diode is the P-N junction with its I-V and C-V characteristics and can be characterized using the equivalent circuit model. The most common way of modeling this junction is a parallel combination of a resistor

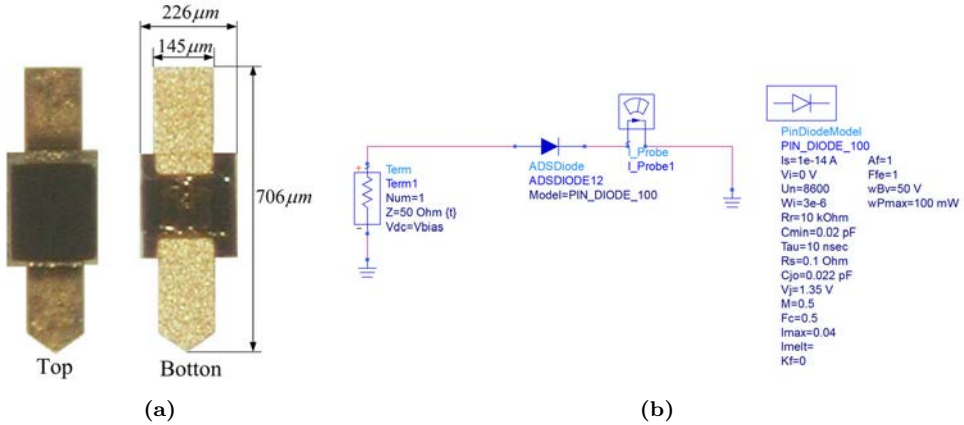

(a) **(b)**

Figure 3.2: (a)Photograph and (b) Equivalent circuit model PIN diode provided by [56].

and a nonlinear capacitor. In our case, the manufacturer procured the specific Spice model for this PIN diode based on target specifications, simulated results and prototype measurements, which would be more accurate than the simple circuit model. These parameters were then simulated using ADS [57] as shows the diagram of Figure 3.2b and the impedance was extracted for the frequency band of interest. The impedance has been obtained by the simulation of the diode in ON and OFF state corresponding to a bias voltage of $V_{ON} = 1.35\ V$ and $V_{OFF} = 0\ V$ respectively. Figure 3.3a corresponds to the impedance as a function of the frequency of the PIN diode junction in OFF state while the impedance in ON state is a constant value of $Z_{L_{ON}} = 0.13\ \Omega$.

This model corresponds to the equivalent circuit junction modelling of the diode. However, this circuit does not contain the parasitic elements of the physical properties of the diode, i.e the cross-coupling effects between different parts of the circuit, which might be significant, especially in densely packed MIC applications. Therefore, in order take into account a physical model of the diode is included in the full wave simulations of the antenna. In this case, the physical model was obtained by adapting a common diode model to the dimensions provided by the manufacturer. A 3-D electromagnetic full-wave simulator such as MW-CST the geometry of a common PIN diode was defined associating the various materials with the desired parts of the circuit including dielectric constant and loss tangent making the most realistic model in order to obtain the parasitic effects of this diode. This model will be only used for the simulation of the parasitic effect and not the other nonlinear physical parts. The combination of the two consists in obtaining the S-Parameters of the simulated full-wave device and load them with the impedances obtained for the equivalent circuit model.

Once the junction impedance is determined, the performance of the antenna in our system can be evaluated by the calculation of the ME. This parameter, as it has been explain before, shows how well the antenna is matched with the diode. In Figure 3.3b, the ME as a function of the impedance of the antenna Z_T at 100 GHz is shown. It can be observed that the best matching that the antenna can obtain at 100 GHz is of 5.95 dB (the maximum being 6 dB) which is significantly high, and corresponds to a desired antenna impedance of $Z_T = 30 + 14j\ \Omega$.

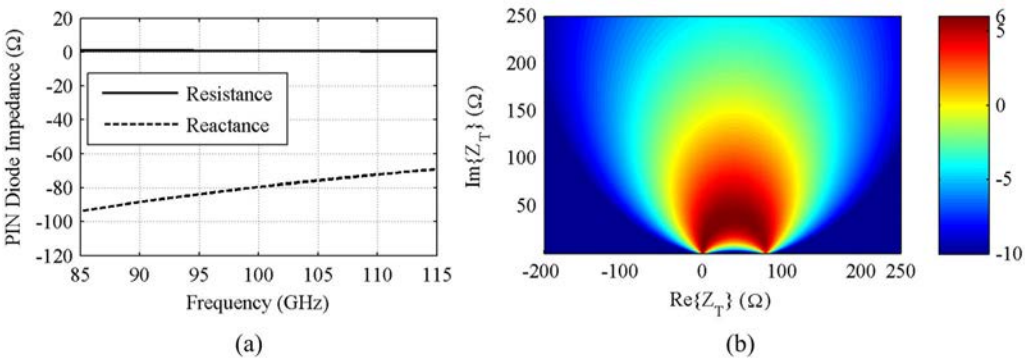

Figure 3.3: Junction impedance of the PIN diode in OFF state. Note that the impedance in ON state is a constant of $Z_{L_{OFF}} = 0.12\Omega$. (b) ME as a function of the impedance of the antenna Z_T.

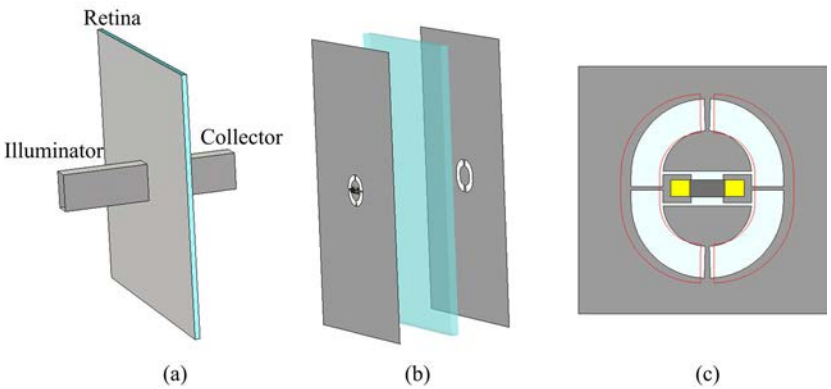

Figure 3.4: Simulation of the system to perform the optimization of the antenna probe.

3.1.2 Retina Design

The retina design is begun by the maximization of the differential transmission coefficient $\Delta\tau_{co,il}$ between the illuminator and the collector when the retina is loaded with both impedances of the PIN diode obtained in the previous section. The basic simulation scenario is shown in Figure 3.4. First, the optimization will be performed for one element and two waveguides will be used as an illuminator and collector (see Figure 3.4a). Note that because the main goal is to design an array of antennas, the substrate used for the simulation of this element has been considered infinite. Figure 3.4b shows the basic scheme of the retina of one element. The dielectric employed is quartz with an $\epsilon_r = 3.75$ and a thickness of $350\mu m$ which is greater than $\lambda_g/4$ at 100 GHz. This substrate is double-grounded and a double-slot geometry is used as antenna. In Figure 3.4c the front view of the double slot with the physical model of the diode is shown. Note that the double slot of the ground plane is indicated with the red line.

The simulation is performed using MW-CST using open boundary conditions for the

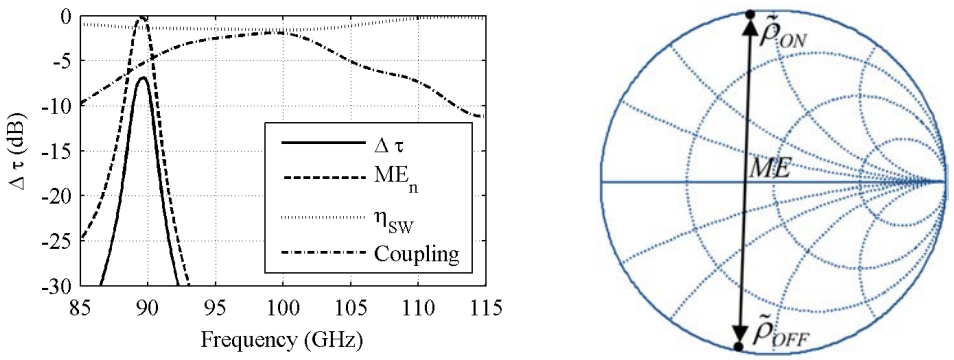

(a) **(b)**

Figure 3.5: (a) $\Delta\tau_{co,il}$, normalized ME, surface wave losses and coupling losses of the system as a function of the frequency. (b) ME of the antenna plotted on a Smith chart.

retina edges and three ports for the illuminator, diode port of the retina and collector respectively. Then, these three ports are loaded with its respective impedances, i.e. the diode is loaded with its junction impedance in ON and OFF state previously calculated in order to finally obtain the $\Delta\tau_{co,il}$. The optimal dimensions of the antenna geometry that maximize this $\Delta\tau_{co,il}$ were obtained after an exhausting number of simulations. Figure 3.5a shows the $\Delta\tau_{co,il}$ as a function of the frequency for the optimal antenna obtained at this frequency band. As it is shown a pick value of -7 dB is obtained at 90 GHz (the maximum $\Delta\tau_{co,il}$ that could be archived is 0 dB). In order to understand the behavior of the system, the $\Delta\tau_{co,il}$ has been decomposed by the following elements (as it has been explained in the previous chapter):

- **Surface wave efficiency** The antenna geometry that reduces the propagation of surface waves over electrically thick substrates is having a double slot over grounded substrate with a double slot. As it is shown in Figure 3.5a by employing this geometry the surface waves losses are less than 1.5 dB in the whole frequency band. Therefore, this does not constitute the main contribution to the losses obtained.
- **Modulation efficiency** At millimeter wave frequencies, the impedance states given by the available devices cannot not be freely chosen by the designer. This implies that the optimization process is based in designing an antenna with a given impedances that matches the impedance of the switching element, in this case, of the PIN diode selected before. As it is shown in Figure 3.5a, the ME achieved has a pick value of 5.78 dB (note that the ME has been normalized to 0 dB, then $ME_n = -0.26\ dB$) when the maximum that can be achieved for this PIN diode impedance is 5.95 dB. In Figure 3.5b the reflection coefficients due to the antenna mode contribution of the diode in ON and OFF state are plotted on a Smith chart, where it can be observed that there is a maximum separation in both states, and therefore, a very good matching between both elements. However, the low bandwidth of the performance of this system is limited by this parameter.
- **Coupling between the retina and collector** As it is shown in Figure 3.5a this parameter corresponds in this particular case to the major loss of the system. Even

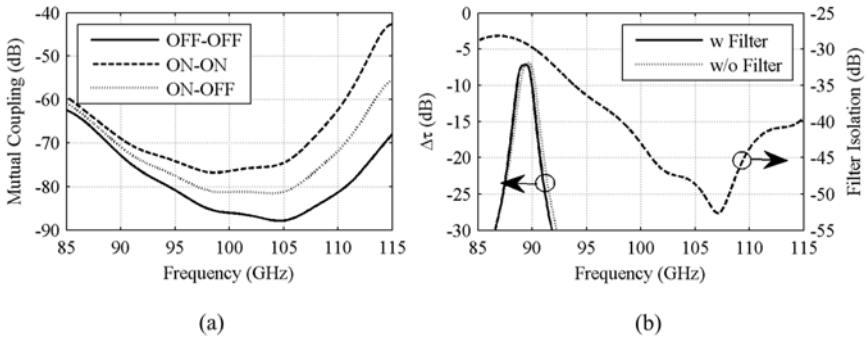

Figure 3.6: (a) Mutual coupling between antenna probe elements. (b) Filter isolation and $\Delta\tau_{co,il}$ corresponding to the antenna simulated with and without filter.

though this contribution can be generally low, in this case due to the high physical blockage produced by the PIN diode package its value is the highest one and is close to -5dB. This parameter, therefore, can be improved by using a smaller and less bulky packaging diode (as it will be shown in the next prototype at 300 GHz where a coupling of -0.5 dB is obtained).

Next, because this antenna will be placed in an array, the mutual coupling between elements needs to be taken into account. The mutual coupling has been obtained by the simulation of the coupling of two antennas for a typical spacing of $\lambda/2$. As it is shown in Figure 3.6a, it falls below -40 dB which therefore can be neglected in the losses account. Note that the double slot geometry improves the mutual coupling as the radiation has a null in the broadside direction therefore, it was already expected a good behavior.

The next element that is designed is an RF-filter that isolates the probe antenna from the bias line used to control the diode. The RF-filter is compound of a series of transmission line steps of length $\lambda/2$ alternating high and low impedance line. The number of steps determines the bandwidth of the filter. In this case, the filter designed is made of 7 step sections providing an isolation of more than 25 dB in the frequency band of interest (see Figure 3.6b). Note that the filter is design to obtain a short-circuit at the entrance ($Z_{in} = 0$) so it is invisible to the antenna as it can be observed in Figure 3.6b, where the $\Delta\tau_{co,il}$ of the antenna with filter and without filter is identical.

All in all, the antenna prototype of the retina for imaging system proposed has been designed to be optimized for the PIN diode employed. The final dimensions of the antenna including the filter are shown in Figure 3.7. Figure 3.7a is the top layer of the antenna where the PIN diode is placed and Figure 3.7b is the bottom layer of the antenna.

3.1.2.1 Prototype Fabrication

In this section, the prototype fabrication is presented. The substrate chosen for the prototype is a 350 μm quartz wafer of 10 mm of diameter. A copper metallization of thickness 0.75 μm is deposited by evaporation on each side of the wafer. The patterning of the wafer is performed with a laser micro-machining which has a precision of 2 μm and a laser point diameter of 25 μm. The previous design already took into account this

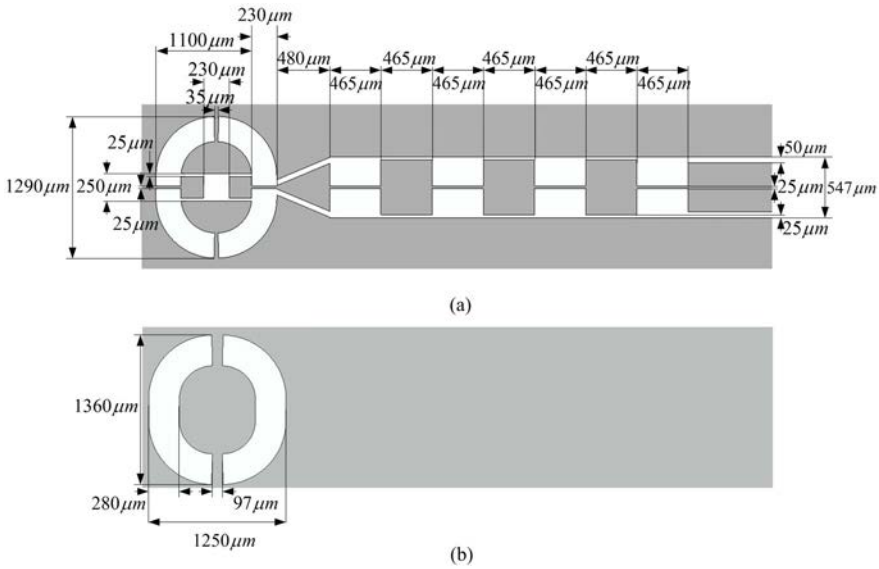

Figure 3.7: (a) Top and (b) bottom layer of the prototype of the retina antenna designed for the imaging system proposed.

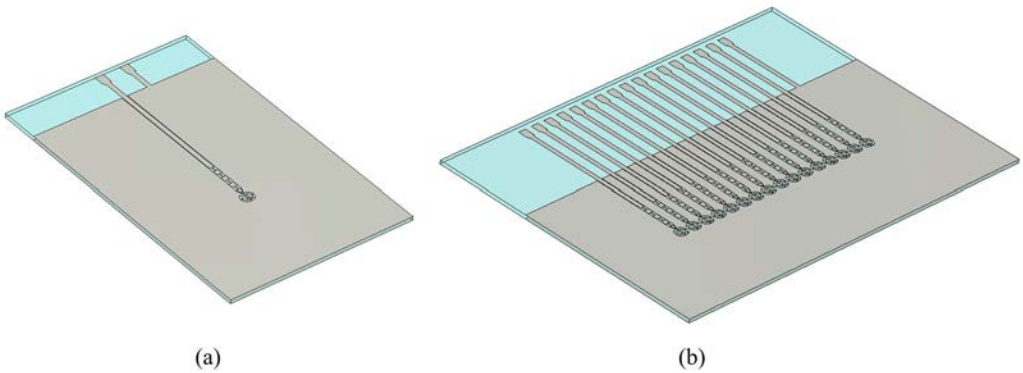

Figure 3.8: (a) One element antenna prototype. (b) Prototype of the 16 elements retina.

restrictions, making the smallest motives of the antenna not smaller than 25 μm.

The goal is to perform two set of measurements which will characterize the analysis performed. Specifically they consist on:

- *One element characterization:* This measurement consists on the characterization of one probe element of the retina. Two waveguides are used as an illuminator and collector and the retina is placed between them. In order to do that, on one hand a one element retina needs to be fabricated as the one in Figure 3.8a. Note that a space of 3λ is left between the antenna and the border of the substrate in order to emulate an infinite substrate. An extra bias pad is added corresponding to the ground connection. On the other hand, a special adapter needs to be fabricated in order to

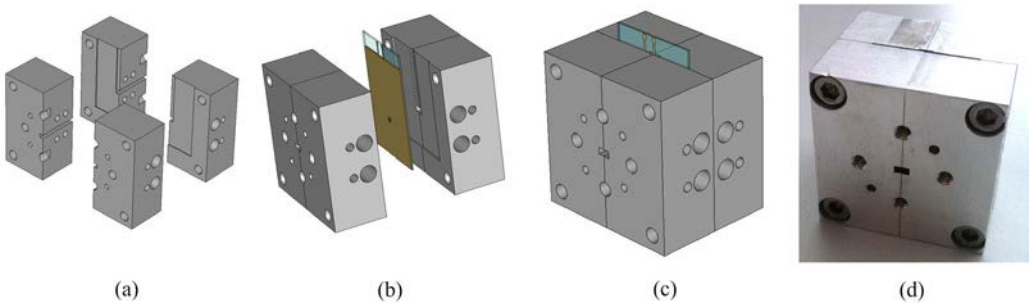

Figure 3.9: (a),(b),(c) Different views of the designed retina adapter. (d) Fabricated adapter

place this element between the waveguides. The design of this adapter is shown in Figure 3.9a,b and c. It is based on a WR-10 waveguide patterned on an aluminium block with two standard flanges UG-387 patterned in each side. The retina profile is placed in the middle as shown in the figure patterned on the waveguide in order to provide a good alignment between the antenna and the waveguide. A cavity of depth 200 μm is patterned on the block in order to avoid short-circuit of the antenna RF filter with the waveguide.

This block has been fabricated in UPC using a Computer Numerical Control machine to perform the patterning of all the elements. It has been fabricated by splitting the block in four pieces (as shown in the Figure 3.9a) and then assembling them using 4 set of screws on each side of the block (see Figure 3.9d).

- *Imaging measurements:* This measurement consists on the characterization of the whole retina within the system. The retina of 16 elements is shown in Figure 3.8b. In this case a special illuminator and collector that is explained in the following section is employed.

Once the designs of the individual antennas and retina have been defined. The next step is to built the mask that will organize these designs in the wafer. The disposition and distribution has been performed in order to maximize the number of designs that fit within the wafer and also to optimize the dicing of the wafer. The mask used for the fabrication is shown in Figure 3.10. As it is shown, 4 individual antennas are placed (2 in the top and 2 in the bottom of the wafer) as well as two whole retinas in the center part of the wafer. The cutting marks are the lines that go through the wafer vertically and horizontally. The two empty spaces on the right side and left side of the wafer are left to perform the calibration and test of the micro-machining laser.

This retina is currently being built. The deposition of the copper in the wafer is performed by Instituto Tecnologico de Materiales (ITMA) in Asturias and the patterning of the laser is performed in the University of Oviedo. The dicing of the wafer will be performed in the National Microelectronics Centre (CNM) a center that belongs to CSIC-Universitat Autonoma de Barcelona (UAB) in Bellaterra.

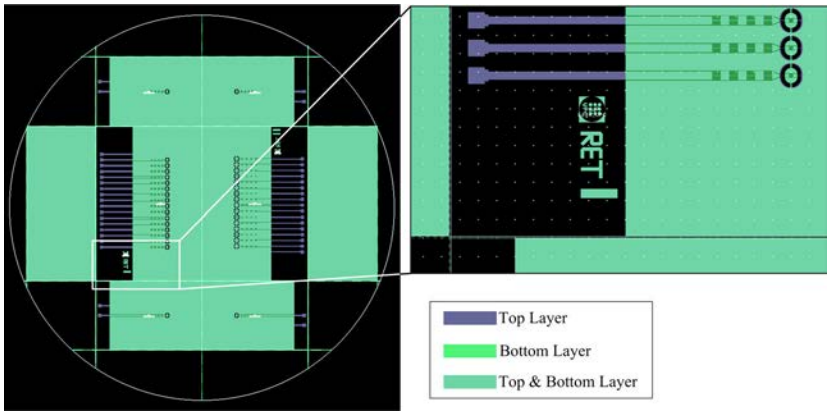

Figure 3.10: Mask set distribution containing the different designs of prototypes at 100 GHz designed.

3.1.3 Collector & Illuminator

The collector is a sectoral horn antenna with an exponential profile in the H-plane, which improves the (near-field) plane-wave character in this plane and the system sensitivity. Based on the reciprocity theorem, the coupling between the collector horn port and the antenna probe placed in the retina is proportional to the field distribution in the collector horn aperture when it is excited from its port. It is clear then, that a uniform field distribution in magnitude in the collector horn aperture maximizes the sensitivity of the system. The illuminator is designed also with an exponential profile like the collector in order to illuminate with a plane wave the sample.

In this section the design of a horn with a constant electric field distribution at its aperture is presented. This horn can be used as illuminator of the sample; on the other hand, when used as a collector a certain distance between the collector and the retina is left in order to avoid the short-circuiting of the horn by the metallic wall of the retina.

3.1.3.1 Illuminator/Collector with Uniform Electric Field Distribution

A horn antenna with polynomial profile was used to extend the region at the antenna aperture over which the power is above -3 dB with respect to its maximum value; that is, to extend the region with a constant amplitude.

The sectoral horn antenna is planned to operate at a central frequency of 100 GHz although it is intended to have a frequency band from 75 GHz to 110 GHz. The antenna is fed by a rectangular waveguide WR-10 with dimensions $2.54 \times 1.27\ mm$. With regard to the feed horn, it was decided to work with a sectoral H-plane horn antenna with an aperture of $31.50 \times 2.54\ mm$. With such dimensions and considering a frequency of 100 GHz, it is possible to place a 16 half-wavelength probe array with a separation of $\lambda/2$ (1.5 mm) between probes at the aperture of the antenna.

The following equations show the expressions used to obtain the polynomial profile of the feed horn, where l_h is the length of the feed horn and a and a_1 represent the

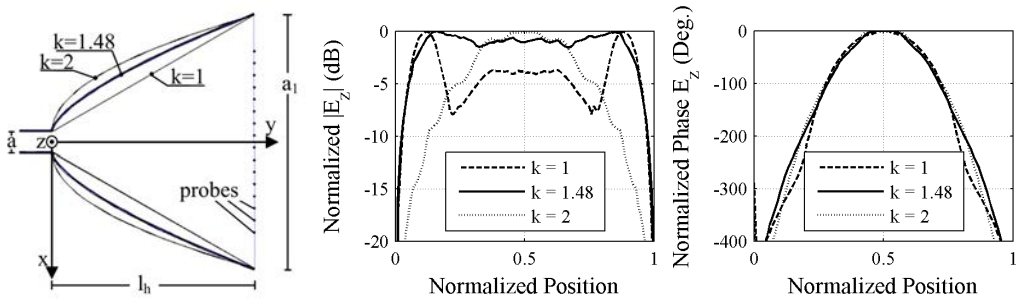

(a) **(b)** **(c)**

Figure 3.11: (a) Sectoral horn scheme for different polynomial profiles k. Normalized field amplitude (b) and phase (c) at the aperture of the horn for different polynomial profiles k at 100 GHz.

width of the waveguide and the width of the feed horn, respectively. These equations are referenced to a Cartesian system whose origin is located at the center of the transition between the waveguide and the feed horn, as illustrated in Figure 3.11a.

$$\begin{gathered} y = l_h \left(\frac{2x'}{a_1 - a}\right)^k \\ x' = \left\{ \begin{array}{ll} x + \frac{a}{2}, & if \quad -\frac{a_1}{2} \leq x \leq -\frac{a}{2} \\ x - \frac{a}{2} & if \quad \frac{a}{2} \leq x \leq \frac{a_1}{2} \end{array} \right\} \end{gathered} \tag{3.1}$$

Different polynomial profiles were simulated using Ansoft HFSS [58]. Figure 3.11b,c shows the results for polynomial profiles with $k = 1,\ 1.48$, and 2 at 100 GHz. The position where the field is measured has been normalized to the width of the aperture a_1. By changing the value of k in the equation of the polynomial profile, it is possible to modify the region of the antenna aperture in which the magnitude of the electric field is above $-3dB$. Since we are interested in a uniform amplitude field distribution, the best result is the one obtained for $k = 1.48$. The phase remains invariant with k but it could be corrected with a lens placed at the aperture of the antenna or with software in the data post processing.

In order to observe the performance of the system for different frequencies, the horn antenna with polynomial profile that is obtained for $k = 1.48$ was simulated for different frequencies along the W-band, the range of frequencies between 75 and 110 GHz (see Figure 3.12). From the results, it can be observed that the field distribution remains uniform along the frequency range. Like the variations in magnitude of the electric field, the phase at the antenna aperture is not strongly affected by frequency in the W-band.

The fabricated horn antenna with polynomial profile with $k = 1.48$ is shown in Figure 3.13. It was fabricated in an aluminium block using a CNC drilling machine in UPC. The block was divided into two pieces and drilled with the CNC. After that, both blocks were assembled together using four metal screws and aligned using two metal pins. The alignment and assembling gap of the two aluminium blocks employed in the fabrication process is critical for the good performance of the horn.

Figure 3.14 shows the simulated and measured reflection coefficient of the horn an-

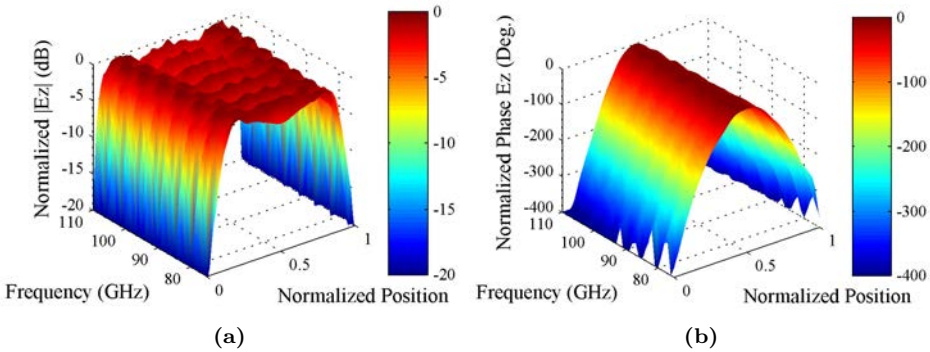

(a) **(b)**

Figure 3.12: Normalized field amplitude (a) and phase (b) at the aperture of the horn as a function of the frequency for $k = 1.48$.

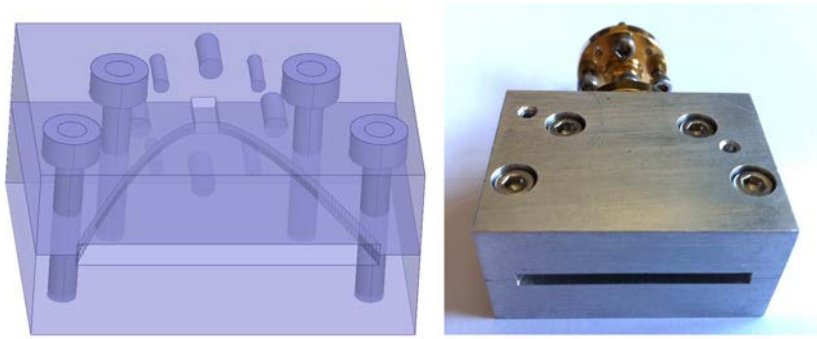

(a) (b)

Figure 3.13: (a) Designed and (b) Fabricated exponential sectoral horn based on the designed described.

tenna. As it can be observed, both, simulation and measurements of the S_{11} of the the horn are always below $-15\,\text{dB}$ for the frequency band of interest, providing a good performance and agreement with the simulations in the whole band.

3.1.4 Measurements

A set of measurements were performed using an initial prototype of retina. This measurements were principally to evaluate the imaging capabilities of the overall system. The fabrication of this retina was performed in UPC with a laser which could fabricate with minimum track/gap of 100 μm with a precision of 10 μm. A double layer design could not be fabricated due to the lack of alignment between both layer. Therefore, with this constraints a single layer retina was designed with a thinner substrate and a double slot antenna (which has a improved behavior from a single slot). The substrate chosen was an Arlon CLT with a permittivity of $\epsilon_r = 2.2$ and a thickness of 127 μm corresponding to $0.06\lambda_g$ at 100 GHz. The substrate has a metallization of 9 μm of copper. The dimensions of the double slot and retina were optimized to obtain a high ME. The final fabricated

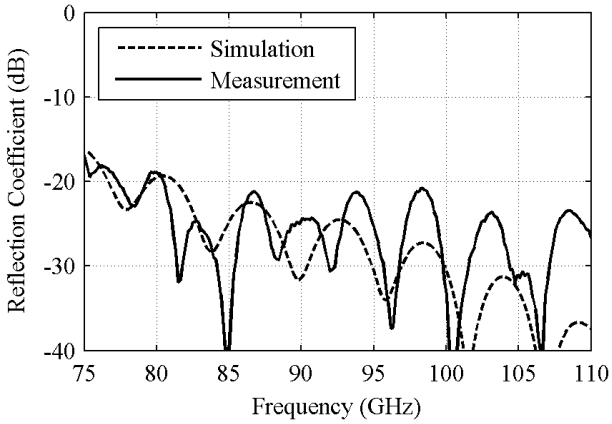

Figure 3.14: Reflection coefficient of the fabricated horn.

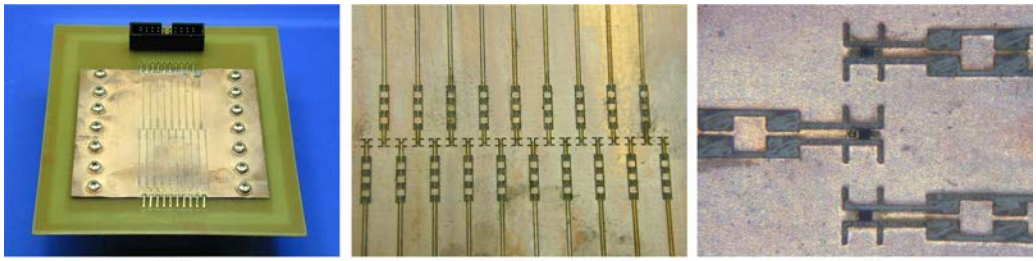

Figure 3.15: Image of the fabricated retina.

of the retina is shown in Figure 3.15. Because the substrate was so thin and malleable, a retina holder was fabricated in order to provide stability to the retina (see Figure 3.15a). The PIN diodes were manually assembled on the retina using polyepoxide (see Figure 3.15b, c).

A PCB was designed and fabricated in order to control the switches of the retina. This PCB consisted on a Programmable Integrated Circuit (PIC) micro-controller PIC18F2550 which was also programmed to communicated with the computer through the Universal Serial Bus (USB) port. A picture of this board is shown in Figure 3.16, where it can be observed the PIC and the output ports where the feeding lines are connected. A line of transistors were added to the outputs of the PIC in order to provide enough current to each diode.

Different measurement set ups were assembled and studied to demonstrate experimentally the operational performance of the system proposed. In the following section, the system calibration and the imaging results will be presented.

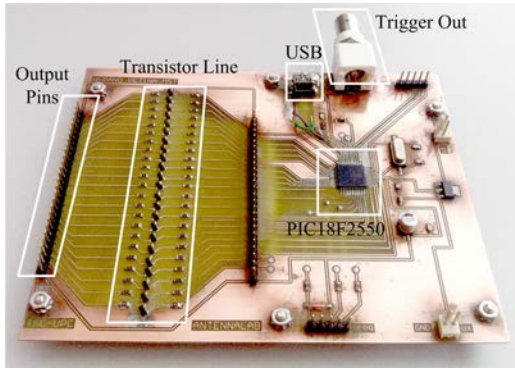

Figure 3.16: Image of the fabricated PCB that generates the LF-modulation of the switches.

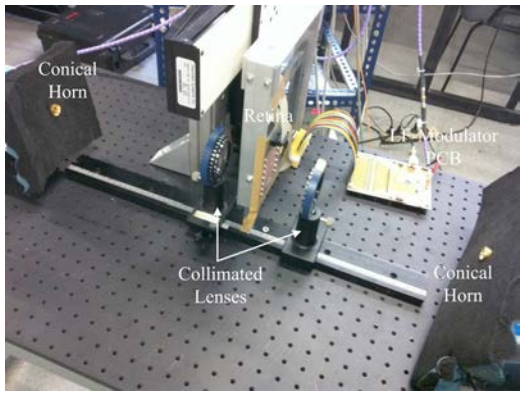

Figure 3.17: Set up used for the retina calibration.

3.1.4.1 System Calibration

The first measurements performed were a calibration and testing of the modulation capabilities of the retina. A preliminary set up was assembled consisting in placing the retina between a pair of collimating lenses and two conical horn antennas working as illuminator and collector (see Figure 3.17). The modulation board governs the retina providing the concurrent modulation of each probe of the retina and also triggering the Vector Network Analyzer (VNA) using its external trigger.

The retina was aligned with two mechanical stages that moved the retina horizontally and vertically in order to be in the focus point of the two collimating lenses. Afterwards, the retina, with all the antennas being modulated at the same time, was displaced horizontally every 0.5 mm using the mechanical stage, and the field in each position was captured at the collector horn with the network analyzer. Each element of the retina was modulated at a different low frequency, i.e each probe was modulated at a frequency that doubles the frequency of the previous probe. For example, if the first probe is modulated at 4 kHz, the second would be at 8 kHz, the third at 16 kHz and so on. This fact avoids the aliasing among all the multiple harmonics of each probe according to the Nyquist rate

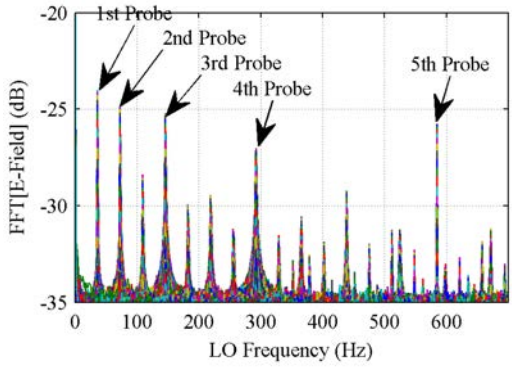

Figure 3.18: FFT of the received field at the collector.

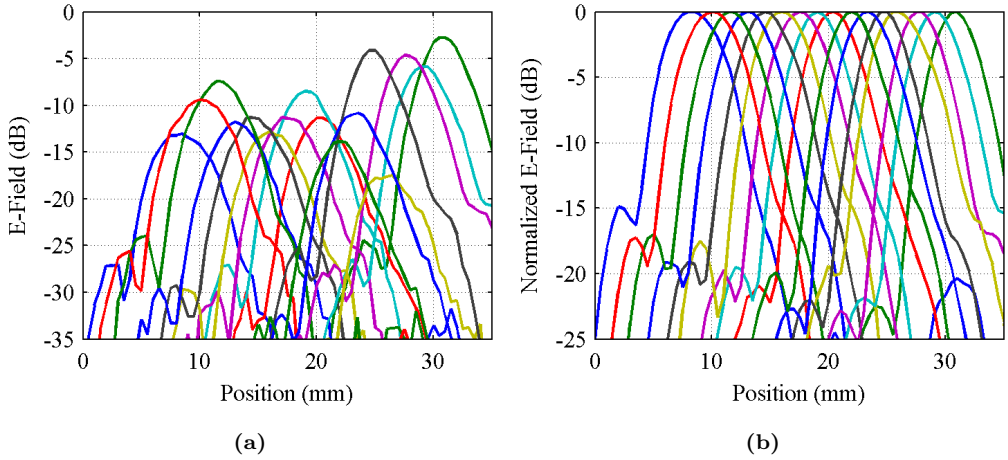

(a) **(b)**

Figure 3.19: (a)Non-normalized and (b) Normalized field amplitudes from each probe.

criteria where $f_i \geq 2BW$ being BW the bandwidth of the channel.

In Figure 3.18 it can be observed the Fast Fourier Transform (FFT) of the received signal at the collector at 100 GHz, when five elements are modulating simultaneously. Each peak corresponds to the scattered field received at each probe. It can be observed how the probes are being modulated doubling the frequency from the previous one, i.e the first is modulated at 36 Hz, the second at 72 Hz, the third at 144 Hz, the forth at 288 Hz and the fifth at 576 Hz. The multiple harmonics generated by each probe do not interfere with the desired fields. All the images superposed within the graph corresponds to the field in each of the position of the retina. Therefore, because all the probes have gone through the same positions, in theory, all the peaks from each probe should have the same amplitude as the expected behavior of each antenna is the same. These variations are due to inaccuracies in manufacturing of the antennas, mounting the diodes and differences on the theoretical property values of the components used.

In Figure 3.19a the field amplitude captured now by all the 16 modulated probes as

a function of the displacement is shown. As a result, each probe describes the profile field amplitude given by the collimating lens used in the set up. The figure shows how each probe describes the lens profile at a different dynamic margin, i.e each probe has a different peak amplitude. However, if this amplitude is normalized, each probe describes a profile that is practically identical, as shown in Figure 3.19b. This measurement was performed with a network analyzer in continuous wave (CW). The IF bandwidth was set to 30 kHz allowing a simultaneous capture of all the probes. An averaging of 10 samples was chosen as a trade off between measurement time and the SNR. From Figure 3.19 and 3.19b, the SNR can be obtained if substracting the field peak level by the first lobe that appears in the profile at -15dB from the first probe which will correspond to the noise level. Taking advantage of the fact a high bandwidth from 75 GHz to 100 GHz is available, a gating in the measured fields is performed in order to diminish the possible reflections caused by the different elements of the set up.

With these measurements, a variation in the response of the different probe elements of the array is observed and therefore a calibration of each probe is required in order to have a good performance of the system.

3.1.4.2 Imaging Results

The final system setup was assembled (see Figure 3.20a)using the previous retina and the illuminator and collector presented section 3.1.3. In this section, the experimental results obtained with the system are shown and analyzed. The imaging scenario consists in placing one or two circular metallic cylinders in front of the retina to perform imaging as shown in Figure 3.20. This scenario allows to analytically compute the scattered fields and retrieve the theoretical image by using a tomographic algorithm as explained in the previous chapter.

In order to minimize the number of reflections, the differential measurement of the same scenario without the object under test (the so called "empty chamber") is used for the image reconstruction and calibration of the system. Moreover, an averaging and a gating are used as before in order to diminish the noise and the reflections caused by the different elements of the set up.

The distance between the illuminator horn and the retina is 4 cm and the retina is placed in front of the collector horn at a distance of less than 1 mm so it does not short-circuit the electric field at the aperture of the horn. Different images were taken with the system described using metallic cylinders of 2 mm of diameter. In Figure 3.21, 3.22 and 3.23 tomographic images are shown corresponding to images taken of one cylinder and of two cylinders. The figures on the left correspond to images obtained after measurements with the setup and the figures on the right correspond to the expected results after simulations. It can be observed that the objects under test are detected successfully and placed at the expected position with a tolerable level of noise. Further improvements would require a better calibration of the retina and a better alignment of the different components of the system.

Both, simulations and measurements contain multiple and high-contrast scattering factors corresponding to non linear and frequency dependent factors. These factors can be smoothed and reduced by using multi-frequency and multi-view techniques as shown

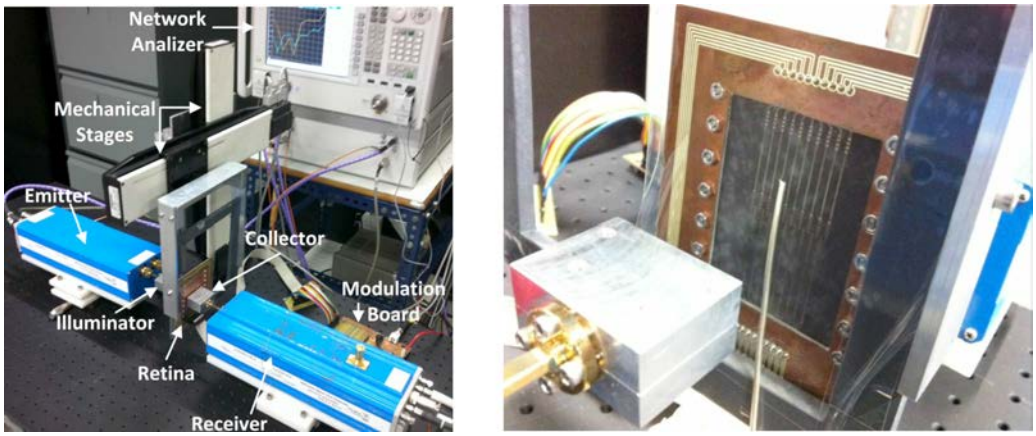

Figure 3.20: Measurement setup.

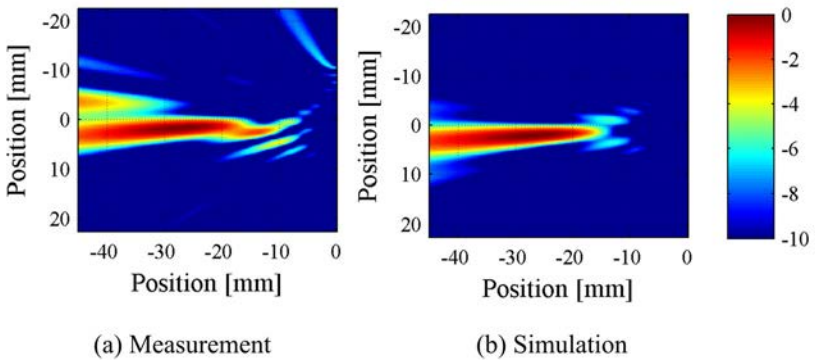

Figure 3.21: One metallic cylinder placed at 27 mm from the retina and displaced 2 mm.

in the previous chapter.

3.2 One Element Probe Antenna Characterization at 300 GHz

The design procedure and characterizaton previously introduced can be extended for systems at higher frequencies. In this section, a prototype of a retina using a Schottky diode and working at 300 GHz is presented. The development of millimeter wave and submillimeter wave components and systems still faces many challenges and limitations. The switching technology currently that is still under development are Schottky diodes, which are employed in heterodyne receivers for their frequency mixing capabilities. This section will use this Schottky diodes as switching elements for the near field system presented before. Chalmers University are currently developing Schottky diode switches allowed us to access to this technology through a collaboration. The design and characteristics of the Schottky diode shown in this thesis correspond to the ones that they are currently

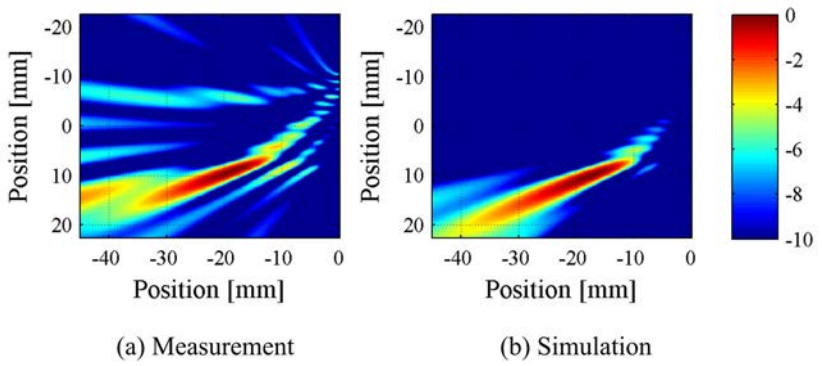

Figure 3.22: One metallic cylinder placed at 18 mm from the retina and displaced 10 mm.

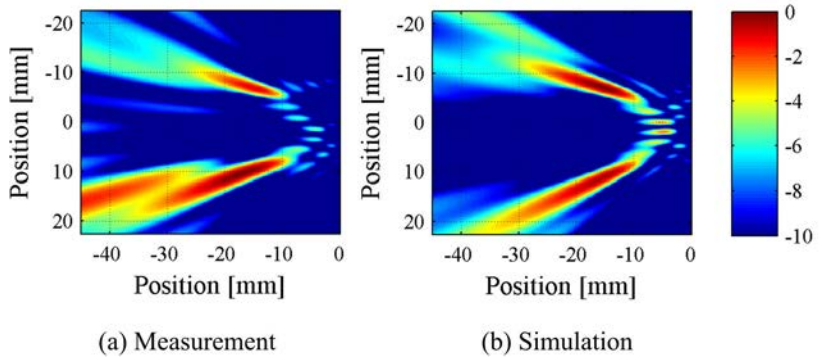

Figure 3.23: Two metallic cylinder separated 1cm from each other placed at 15 mm from the retina.

developing.

This section presents the design of a one element characterization that was intended to characterize the diode and the retina capabilities and performance at higher frequencies. Next, a full detail of the characterization of this switch is presented.

3.2.1 Switching Element Characterization - Schottky Diode

Schottky diodes are junction diodes as the PIN diode, but in this case the junction is formed from a metal-semiconductor junction, rather than a p-n junction, which reduces the capacitance while increasing the switching speed. This junction formed between the metal and the semiconductor once they are in contact is responsible for its current-voltage and capacitance-voltage behavior, and therefore, its impedance.

The diode used for the prototype corresponds to a Schottky varactor diode with only one anode. The physical model of the diode is shown in Figure 3.24b. The green substrate of the model corresponds to a layer of Gallium Arsenide (GaAs) which is a semiconductor commonly used to fabricate these kind of devices. The yellow parts of the model

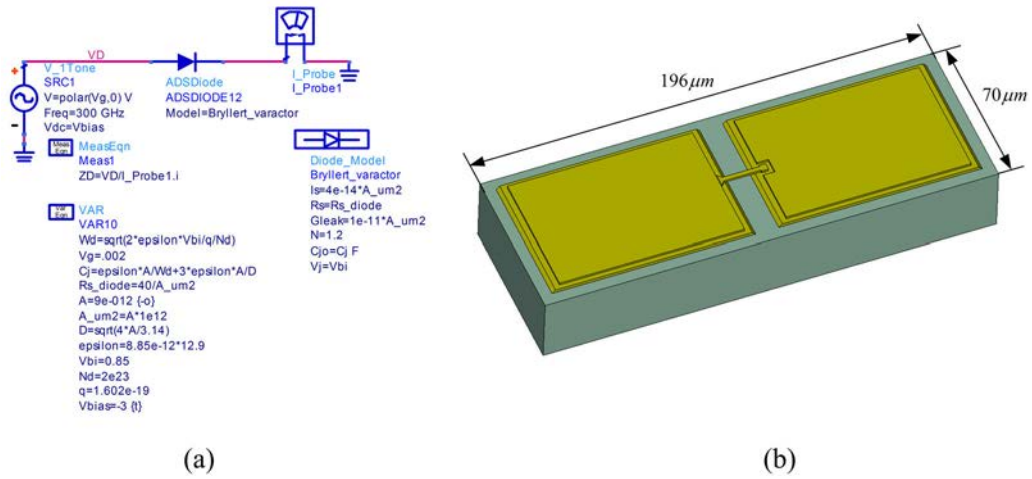

Figure 3.24: (a) Equivalent circuit and (b) Physical model of the Schottky diode used for the prototype.

correspond to gold. The finger shown in the middle corresponds to the anode whose area will highly variate the behavior of the junction. Figure 3.24a corresponds to the equivalent circuit model of the junction. As it is shown, the area of this anode plays an important role in the intensity value of the diode for a certain voltage, and therefore, in the impedance behavior. For instance, Figure 3.25 shows the junction impedance for a diode as a function of the frequency for ON and OFF state for an anode of area 9 μm^2 (a) and 2 μm^2 (b). The bias voltage in ON and OFF state of the diode is $V_{ON} = -3\ V$ and $V_{OFF} = 0\ V$ respectively. As it is shown, by reducing the area, the reactance of the impedance becomes more capacitive. Note that when reducing the area, both states ON and OFF contain a high reactance part, however, the difference between states is higher and consequently its behavior improves as shows the ME of Figure 3.26. The ME improves by 1.2 dB (from 2.9 dB to 4.1 dB) by reducing the anode area.

Figure 3.27 shows the dependence between the voltage applied to the diode and the junction impedance at 300 GHz. As it can be observed, having a controllability of the voltage allows the selection of the impedance. In this case, the voltage selection has been $V_{ON} = -3\ V$ and $V_{OFF} = 0\ V$ in order to leave a safety margin to the instabilities that occur at 0 V, and also also stay in the safety operational level of the diode.

Therefore, once having determined the operational bias and physical dimensions of the diode, the antenna geometry is designed in order to match correctly to its impedance. In this case, the antenna impedance at 300 GHz that needs to be designed for is $Z_T = 91 + 247j\ \Omega$.

3.2.2 Antenna Design

The procedure followed for the design of the antenna is the same followed for the previous prototype at 100 GHz. The maximization of the differential transmission coefficient $\Delta\tau_{co,il}$ is the key parameter to optimize. The basic simulation scenario in this case is the same as

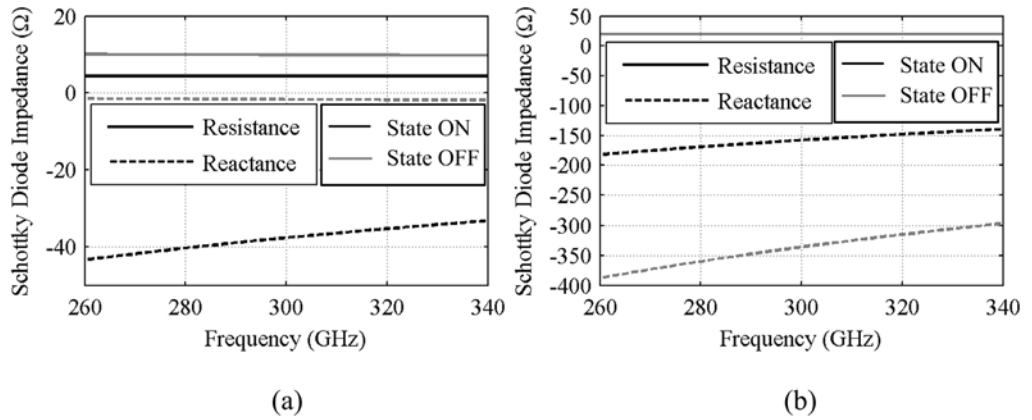

Figure 3.25: Junction impedance of the Schottky diode in ON and OFF state for an anode area of (a) 9 μm^2 and (b) 2 μm^2.

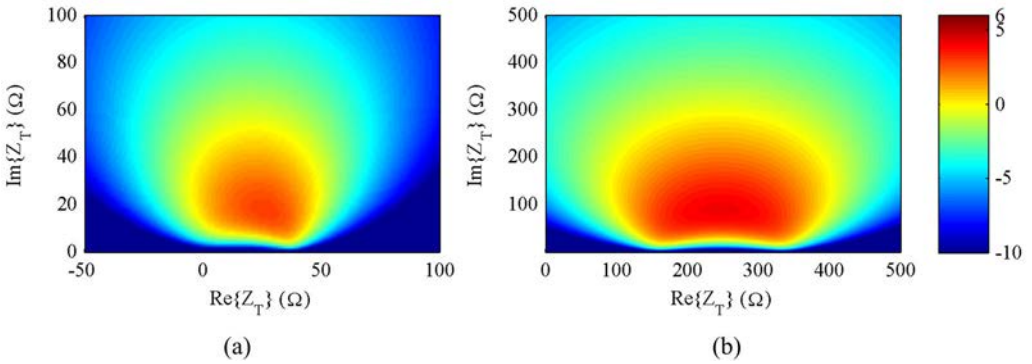

Figure 3.26: ME as a function of the antennas impedance for a Schottky diode with an anode area of (a) 9 μm^2 and (b) 2 μm^2.

in Figure 3.4. Note that in this case the physical model of the diode is the one in Figure 3.24 and it will be flip-chip soldered on the antenna (upside down into the antenna).

The dimensions of the antenna were optimized in order to obtain a maximum $\Delta\tau_{co,il}$, and a maximum value of -5.2 dB at 300 GHz was achieved. In Figure 3.28a it can be observed that in this case, while the surface wave efficiency and coupling efficiency are high (each has -0.65 dB of losses), the main contribution to the loss of $\Delta\tau_{co,il}$ it is due the ME which in this case is 2.1 dB (note that the ME has been normalized to 0 dB, then $ME_n = -3.9\ dB$). This fact is understandable as the behavior of the Schottky diode is worse in terms of adaptability to the antenna. From the previous analysis of the diode it was observed that the maximum ME that was obtained at 300 GHz was 4.1 dB (instead of 6 dB). In Figure 3.28b the reflection coefficients due to the antenna mode contribution of the diode in ON and OFF state are plotted on a Smith chart, were the behavior is not as good as in the previous prototype at 100 GHz where the ME achieved was significantly greater (5.78 dB).

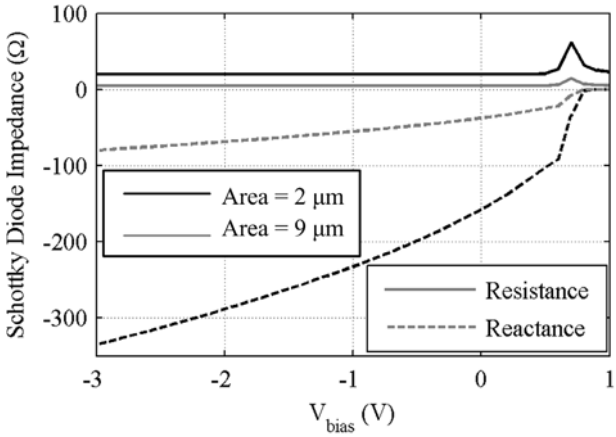

Figure 3.27: Junction impedance of the Schottky diode at 300 GHz as a function of the biasing voltage V_bias applied.

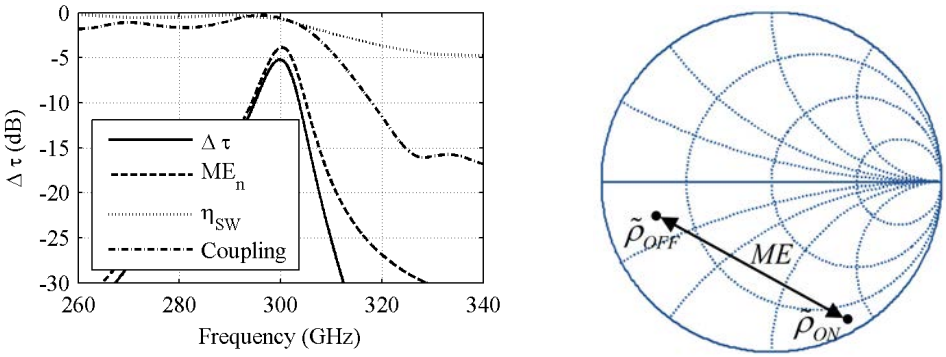

(a) **(b)**

Figure 3.28: (a)$\Delta\tau_{co,il}$, normalized ME, surface wave losses and coupling losses of the system as a function of the frequency. (b) ME of the antenna plotted on a Smith chart.

The mutual coupling is shown in Figure 3.29, where two antennas have been simulated and the coupling parameters for each combination of diode state have been taken. In this case, the results are higher than the previous at 100 GHz due to the smaller physical blocking produced by the diode package. By choosing different probe modulations (ON-OFF, OFF-OFF or ON-ON) different mutual coupling are obtained and the performance can be improved.

The RF-filter that isolates the probe antenna from the bias lines of the Schottky diode is also compound of 7 series of steps of $\lambda/2$ of transmission lines of high and low impedance. The isolation achieved is more than -25 dB in the frequency band and it is invisible to the antenna, i.e the $\Delta\tau_{co,il}$ with and without the filter is not affected (only an insignificant shift in the peak frequency).

Figure 3.29 shows the dimensions of the final prototype antenna. The top plane of

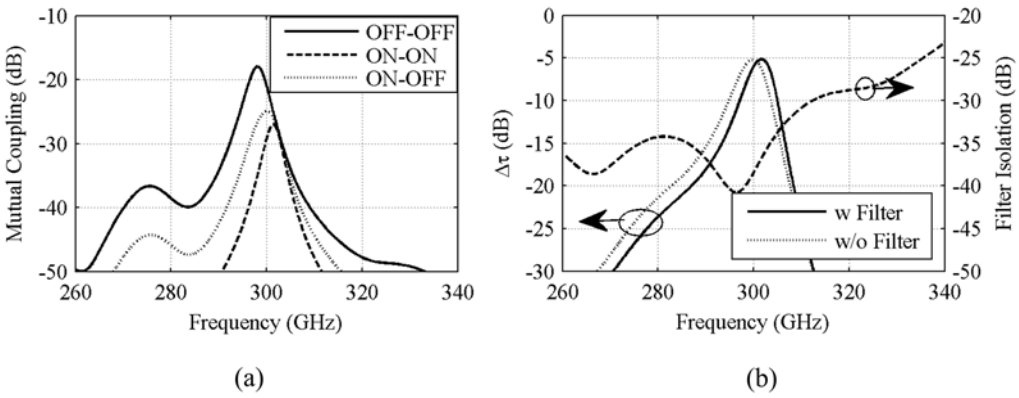

Figure 3.29: (a) Mutual coupling between the antenna probe elements. (b) Filter isolation and $\Delta\tau_{co,il}$ corresponding to the antenna simulated with and without filter.

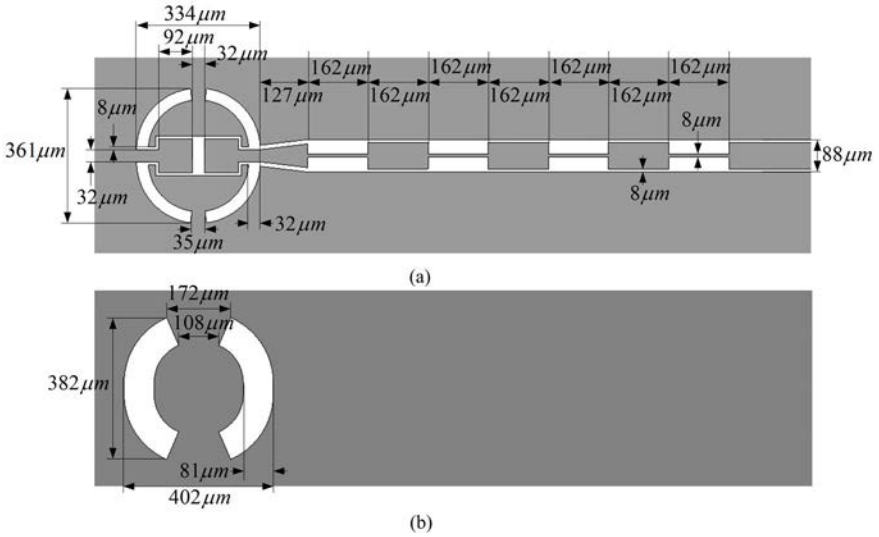

Figure 3.30: (a) Top and (b) bottom layer of the prototype of the retina antenna designed for the imaging system proposed.

the antenna is where the Schottky diode is placed upside down. Appendix A presents the next steps to fabricate and measure a prototype using the design shown in this section.

3.3 MST MEMs Retina Prototype

RF-MEMS switches currently employed at microwave frequencies are a high potential switching technology that can be employed at millimeter and submillimeter wave frequencies because of its small dimensions, high isolation and low conduction losses [59] . Although MEMS technology is increasing its frequency as the time goes, it is still func-

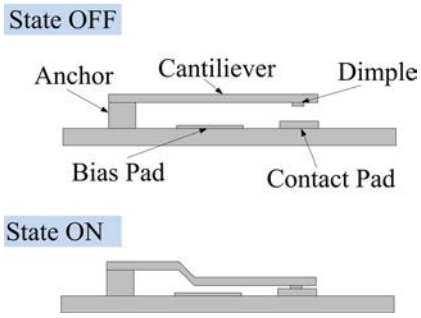

Figure 3.31: RF-MEMS switch diagram.

tioning mainly in the microwave regime. This is why in this case, two prototype retinas were fabricated at lower frequencies, one in the 50-75 GHz band, and another in the 75-100 GHz band. These prototype were intended to measure the technology capabilities of the available technology at the moment.

RF-MEMS switches offer in some cases a greater performance than semiconductor switches because of their potential lower losses, their quasi-zero power consumption and the possibility of being monolithically integrated within the antenna structure. The goal of this section is to study integration capabilities of the RF-MEMS in the antennas, which for this type of retinas could be beneficitial because of the required number of switches (proportional to the number of pixels). However, the robustness and reliability of this switches (even in individually packaged RF-MEMS) is currently inferior to the semiconductor switches.

3.3.1 Switching Element Characterization - RF-MEMS

RF-MEMS are characterized by its mechanical movement that opens or short-circuits the RF-system. Between the different type of RF-MEMS that can be found, this thesis is focused in the metal contact RF-MEMS switch which uses physical contact triggered by a DC voltage.

Figure 3.31 shows the structure of the RF-MEMS used in this thesis, i.e the cantilever type. The main part of the switch is the cantilever which is the movable part of the switch. The cantilever is supported by the anchor by one side leaving the other side connected or disconnected depending on its positon (i.e. state ON or OFF the switch). The dimples hang from the bottom part of the the cantilever and are responsible for connecting the cantilever and the contact pad and therefore activating or deactivating the switch. The state of the switch will be triggered by an activation voltage normally between 35 V and 85 V applied to the bias pad. The actuation mechanism of the switch is electrostatic, therefore, the currents over the bias lines are negligible and also the power consumption. Because of this quasi-zero power consumption, the biasing lines are made of high-resistivity material that actuates as an RF-filter that provides the antenna an isolation from the biasing circuitry.

As it has been presented in the past sections, in order to design the retina, it is

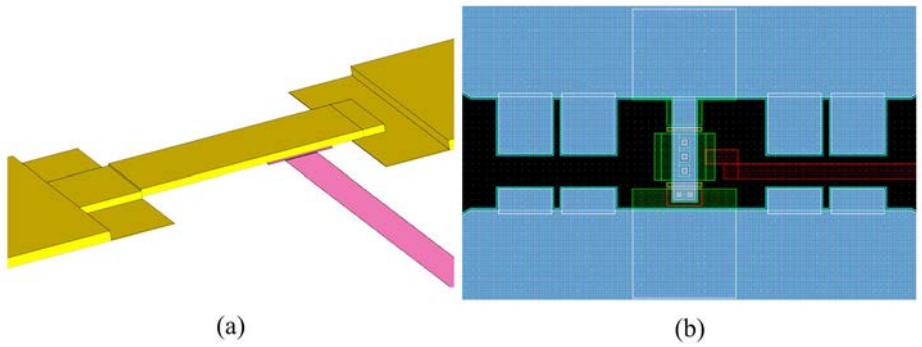

Figure 3.32: (a) 3-D Structure of the RF-MEMS. (b) Mask of the RF-MEMS

required a load that presents two highly differentiated states, and that it is as constant in frequency as possible. Because the specific parameters of the RF-MEMS switch were not fully known at the design stage, an ideal RF-MEMS was considered, emulating a short-circuit and an open circuit for the whole frequency range. Therefore, for the OFF state, since the capacitance is extremely small all RF-MEMS present basically an open circuit impedance. On the other hand, for the ON state, the MEMS switches become basically RL circuit, and the impedance can displace from the ideal short-circuit state.

Figure 3.32a shows the 3-D diagram of the RF-MEMS, while Figure 3.32b shows the structure of the mask that contains the elements presented. Their fabrication process consists in a complex multi-layered lithography serial processes, that are sequentially performed until the final structure is obtained. The RF-MEMS optimization and the prototype retinas fabrication were developed in a collaboration between the USU and UPC. The fabrication process and the final fabrication of the prototypes were performed in the installations of Cornell Nanoscale Science and Technology Facilities, Ithaca, New York.

3.3.2 Retina Prototype

As it has been explained before, the parameters of the RF-MEMS were not known at the design stage so the design process was performed using an ideal switch. Therefore, the goal of these prototypes was to study the current micro-fabrication processes, the RF-MEMS switches performance and its capabilities to be monolithically integrated within the antenna. Two retina prototypes were designed using bowtie antennas: one at a frequency of 50-75 GHz and another one at 75-100 GHz. Taking advantage that in this case the stepped impedance filter was not required, 2-D array of 4×4 antennas was fabricated.

The final dimensions of the antenna elements are shown in the top of Figure 3.33 and the mask design with the antenna and the switch is shown at the bottom. Some metallic bars were added next to the RF-MEMS in order to create uniformity among the area next to the switch (as it can be observed in Figure 3.32b) and protection from the some aggressive etching that occur during the fabrication.

The mask set designed with all the antenna prototypes is presented in Figure 3.34.

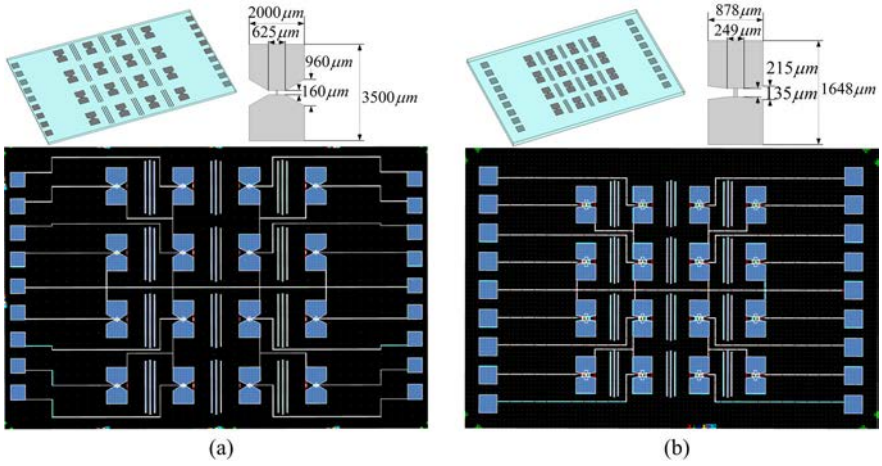

Figure 3.33: (a) Retina prototype at 50-75 GHz. (b) Retina prototype at 75-100 GHz

It contains both retina prototypes, the bigger one in the middle part of the wafer and the second one in the left part of the wafer. The rest of the antenna designs belong to other integrated antennas for different purposes. Different sets of switches were placed around the wafer in order to perform an individual characterization of the RF-MEMS performance. The alignment marks are used to align the different layers of the fabrication process. They are placed in different areas of the wafer symmetrically distributed in order to help their finding with the contact aligner. Two types of alignment marks are used depending on the layer, one is used to align with the top layer and the other one is used to align the bottom layer. The lithography marks are used to control the quality of the lithography process, i.e the development of the photoresist and the etching of the metal. It consists on different horizontal and vertical lines of different widths and different spacing that can be checked at the microscope after each process. In the following section, the microfabrication processes and tools are described.

3.3.3 Fabrication Process

The fabrication process was carried out in CNF which allows the fabrication of planar structures with a lithographic process resolution between 1 and $2\mu m$. The fabrication techniques and tools are chosen depending on the materials employed and on this case on the multi-layer structure (the use of a certain process on a layer can affect negatively to the rest of the multi-layer structure).

The lithographic process consists on the deposition of a layer of the material to be patterned. Different deposition processes can be employed, such as evaporation, sputtering, spinning and electrolatting. To perform the patterning a thin layer of photoresist is coated over the previous material. This photoresist material changes its properties when exposed to ultra-violet radiation. Therefore, with the masks which contain the patterns of the design, certain areas will be covered or exposed to this light using image projection or e-beam lithography. After that, a developing process is performed, consisting on

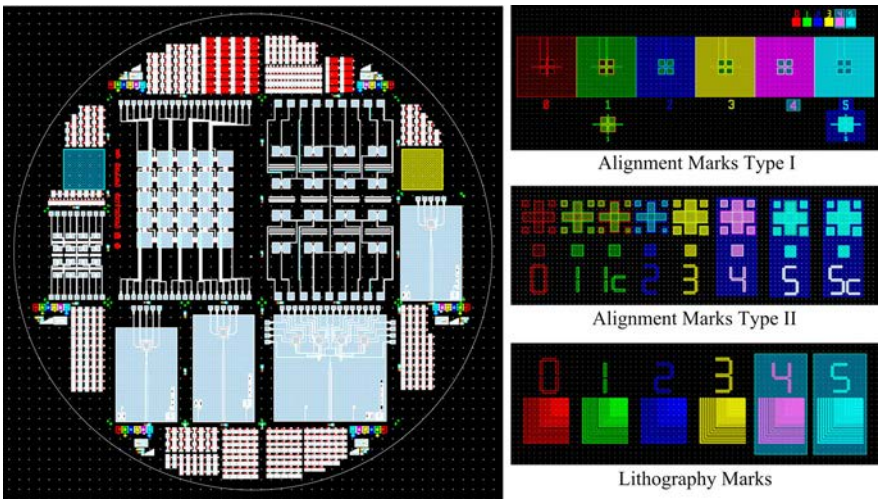

Figure 3.34: Mask set of the 6 layers that contains all the prototypes.

removing the parts of the photoresist that have been exposed to the light (in case of negative photoresist). Next, once the design is patterned over the photoresist, an etching of the first material deposited is performed in order to eliminate the material from the parts that are not protected. This etching can be performed using wet etching (based on liquid chemicals) or dry etching (based on high energy ions). Finally, the remaining photoresist is stripped from the wafer leaving only the patterned material.

The fabrication of the antennas consisted on 172 individual processes performed in the cleanroom and can be summarized in the following major steps:

1. *High-Resistivity Lines Deposition - Mask 1*

   The feeding lines of the RF-MEMS made of TaN are deposited over the quartz wafer. The deposition is performed by a sputtering machine and dry etching using CF_4 as plasma etchant.

2. *Gold Layer - Mask 2*

   This layer consists on the deposition of a thin layer of gold over the quartz. First, a thin layer of 160 A of chrome is deposited using evaporation over the wafer of quartz in order to provide the adherence, and then a layer of 3000 A of gold is evaporated on top. Both layers are then patterned using wet etching, first the gold and then the chrome using its respective wet-etchands. After this process the RF-MEMS switch looks as in Figure 3.35 were the bottom part of the RF-MEMS is shown (without the cantilever).

3. *Sacrificial Layer - Mask 3*

   The sacrificial layer serves as a suspender for the RF-MEMS cantiliever. In this process, a thick layer of Poly-Methyl Methacrystalate (PMMA) is deposited by spinning in two times in order to achieve the desired thickness of 1 μm. Because the PMMA has a similar organic nature as the photoresist used for patterning, the masking is performed with an evaporated thin layer of 530 A of titanium on top of

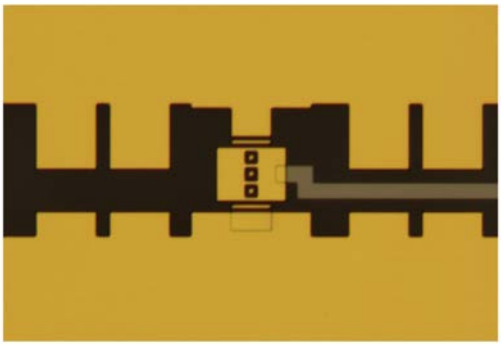

Figure 3.35: Optical image of the RF-MEMS without the cantilever.

the PMMA. The patterning is performed using wet etching with Hydrofluoric Acid and the undesired PMMA is removed using O_2 dry etching.

4. *Dimples Layer - Mask 4*

   The dimples, which are the contact points of the cantilever with the contact pads are created by patterning small holes in the sacrificial layer (patterning half-way instead of all the way). The patterning in the PMMA layer using the same process as before (depositing a thin layer of titanium and then using wet etching and O_2 dry etching for the patterning).

5. *Gold Layer - Mask 5*

   A thin layer of 2000 A of gold is deposited using evaporation and patterned. A seed layer of chrome is used for the adherence of the gold over the PMMA.

6. *Electroplating - Mask 6*

   Because of the large thickness of the gold layer required in the cantilever, the previous layer of gold is grown using the electroplating process until reaching a final thickness of 4-5 μm. This is one of the critical points of the fabrication process due to the uniformity issues that this process produces within the wafer.

7. *Dicing*

   The designs are diced using a diamond blade. It is also a another a critical point of the process due to the high vibrations that this technique produces over the structure. Therefore, the PMMA in the RF-MEMS is maintained during this process to provide robustness.

8. *Release*

   This process consists in the realease of the RF-MEMS and leaving the cantiliever in the final suspension state. Thus, the sacrificial layer is removed by using wet etching and dried using a critical point drier technique. When the RF-MEMS are in the wet solution, there are no risks of damages, the possible structural damage that could cause the dry etching is solved by using the critical point dryer tool.

At this point the antennas are ready to be measured.

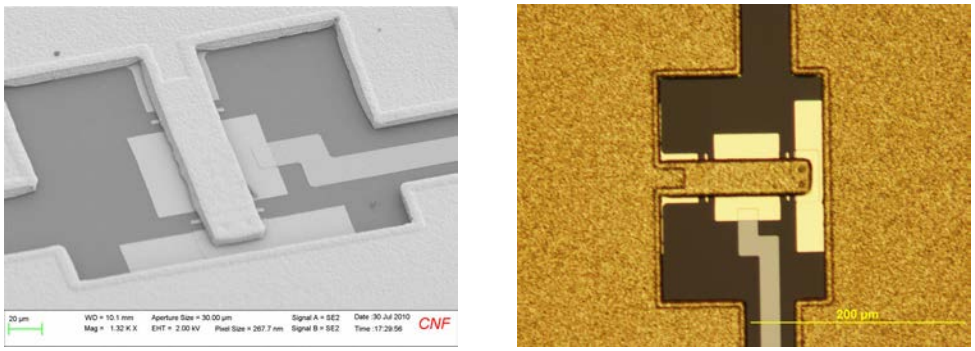

(a) (b)

Figure 3.36: (a) SEM and (b) Optic image of the fabricated RF-MEMS.

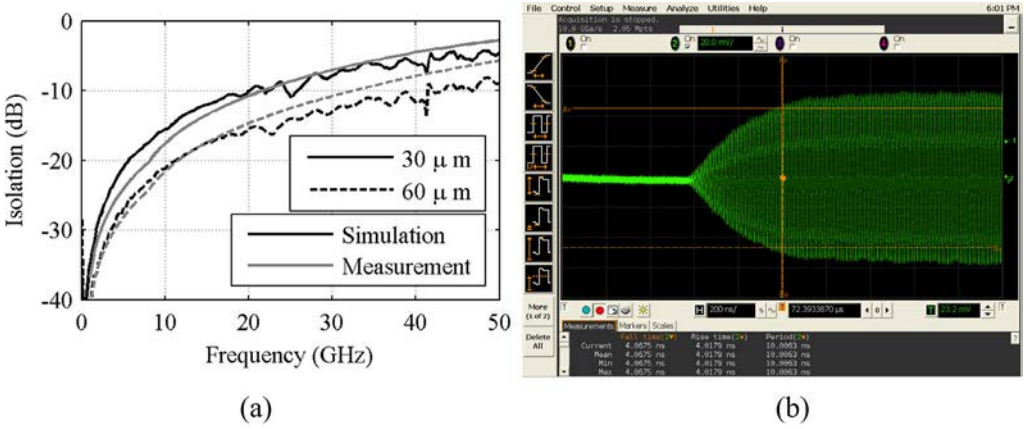

Figure 3.37: (a) Isolation and (b) switching response of the RF-MEMS

3.3.4 Measurements

Figure 3.36a shows an optical image of a micro-fabricated switch. It can be clearly observed the different parts of the RF-MEMS mentioned before. Note also the different texture and color that can be appreciated between evaporated (shiny smooth golden areas) and electroplating gold (grain darker golden areas). This roughness could be an issue for higher frequencies as it could produce a degradation on the antenna or switch performance, therefore other techniques like evaporation or sputtering are recommended. Figure 3.36a shows the image of the RF-MEMS using a Scanning Electron Microscope (SEM) microscope. This microscope provide a 3-D looking image of the RF-MEMS where the cantiliever is shown suspended on top of the contact pads.

In order to peform the characterization of the RF-MEMS several of those were included in CPW lines where an easy and realiable testing could be performed. Measurements were performed using a GSG-probe station and an Agilent PNA Network Analyzer working up to 50 GHz. Figure 3.37a shows the transmission coefficient for a RF-MEMS in ON and

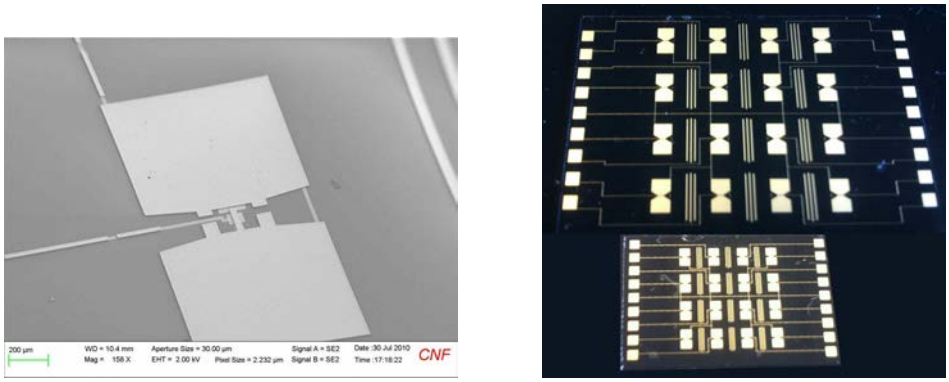

(a) **(b)**

Figure 3.38: (a) SEM image of an element of the fabricated retina. (b) Photograph of the fabricated retinas. The top retina corresponds to the 50-75 Ghz band and the bottom one to the 75-100 GHz band.

OFF states. The RF-MEMS DC activation voltage between 40 and 70 V depending on the thickness of the cantaliever switch (due to the non-uniformity of the gold deposition from the electroplating process). Results were compared with the RF-MEMS in HSFSS simulation software. The activation time of the switch is around 75 μm (see Figure 3.37a) which is typically low considering this type of switches.

Figure 3.38a shows a SEM image of a dipole with the integrated RF-MEMS of one of the fabricated retinas. In Figure 3.38b it is shown the picture of the final fabricated retinas. The RF-MEMS in the antennas where individually tested directly on-waver after their fabrication. The yield of the microfabrication process was less than 40%, i.e. less than 40% of the RF-MEMS used by the antennas worked as expected, where the rest were either short-circuited or non-moving switches. These measurements prove the potential of these RF-MEMS as being a technology capable of working at higher frequencies as well as capable of being integrated within the antenna, which was the original goal of this research.

Part II

Integrated Focal Plane Antenna Arrays

4

Chapter 4
Micro-Lens Antenna Design

Large[1] format heterodyne arrays and cameras are highly in demand in the submillimeter wave frequency band for ground based and space applications. In recent years, there has been enormous progress in designing terahertz heterodyne receivers in ultra-compact packages which are easy to integrate into arrays. One such idea that has gained ground is to stack multiple layers of silicon micromachined parts in a receiver package [60] as in Figure 4.1. Such an assembly allows integration of submillimeter-wave mixers and frequency multipliers with MIC amplifiers on the same wafer stack. Figure 4.1 shows the scheme of the proposed integration. The key technology that is needed for this silicon array integration to work is the antenna array to couple the RF signal to the detectors. Moreover, the antenna array technology should be consistent with silicon micro-fabrication to have seamless integration of all the front-end elements.

In the submillimeter-wave band, directive antennas are mostly achieved with horns or

[1]The following sections contain portions, sometimes verbatim, of the publication [JA1] of the author.

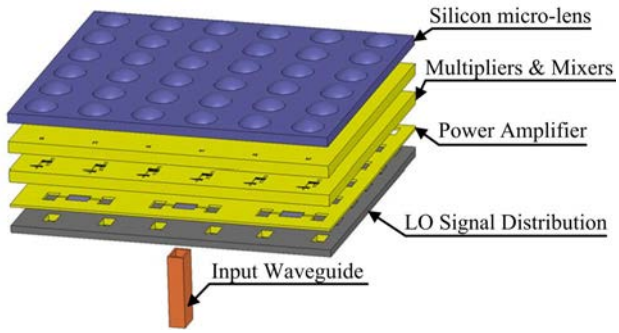

Figure 4.1: Scheme of the wafer-level integration for a multi-element compact receiver

lenses. As it has been explained in the introductory chapter, horns arrays can be fabricated by stacking layers of etched holes in silicon to form platelet horns. This technique has been successfully demonstrated in relatively low frequencies [61], but the higher the frequency, the higher the difficulty in achieving the required tolerances for stacking the layers. At very high frequencies, lenses are usually preferred, as they can be fabricated with silicon micro-machining [62].

A micro-lens antenna compatible with silicon micro-machining techniques and allowing a wafer level integration for array manufacturing has been proposed in this thesis. This section presents the detailed design guidelines and electromagnetic modeling of this antenna.

4.1 Introduction

Submillimeter-wave integrated lens antennas have been extensively studied by Rebeiz group [43, 63] and they basically consist of a hemispherical lens, a dielectric slab and a feed antenna that follows the active receptor circuitry. These antennas are commonly used for imaging applications because of their good coupling to an optical system, i.e how good the antenna is coupled to a Gaussian beam (Gaussicity).

In general, these lens antennas have an ellipsoidal shape as in Figure 4.2a. The antenna feed is placed at the second focus (F_2) of the ellipse with an eccentricity $e = 1/\sqrt{\epsilon_r}$ in order to achieve maximum directivity. The rays that emerge from this point in the direction above the critical angle are focused parallel to the broadside direction obtaining a perfect collimated beam that radiates outside the lens (in Figure 4.2a: the rays that hit the border of the lens below the dashed line are refracted in different directions while the rays that hit above the dashed line are focused broadside). In order to simplify the fabrication of such lens, the most common solution is to use a half hemisphere on top of a wafer of thickness $L/R = 1/\sqrt{\epsilon_r}$ (the thickness of the wafer is defined as an extension height L and usually is given as a function of the radius of the hemisphere), see Figure 4.2b. Note that this approximation is only valid for high dielectric materials.

The reflections that occur at the boundary between the dielectric and air are a significant problem in this type of antennas. Even with the use of a matching layer, there

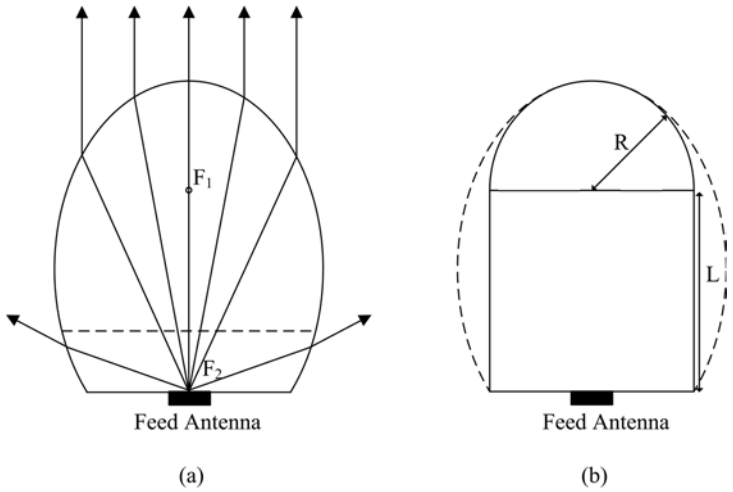

Figure 4.2: (a) Ray tracing of an elliptical lens feed by an antenna placed in the second focus F_2. (b) Synthesis of an elliptical lens from a hyperhemispherical lens.

is a certain point besides the critical angle (around 60 deg) where all the power is reflected back inside the lens. In order to minimize these reflections, a feed antenna that illuminates only the upper part of the lens (not the side) is needed, achieving a directive pattern that focuses the radiation above this critical angle.

In order to design the lens to obtain a good performance in terms of Gaussian coupling and radiation efficiencies, a full characterization of the extended hemisphere lens a function of the extension length needs to be performed for the particular feed antenna illumination used. The optimum extension length depends on the diameter of the lens, on the frequency and on the feed antenna illumination [43]. In general, the larger the diameter, the higher is the extension height. However, for a fix diameter, the optimum efficiency of the antenna is achieved for a certain extension height. This variation is associated to the fact that the extended hemispherical lens is not quite an ellipse and therefore there is a phase error for the hemispherical lens.

Moreover, if the actual phase center of the antenna is not placed in the antenna aperture plane, the optimum extension height L/R can significantly differ from the geometrical one. Figure 4.3 shows the taper efficiency as a function of the extension length L/R. The taper efficiency or utilization factor is defined as $\eta_{ta} = \left(\frac{\lambda}{\pi D}\right)^2 \frac{U(\theta,\phi)|_{max}}{\int_0^{2\pi}\int_0^{\pi} U(\theta,\phi)\sin\theta d\theta d\phi}$, where D is the diameter of the aperture of the lens antenna and $U(\theta,\phi)$ is the radiation pattern of the antenna. A high taper efficiency is obtained due to the use of a high directive antenna feed that illuminates the aperture. Note that in this case the antenna feed phase center is displaced from the antenna aperture plane. Therefore, it is convenient to design the lens in accordance with the illumination of the feed antenna.

The use of matching layers in lenses is recommended to reduce the reflections due to the use of high dielectric substrates. A matching layer is a dielectric layer of thickness $\lambda_m/4$ (being $\lambda_m = \lambda_{diel}/\sqrt{\epsilon_{diel}}$ and ϵ_{diel} and λ_{diel} the permittivity and the wavelength of the lens dielectric) placed on top of the curved surface of the lens. These reflections can

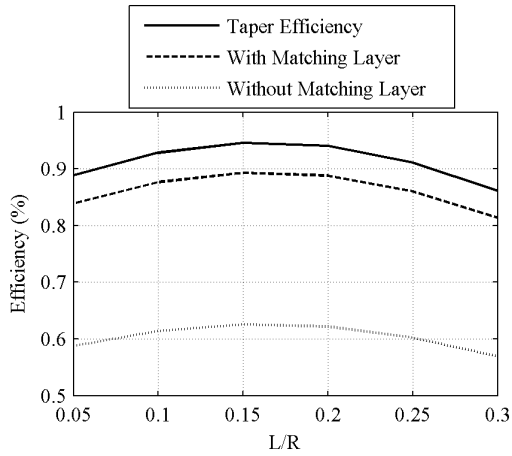

Figure 4.3: Taper efficiency of a micro-lens illuminated with a leaky wave feed as a function of the extension height for a lens aperture of $5mm$ at 550 GHz.

impact on the performance of the antenna, causing a large power loss, as it is shown in Figure 4.3. It can be observed that by using a matching layer a reduction of 30% in the power loss can be achieved.

4.2 Antenna Geometry

In this chapter a lens antenna that can be fabricated and with the same techniques and therefore integrated with other front-end MIC detector elements is presented. Moreover, it can provide directive radiation patterns in order to illuminate efficiently an optical system. The geometry of the lens antenna is shown in Figure 4.4: shallow lens illuminated by a leaky wave waveguide feeds.

The leaky wave waveguide feed, first time proposed in [46], consists of a square waveguide, a ground plane with a double slot aperture (iris) and a resonant air cavity. The waveguide is a square waveguide excited with the TE_{10} mode. The waveguide is used to couple the radiation into the Schottky mixers. The air cavity of thickness $\lambda_0/2$ creates a directive field inside the silicon by increasing the effective area of the waveguide feed because of the excitation of a couple of TE/TM leaky wave modes as described in [64]. The double arc slot iris geometry is used for two purposes: to match the antenna impedance to the TE_{10} waveguide mode and to suppress the undesired TM_0 leaky wave mode that can propagate inside the air cavity.

A lens at the top of the waveguide feed is used to radiate a directive highly Gaussian pattern into free space for an efficient excitation of an optical system. The lens is shallow in order to facilitate its fabrication with silicon micro-fabrication and moreover it simplifies the fabrication of the matching layer. The shallow lens corresponds to the top part of an extended hemispherical lens. In order to generate a well directive pattern with high aperture efficiency, the shallow lens has to be placed at the right distance from the

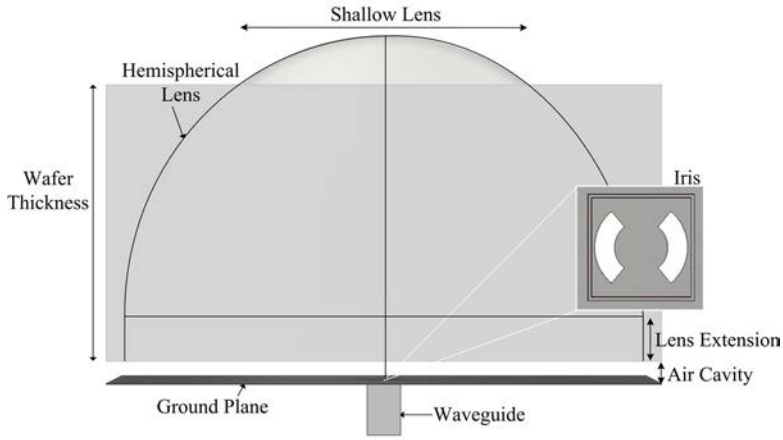

Figure 4.4: Sketch of the silicon micro-lens antenna geometry.

air cavity. This corresponds to displacing the center of the hemispherical lens by an extension height. The waveguide feed will illuminate this shallow lens with a certain field edge taper defined by edge angle. The lens geometrical parameters can be optimized and will be described in the following section to achieve high efficiencies.

4.3 Micro-Lens Antenna Design Guidelines

In this section guidelines employed for the design of the antenna explained before will be discussed. The design can be divided in two processes: the design of the antenna feed and the design of the extended hemispherical lens. Specific examples will be provided of antenna that could be used in an optical system described in [15]. Such system was characterized by an f-number of 2 implying a lens diameter of diameter approximately 2.5 mm at 550 GHz.

4.3.1 Antenna Feed Geometry

The antenna feed consists of a square waveguide, a double slot iris, and a resonant air cavity [64,65] as it is shown in Figure 4.5. The feed is a square waveguide propagating the dominant TE_{10} mode. This waveguide is loaded with a double slot iris (see Figure 4.5b) which is designed to match the antenna impedance to the mode TE_{10} of the waveguide and to suppress the undesired TM_0 mode that alters the radiation pattern at large angles that can propagate in the cavity [64]. Between the waveguide and the dielectric of permittivity ϵ_{rd} there is a cavity of dimension h and dielectric constant ϵ_{rc}. This cavity acts as a partially guiding structure of TE/TM leaky wave modes. These modes are excited when $\epsilon_{rc} < \epsilon_{rd}$ and $h \approx \lambda_0/2\sqrt{\epsilon_{rc}}$ and radiate towards the broadside of the structure.

The dimensions of the double slot have been optimized in order to obtain a reflection coefficient around $-15dB$ in the frequency band of 15%. The reflection coefficient is obtained by the simulation of the waveguide with the iris and an infinite silicon medium

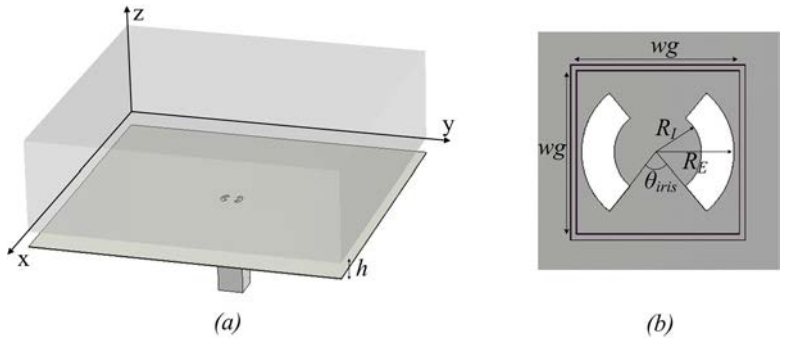

Figure 4.5: (a) 3D view of the antenna feed and (b) top view of the double-slot iris.

on top using MW CST [66]. Figure 4.6a shows the input reflection coefficient of an antenna feed designed to work at 550 GHz. The dimensions of its iris are shown in Figure 4.6b.

The antenna illuminates the lens with the leaky wave waveguide feed. In Figure 4.6c the radiated field by the antenna feed along the silicon medium is shown. As it can be observed, only the upper lens surface is illuminated.

The modelling of the micro-lens is performed using a Physical Optics (PO) method. The PO is a ray tracing technique that calculates the far-field patterns of the complete lens antenna. This PO technique uses as an input the primary fields, which are the fields radiated by the antenna feed within the silicon medium, on the lens inner surface. These primary fields are used to compute the distribution of the electric and magnetic fields across the spherical surface of the extended hemispherical lenses. The Fresnel transmission coefficients are used at the boundary to calculate the reflected and radiated field values. After the fields have been multiplied by the appropriate transmission coefficients, the equivalent and magnetic current densities are determined just outside the spherical surface. From this currents, the far fields are then determined by integrating over the lens surface. Further information about the primary and secondary field calculations employed is presented in Annex 2.

Because the feed antenna is very directive, the lens surface can be in the near field of the antenna; this fact has to be taken into account in the PO calculation in order to obtain accurate results. For the cases considered in this thesis, the lens is not placed in the reactive near-field region of the feed, but in the radiative region, and therefore the PO can still be performed. The calculation uses the incident field decomposed on plane waves coming from the antenna feed but with a different amplitude and phase, i.e. the one given by the near field calculated over the lens surface. The main difference of the calculation of the primary fields through the near-field or far-field is that broader radiation patterns are obtained in the case of the near-field compared to the far-field. Thus, the dimensions of the lens are larger for feeds in the near-field than for feeds in the far-field.

The primary fields has been calculated by simulating the antenna feed structure with MW CST. The computation of the near field is performed by integrating the field obtained in CST over the xy grid after the cavity using the free space Green's function, as explained in [65]. Figure 4.7a and b shows a comparison of the simulated primary field calculated

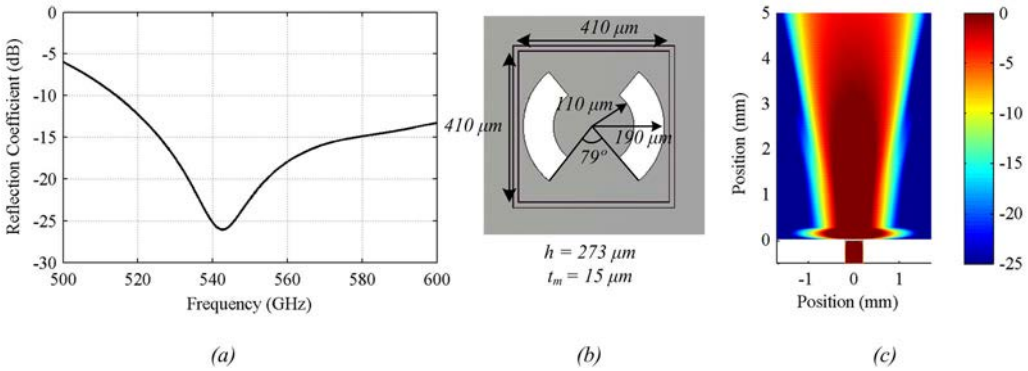

Figure 4.6: (a) Antenna input feed reflection coefficient of a waveguide loaded with a double arc iris in the presence of an air cavity ($h = 273\mu m$) and an infinite silicon medium. (b) Antenna feed dimensions.(c) Radiated field of the antenna feed along the silicon medium.

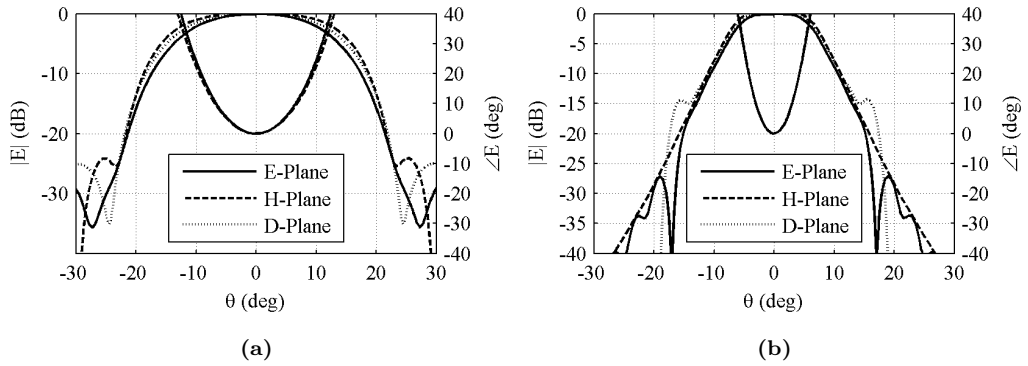

Figure 4.7: Normalized amplitude and phase of the electric near-field (at 4.5λ) (a) and far-field (b) inside an infinite silicon medium.

in the near-field or in the far-field of the antenna. It can be observed that the near-field patterns are broader than the far-field patterns. Note also that from the phase of the electric fields of Figure 4.7, it can be observed that the phase center is not in the plane of the waveguide aperture. The phase center of this antenna is below the waveguide aperture, and this displacement implies that the extension height of the lens needs to compensate this phase difference, as it will be shown in the next section.

This feed antenna has been selected because it is easier to fabricate in array using silicon micromachining processes and it presents lower losses, i.e reflection losses, ohmic losses compared to other kind of directive antennas. This feed presents a limitation in its frequency behavior due to the leaky wave cavity which depends on the dielectric material of the cavity. Because, of the use of an air cavity, a bandwidth of 15% can be achieved, and the fields presents a low frequency variation in this frequency range.

The performance of this antenna feed structure is affected by the losses associated to the finiteness of the structure, i.e spillover in the air cavity and the losses associated to

the dielectric material used for the infinite medium. In the next section, these losses are introduced and calculated.

4.3.1.1 Leaky Wave Spillover Losses

There is some residual power radiated towards the air at the edge of the cavity that will depend on the diameter of the lens. This residual power associated to the leaky wave air cavity is computed assuming that a cylindrical radiating wave is created inside the air cavity by a couple of leaky wave modes. The loss has been computed assuming a rotationally symmetric cylindrical leaky wave:

$$E = \frac{e^{j\beta\rho}e^{\alpha\rho}}{\sqrt{\rho}} \tag{4.1}$$

The attenuation constant obtained from [65] is $-0.3k_0$ at $550GHz$. Therefore, the percentage of power that arrives to the lens edge is:

$$L_{leaky}(\%) = \frac{\int_0^{D/2} \frac{e^{2\alpha\rho}}{\rho}\rho d\rho d\phi}{\int_0^{\infty} \frac{e^{2\alpha\rho}}{\rho}\rho d\rho d\phi} = \frac{\int_0^{D/2} \frac{e^{2\alpha\rho}}{\rho}\rho d\rho}{\int_0^{\infty} \frac{e^{2\alpha\rho}}{\rho}\rho d\rho} = 1 - e^{\alpha D} \tag{4.2}$$

Losses in the air cavity associated to the leaky wave modes have been calculated to be less than 1% for lens diameters larger than 4λ and therefore, they have been neglected in the study. This result has been corroborated with simulations in CST by integrating the field radiated within the leaky wave cavity and normalizing it with the input power.

4.3.1.2 Dielectric losses

The losses in the dielectric have been calculated with the equation:

$$L_{diel}(dB) = 20log(\epsilon^{-\alpha l}) \tag{4.3}$$

being l the thickness of the dielectric and α:

$$\alpha = \omega\sqrt{\mu\epsilon}\sqrt{\frac{1}{2}\left[\sqrt{1+(\tan\delta)^2}-1\right]} \tag{4.4}$$

and

$$\tan\delta = \frac{\sigma}{\omega\epsilon} = \frac{1}{\omega\epsilon_0\epsilon_r\rho} \tag{4.5}$$

Considering that the silicon used in this study is high resistivity silicon with a permitivity of $\epsilon_r = 11.67$ and a resistivity of $\rho = 10k\,\Omega\cdot cm$. The tangent loss obtained is $\tan\delta = 2.8\cdot 10^{-5}$, $\alpha = 0.5513$ and therefore the losses are calculated to be $L_{diel}(dB) = -4.79dB/m$. For a wafer with a thickness of $21\lambda = 11.5mm$ the total losses due to the dielectric would be $0.055dB$. Therefore, these loss has been neglected in this study.

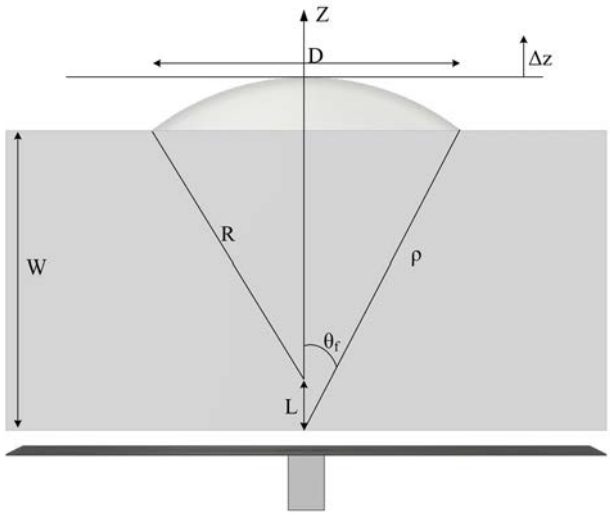

Figure 4.8: Sketch of the silicon micro-lens antenna geometry.

4.3.1.3 Conductor Losses

Losses in the conductor ground plane have been calculated using the expression

$$P_c = \frac{1}{2}\sqrt{\frac{\pi\mu f}{\sigma}}\int_S |H|^2 dS \tag{4.6}$$

being σ the conductivity of the conductor material, H is the magnetic field intensity in A/m, f is the frequency and μ is the permeability value of the conductor. In this case of a $550GHz$, losses have been calculated to be 1% of the power transmitted to the antenna. Therefore, they have been neglected in the study.

4.3.2 Micro-Lens Design

In this section, the detailed design guidelines of the micro-lens geometry are presented. Several parameters have to be optimized in order to maximize the antenna directivity for a certain diameter and field edge taper. The parameters depend on the actual lens diameter because the feed illumination varies if the micro-lens is in the near or far field of the primary feed. Therefore general design curves with the optimized parameters that provide maximum aperture efficiency are given as a function of the lens diameter D.

The lens geometry is shown in Figure 4.8. A silicon wafer of thickness W lies on top of the feed. This wafer includes a sector of a hemispherical lens, referred later in the paper as micro-lens. This micro-lens is defined by the edge angle θ_f, radius R of the hemisphere, height of the lens H, and the diameter D. In order to obtain the maximum possible directivity, these parameters need to be optimized. Note that the center of the lens sphere does not coincide with the primary feed and it is subject to the optimization similar to standard extended hemispherical lenses [43].

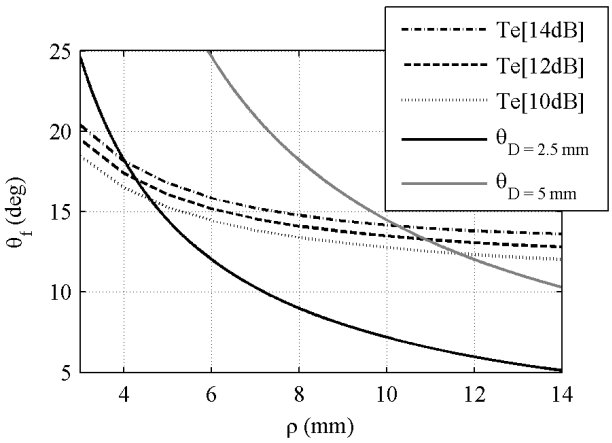

Figure 4.9: Taper values θ_f as a function of the distance ρ at a function of the distance ρ at 550 GHz.

The antenna is designed in order to maximize its aperture efficiency at the central frequency of the band, which corresponds to the frequency in which the air cavity is equal to $\lambda_0/2$. The ultimate goal of this work is to fabricate a focal plane lens array including a standard quarter wavelength matching layer of parylene and therefore eliminating the impact of the multiple reflections [67, 68]. For ordinary lenses arrays, when the whole hemisphere of the lens is illuminated, the fabrication of the matching layer is quite complex. But in this case, the use of shallow lenses substantially simplifies the fabrication of this layer. Note that the geometry considered here is a relatively narrow band antenna, and therefore such matching layer will have a good behavior over the whole frequency band.

The first parameter to optimize is the edge angle θ_f. This angle is associated with the field level at the edge of the lens aperture in the same way that is done for reflector antennas (i.e. $Te[12dB]$ corresponds to a field level of $-12dB$ at the edge of the lens with respect to the field level at the center). This taper angle provides the trade-off between the spillover loss and the taper efficiency.

The spillover of the lens is defined as the amount of power transmitted by the antenna feed that is not caught inside the aperture of the lens. The lens field taper has been the subject of in depth studies such as in [67] and it can be calculated as:

$$\eta_{S_L} == \frac{\int_0^{2\pi}\int_0^{\theta_f} |E_f(\theta,\phi)|^2 \sin\theta \, d\theta \, d\phi}{\int_0^{2\pi}\int_0^{\pi/2} |E_f(\theta,\phi)|^2 \sin\theta \, d\theta \, d\phi} \tag{4.7}$$

being $E_f(\theta,\phi)$ the field radiated by the antenna feed.

The taper angle associated to a certain field level will differ if the feed is in the near or far field, and this will affect the associated lens diameter. For example, Figure 4.9 shows the angle as a function of the distance ρ for different taper values (i.e. 10dB, 12dB and 14dB) for the feed presented above at 550 GHz. The dotted lines have been obtained by

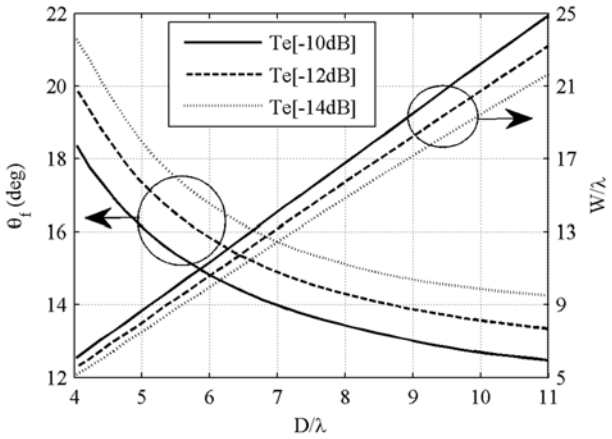

Figure 4.10: The taper angle θ_f (left axis) and the wafer thickness W/λ (right axis) are presented as a function of the normalized lens diameter D/λ for different field tapers.

calculating the primary near field inside the dielectric of the antenna feed field simulated with CST. The solid lines represent the theoretical value of the taper for a fixed aperture (i.e $D = 5mm$ and $D = 2.5mm$ given by $\theta_f = \sin^{-1} D/2\rho$. The intersection between both lines will give the optimal taper θ_f and distance ρ where the lens will be placed. For example, for a lens aperture of 5 mm and a taper of 12 dB at 550 GHz, it is obtained a ρ of 10.8 mm and a taper of 13.4 deg. However, for a lens aperture of 2.5 mm and a taper of 12 dB at 550 GHz, it is obtained a ρ of 4.0 mm and a taper of 18.1 deg. One can appreciate that the taper decreases more rapidly in the near field zone and it gets flatten as it moves to the far field, where the taper will be independent of ρ.

Here we perform the optimization for several field tapers because depending on the application one would like to minimize the spillover, i.e large field taper (e.g. not fully sampled focal plane arrays) or maximize the directivity (e.g. fully sampled focal plane arrays).

The angle for a -10, -12 and -14 dB taper has been obtained by calculating the primary near field inside the dielectric as explained in [65] and averaging the tapers in the main cuts of the antenna. Figure 4.10 presents the edge angle for these three tapers depending on the diameter of the aperture that one would like to design. All the curves are provided as a function of the free space wavelength, λ. It can be observed that the taper angle decreases more rapidly in the near field zone and it gets flatten as it moves to the far field, where the taper angle is independent of the lens aperture. The right axis of the same figure presents the corresponding wafer thickness W, which can be easily calculated as $W = D/2\tan(\theta_f)$.

For each diameter, the surface curvature has to be optimized to maximize the antenna directivity. The lens surface curvature is an extended hemisphere defined with the radius R and the height H as shown in Fig. 4.11.

Figure 4.11 shows a set of lens surfaces associated with a fixed aperture diameter D and wafer thickness W, which is selected by fixing the field taper angle θ_f. The radius

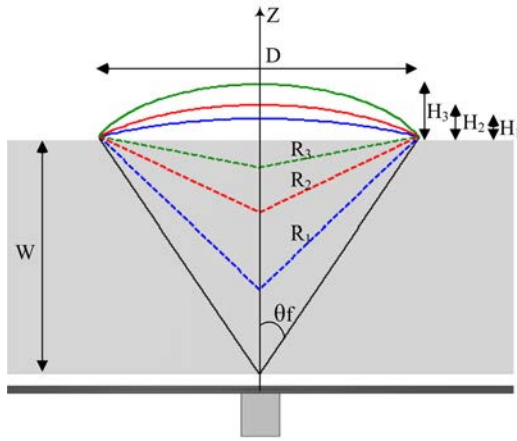

Figure 4.11: Sketch of different micro-lens curvatures as a function of the hemispherical lens radius and center for a fixed taper angle.

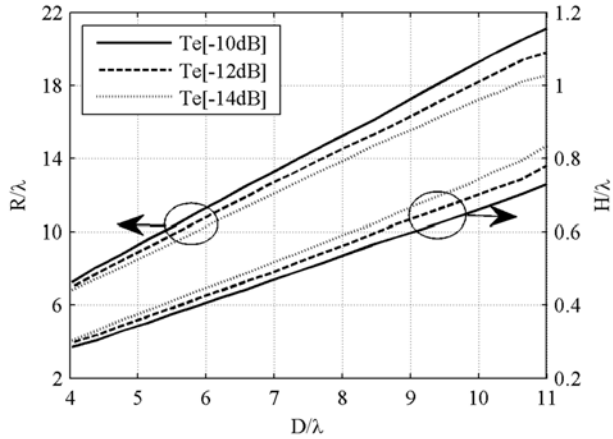

Figure 4.12: Optimum radius R (right axis) and height H (left axis) of the micro-lens as a function of the diameter D for different field tapers.

and height parameters control the actual curvature of the lens, as it is shown in Figure 4.11. The height defines where is the center of the hemisphere defining the lens surface (i.e. $L = W + H - R$). Note that L can be also negative meaning that the center of the hemisphere is under the air cavity.

For planar antennas, the optimum lens surface is known. However, the leaky-wave waveguide feed has a phase center below the waveguide aperture and therefore the optimum lens surface will differ from the standard cases [65]. In order to optimize these lens parameters to maximize the directivity, a set of surfaces obtained varying the height and radius are studied with a PO tool. Because the structure is too big in terms of the wavelength, a full-wave simulator cannot be used to perform this analysis due to the computational time and complexity of the global structure. This PO approach has been

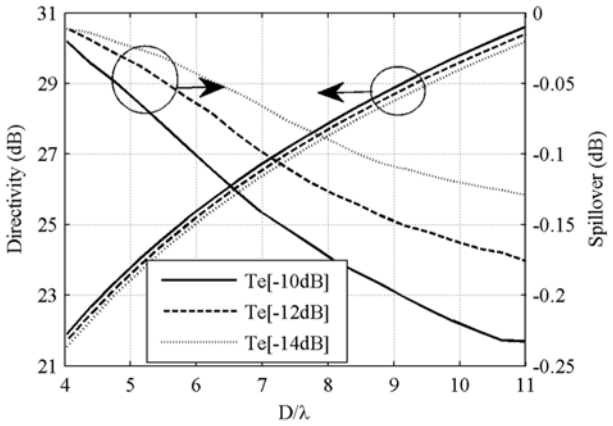

Figure 4.13: Directivity (left axis) and spillover (right axis) as a function of the diameter D of the micro-lens for different field tapers.

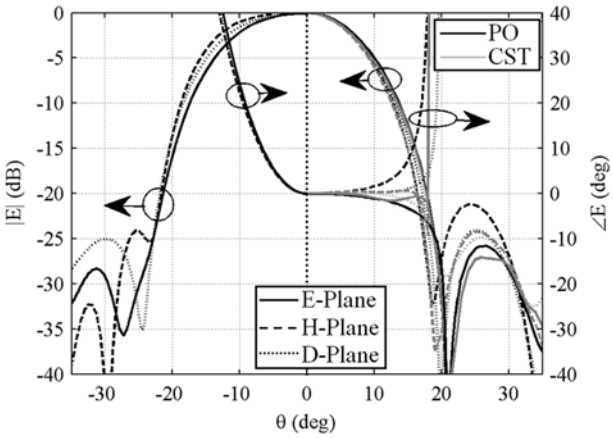

Figure 4.14: (Left) Normalized amplitude and phase of the electric field inside an infinite silicon medium at 4.5λ from the antenna feed. (Right) Normalized amplitude and phase of the electric field obtained with the PO method and full-wave simulation of the lens antenna for a lens diameter of $D = 4.5\lambda$.

validated with full-wave simulations using CST Microwave Software of a lens antenna with a small diameter $D = 4.5\lambda$ as it is shown in Figure 4.14 (Right). The same method was also validated in [65] with full-wave simulations and measurements. The optimization of the lens surface (i.e. the selection of the lens radius R and height H) is done as a function of the aperture dimensions, D, for -10, -12 and -14 dB feed tapers. The optimum parameters resulting in the highest directivity are summarized in Figure 4.12, whereas Figure 4.13 shows the obtained antenna directivity and the spillover loss for all the cases.

A very important parameter to investigate is the Gaussicity because the main application of such lens antennas is to be used as focal plane arrays and the Gaussicity is related to how well the antenna is coupled to an optical system. It is defined as the coupling

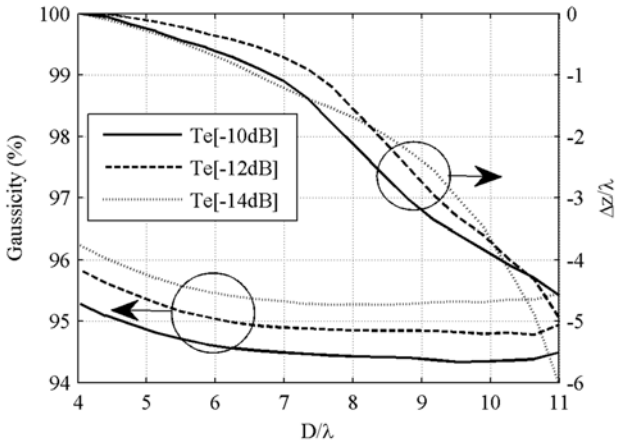

Figure 4.15: Gaussicity (left axis) and phase center correction (right axis) as a function of the diameter D of the micro-lens for different field tapers.

efficiency of an antenna far field patterns to a Gaussian-beam [69]. The coupling efficiency of an antenna to a Gaussian beam is the relationship between the far-field patterns of the antenna and the far-field Gaussian beam expression, defined as:

$$\eta_{Gauss} = |\langle\psi_{ant}|\psi_{Gauss}\rangle|^2 = \frac{\iint(\vec{v}_{co}\cdot F(\theta,\phi))e^{-(\theta/\theta_0)^2}e^{\pm j\pi(\theta/\theta_1)^2}\sin\theta d\theta d\phi}{\iint|F(\theta,\phi))|^2\sin\theta d\theta d\phi\iint e^{-2(\theta/\theta_0)^2}\sin\theta d\theta d\phi} \tag{4.8}$$

Before performing such calculations, the beam waist and the phase center of the lens antenna that maximize the Gaussicity for each case are calculated. Figure 4.14 (Right) shows the far field of the antenna (E-Plane, H-Plane, D-Plane). Note that the cross polarized fields in the three planes fall out of the figure scale. The phase center of the antenna (indicated as Δ_z in Figure 4.8) is shown in Figure 4.15 for all cases. In the same figure, the Gaussicity is also provided. One can appreciate that high values of Gaussicity are obtained for all the diameters.

All in all, the optimization has been performed with parametric study varying a single parameter associated to the lens surface curvature (see Fig.4.11) in order to maximize the efficiency of the lens. The surface curvature is an extended hemispherical lens, which is defined with a radius and an extension height. The optimization was performed varying both the radius and extension height simultaneously for a fixed wafer thickness W and lens diameter D. In particular, the optimization procedure is the following:

- For a certain diameter D, obtain the taper angle of the primary field and the wafer thickness W by calculating the primary field radiated inside an infinite dielectric of silicon using a CST simulation. The field taper varies as a function of the diameter of the lens, depending if the feed antenna is in the far-field or near-field zone.
- Optimize the lens height H and radius R of the micro-lens to maximize the efficiency of the antenna. This optimization is achieved by performing a parametric study and choosing the value that maximizes the efficiency of the antenna. The efficiency of the antenna is obtained through the secondary field calculation using the PO method.

5 Chapter 5 Focal Plane Array Design

5.1 Introduction

Submillimeter-wave technology and in particular, heterodyne techniques have been highlighted as an important imaging capability for ground based and space applications [60,70]. Most heterodyne systems currently used provide sufficient science data in spite of being single pixel. However, recent applications like the imaging radar presented in [15] or space applications would take advantage from having large format of heterodyne arrays by imaging several pixels simultaneously and therefore increase its acquisition time.

A Focal Plane Array (FPA) is an array of antennas placed at the focal plane of an imaging system. In radio astronomy, FPAs are placed at the focus point of a radio telescope. Initially, radio telescopes had one receiver at the focus of the telescope, like in Figure 5.1. Now, the use of FPAs allows multiple pixel scanning, increasing the survey speed by a factor N, being N the number of antennas. Each antenna points to a different part of the field of view.

Figure 5.1: Imaging system composed by one element

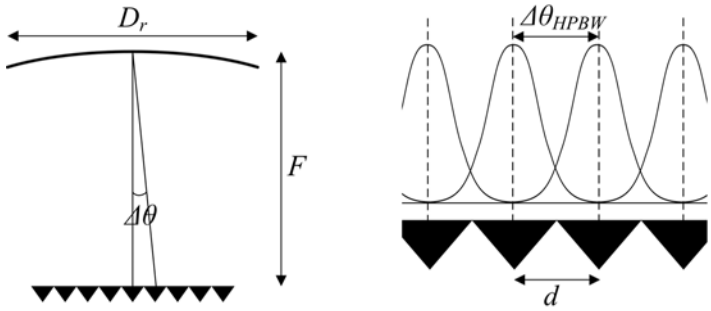

Figure 5.2: A FPA located at the focal plane of a reflector system, generates multiple independent beams.

The resolution of the image is the key parameter in an imaging system. In a FPA, the parameter that is directly related to the resolution is the array spacing d. This parameter and the illumination efficiency of the array determine the characteristics of the FPA and they can be optimized for narrow band systems (for frequency bands of less than 25%).

In this chapter, the development of the design guidelines of a FPA at terahertz frequencies is presented. This design complies with the power budget and fabrication constraints limitations that systems face at THz.

5.2 FPA Illumination

A FPA located at the focal plane of a reflector, generates multiple independent beams as shown in figure 5.2. Three parameters characterize the performance of the FPA within the imaging system: the beam separation $\Delta\theta$, the reflector diameter D_r, and the focal distance F. On one hand, the beam separation can be approximated to the resolution of the imaging system, $\Delta\theta \approx \Delta\theta_{HPBW}$ (see Figure 5.2). On the other hand, the illumination efficiency of the reflector is determined by two parameters:

- The spillover, defined as the power transmitted by the feed antenna that is not caught by the reflector. The spillover efficiency is defined as the ratio of energy incident at the reflector to the total energy emitted by the feed. For a cylindrical symmetry radiation pattern it can be expressed as:

$$\eta_{so} = \frac{\int_0^{2\pi}\int_0^{\theta_0} |f(\theta)|^2 \sin\theta d\theta d\phi}{\int_0^{2\pi}\int_0^{\pi} |f(\theta)|^2 \sin\theta d\theta d\phi} \tag{5.1}$$

  where $f(\theta)$ is the radiation pattern of the antenna and θ_0 is the angle defined by the feed and the reflector (see Figure 5.3):

$$\tan(\theta_0/2) = \frac{D_r}{4F} \tag{5.2}$$

  The spillover efficiency improves with the diameter of the feed and at the same time this diameter is limited by the sampling condition.

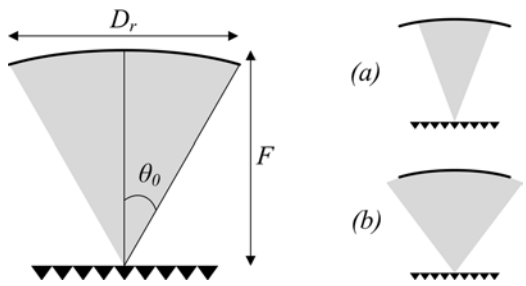

Figure 5.3: The spill over the part of the feed antenna radiation that misses the reflector.(Left) Efficiently illuminated reflector. (Right) Reflector illuminated inefficiently: (a) Good spill over bad taper efficiency, (b) Bad spill over and good taper efficiency

- The taper efficiency is the loss associated with the aperture taper and expresses the uniformity of the field distribution on the aperture. It can be expressed as:

$$\eta_t = 32\left(\frac{F}{D_r}\right)^2 \frac{\left|\int_0^{2\pi}\int_0^{\theta_0} f(\theta)\tan(\theta/2)d\theta d\phi\right|^2}{\int_0^{2\pi}\int_0^{\theta_0}|f(\theta)|^2\sin\theta d\theta d\phi} \tag{5.3}$$

The aperture efficiency will be defined as combination of the spillover and taper efficiency $\eta_{ap} = \eta_s\eta_t$.

Let us now consider what the implications in terms of reflector illumination efficiency and sampling criteria are, when a circular aperture with a certain field distribution (i.e the aperture of a horn or a lens) is used to illuminate a reflector of certain f-number.

5.2.1 Uniform Illumination

Consider that the reflector is illuminated with a circular aperture with uniform illumination. The normalized radiation pattern of an aperture A can be expressed as the Fourier transform of the aperture field:

$$f(\theta,\phi) = \frac{1}{A}\int_A e^{j\mathbf{k}\cdot\mathbf{r}'}dS' \tag{5.4}$$

This is valid for very directive antennas, i.e big apertures in terms of the wavelength.

Considering a circular aperture of diameter D and cylindrical symmetry ($f(\theta,\phi)$ is independent of ϕ) illuminated with a linear polarized wave $\vec{E} = E_x\hat{x}$ (see Figure 5.4). For computing the integral, we may set $\phi = 0$. Having that $\mathbf{k}\cdot\mathbf{r}' = k_x x' = k\rho'\sin\theta\cos\phi'$ and $dS' = \rho' d\rho' d\phi'$

$$f(\theta) = \frac{1}{\pi r_a^2}\int_0^{D/2}\int_0^{2\pi} e^{jk\rho'\,\sin\theta\,\cos\phi'}\rho'\,d\rho'\,d\phi' \tag{5.5}$$

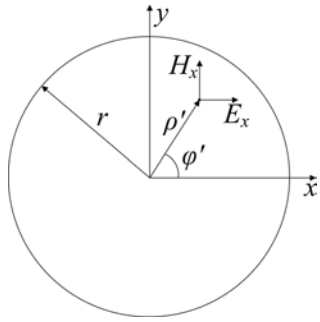

Figure 5.4: Circular aperture.

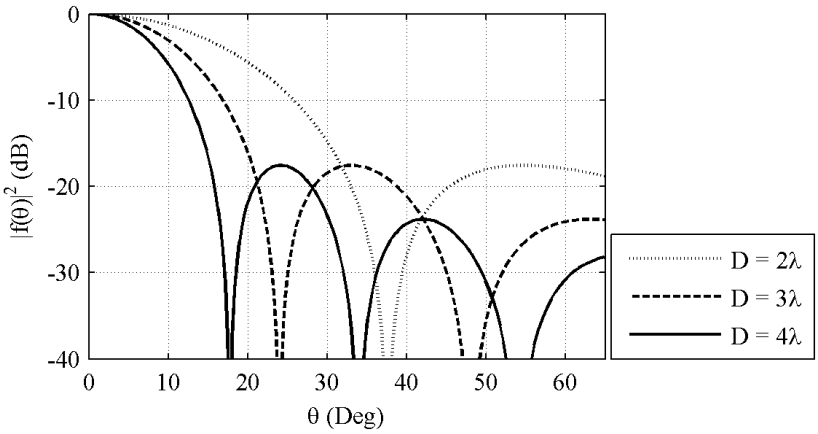

Figure 5.5: Radiation pattern of a circular aperture with uniform illumination for different aperture diameters.

Using the Bessel functions $J_0(x)$and $J_1(x)$,

$$J_0(x) = \frac{1}{2\pi}\int_0^{2\pi} e^{jxcos\phi}d\phi \quad and \quad \frac{J_1(x)}{x} = \int_0^1 J_0(xr)rdr \tag{5.6}$$

the integrations can be solved giving a normalized radiation pattern field of:

$$f(\theta) = 2\frac{J_1(k\,D/2\,\sin\theta)}{k\,D/2\,\sin\theta} \tag{5.7}$$

Figure 5.5 shows the radiation pattern of a circular aperture with uniform illumination for different aperture diameters D. The directivity of the antenna increases with the diameter of the aperture and therefore, the spill over efficiency improves(see Figure 5.6).

As it has previously introduced, for an imaging system that fully samples the field of view, the beam separation should be the same as the resolution. considering that the $\Delta\theta_{HPBW}$ can be approximated as $\Delta\theta_{HPBW} \approx \lambda/D_r$, the beam separation is defined by the diameter of the reflector:

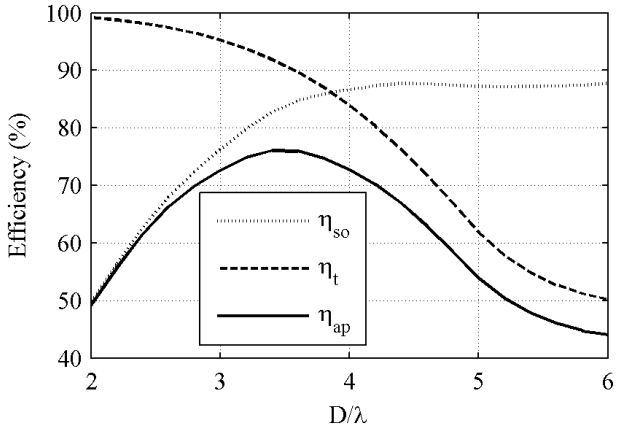

Figure 5.6: (Left axis) Spillover and (right axis) taper at θ_0 of the radiation pattern of a circular aperture with uniform illumination, of a a reflector of $F/D = 2$.

$$\Delta\theta \approx \lambda/D_r \tag{5.8}$$

Moreover, the beam separation depends on the array separation and the focal distance F:

$$\tan(\Delta\theta) = \frac{d}{F} \rightarrow \Delta\theta \approx \frac{d}{F} \tag{5.9}$$

Using the small angle approximation for $\Delta\theta$. With these two connections, the separation between the antenna feed can be defined as:

$$d \cong \Delta\theta\, F = \lambda \frac{F}{D_r} \tag{5.10}$$

which is usually referred as single sampling.

Lets now consider what this sampling implies in terms of illumination efficiency. Figure 5.6 presents the spillover of a reflector of $F/D_r = 2$ illuminated by a circular aperture with uniform illumination as function of the diameter of the feed. As it is shown, the spillover efficiency improves with the diameter of the feed. However, in a FPA, the sampling condition d limits the size of this diameter as it is shown in equation 5.10. Note that this efficiency problem is independent of the F/D ratio because the feed aperture is in any case limited by the sampling condition. In this example, the separation between antennas is $d = \lambda\frac{F}{D_r} = 2\lambda$, and consequently the maximum radius of the aperture has to be $D \leq 2\lambda$, giving a spillover higher than -3 dB.

One way to increase the beam separation and to cover the field of view would be by using the fast rotation of a small mirror, a technique called jiggling [71]. In this case the cross over to adjacent beams would be two times the half power beamwidth as it is shown in Figure 5.7. This technique allows a double sampling condition, implying that the distance between elements can be doubled:

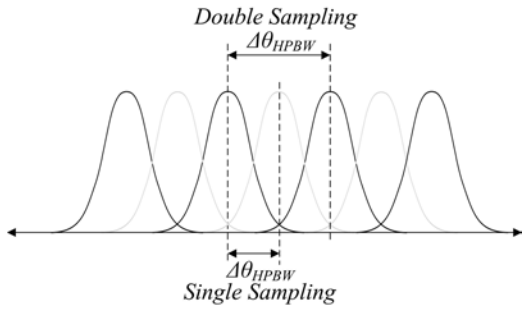

Figure 5.7: In double sampling, the cross over to adjacent beams would be two times de half power beamwidth.

$$d \cong 2\Delta\theta\, F = 2\lambda \frac{F}{D_r} \tag{5.11}$$

In the example of Figure 5.6, when using double sampling, the separation between the antennas is $d = 4\lambda$ and as a result the diameter of the aperture should be less than $D \leq 4\lambda$, giving more margin to obtain a significantly lower spillover (around -0.6 dB).

The taper efficiency, in the case of double sampling is limited by the high sidelobes associated to the distribution given in equation 5.7 (see the radiation patterns in Figure 5.5) as it can be observed in its performance in Figure 5.6. In order to improve this efficiency, a tapered field distribution in the feed aperture will be used. In the following section a Gaussian field distribution with a -10, -12, 14 dB is considered. The radiation pattern of a Gaussian illuminated aperture has lower sidelobes than the uniform illuminated aperture.

5.2.2 Gaussian Illumination

Consider now the synthesis of the radiation pattern for a circular aperture with a tapered Gaussian illumination. A Gaussian intensity distribution with taper Te_{dB} in the aperture plane has a field distribution of:

$$g(\mathbf{r}) = \begin{cases} \frac{1}{\sqrt{2\pi}\sigma} e^{-\mathbf{r}^2/4\sigma^2} & |\mathbf{r}| < r_a \\ 0 & |\mathbf{r}| > r_a \end{cases} \tag{5.12}$$

where σ is the standard deviation of a standard aperture, i.e $\sigma^2 = -r_a^2/lnC$, C is the feed taper which is defined as the amplitude of the feed radiation pattern at the aperture edge relative to the maximum value (in dB, $Te_{dB} = 20logC$) and r_a is the radius of the aperture $r_a = D/2$.

The far field is the Fourier transform of the aperture plane distribution:

$$f(\theta,\phi) = \mathcal{F}\{g(\mathbf{r})\} = \mathcal{F}\left\{\frac{1}{\sqrt{2\pi}\sigma} e^{-\mathbf{r}^2/4\sigma^2} circ(\mathbf{r}/r_a)\right\} = \mathcal{F}\left\{\frac{1}{\sqrt{2\pi}\sigma} e^{-\mathbf{r}^2/4\sigma^2}\right\} * \mathcal{F}\{circ(\mathbf{r}/r_a)\} \tag{5.13}$$

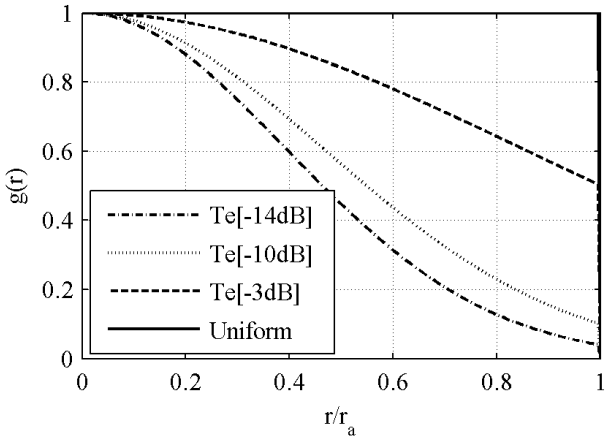

Figure 5.8: Aperture illumination with a gaussian distribution for different tapers.

Because the circular aperture has circular symmetry, and using the following integral representation of the Bessel function:

$$J_0(x) = \frac{1}{2\pi} \int_0^{2\pi} e^{jx cos\phi'} d\phi' \tag{5.14}$$

it can be written:

$$\begin{aligned} f(\theta) &= \left[\frac{1}{\pi r_a^2} \int_0^\infty \int_0^{2\pi} \frac{1}{\sqrt{2\pi}\sigma} e^{-\rho'^2/4\sigma^2} e^{jk\rho' \sin\theta \cos\phi'} \rho' \, d\rho' \, d\phi' \right] * \left[\frac{J_1(k\, r_a \, \sin\theta)}{k\, r_a \, \sin\theta} \right] = \\ &= \left[\frac{1}{2\pi^2 r_a^2} \frac{1}{\sqrt{2\pi}\sigma} \int_0^\infty e^{-\rho'^2/4\sigma^2} J_0(k\, \rho' \, \sin\theta) \rho' \, d\rho' \right] * \left[\frac{J_1(k\, r_a \, \sin\theta)}{k\, r_a \, \sin\theta} \right] \end{aligned} \tag{5.15}$$

Using the Hankel transform:

$$H_0(u) = \int_0^\infty h(\rho') J_0(u\rho') r \, d\rho' \tag{5.16}$$

The radiation pattern can be expressed as:

$$f(\theta) = \left[\frac{\sigma^2}{8\pi^2 r_a^2 \sqrt{2\pi}\sigma} e^{-\frac{\sigma^2 k^2 \sin^2\theta}{16}} \right] * \left[\frac{J_1(k\, r_a \, \sin\theta)}{k\, r_a \, \sin\theta} \right] \tag{5.17}$$

Figure 5.9 shows radiation patterns of a circular aperture with a tapered Te_{dB} Gaussian illumination. Note that the sidelobes with a Gaussian tapered illumination decrease considerably as the taper increases. Consequently, an improvement of the overall illumination efficiency is expected as it can be observed in Figure 5.10. Figure 5.10 shows the spillover, taper and aperture efficiency for a tapered $Te[12\ dB]$ Gaussian illumination in

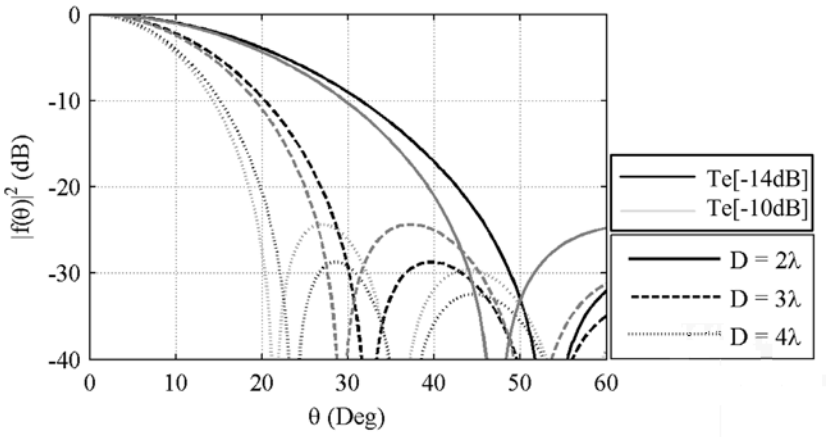

Figure 5.9: Radiation patterns of a circular aperture with different radius r_a with a gaussian illumination with tapers $Te[-10dB]$ and $Te[-14dB]$.

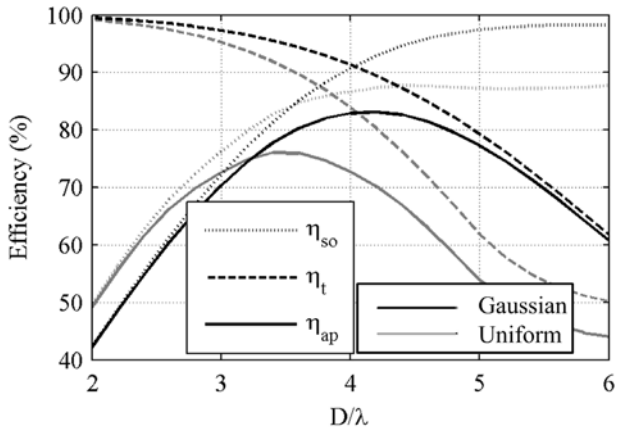

Figure 5.10: FPA efficiency of a reflector of $F/D_r = 2$ fed by a 12 dB tapered Gaussian illumination aperture.

comparison with a uniform illumination. Notice that an increase of 10% in the beamwidth for the -12 dB taper feed aperture can be obtained with the Gaussian feed illumination compared to the uniform distribution.

The resolution achieved in a Gaussian field distribution which also depends on the beamwidth of the imaging system is, in this case, defined as follows:

$$\Delta\theta_{HPBW} = (1.02 + 0.0135 Te^r_{dB}) \frac{\lambda}{D_r} \tag{5.18}$$

where Te^r_{dB} is the taper of the reflector in dB and D_r is the diameter of the aperture of the reflector. Therefore, the separation between the antenna feeds for single sampling will be:

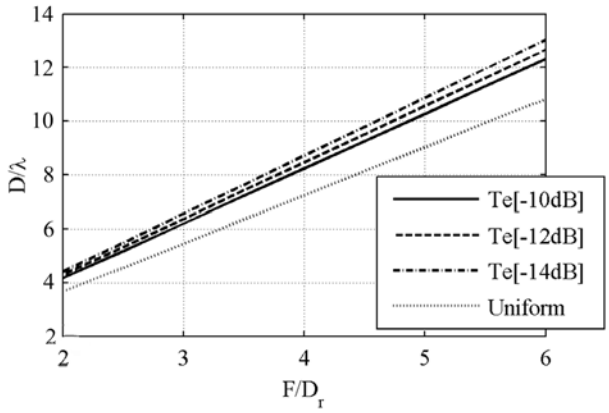

Figure 5.11: Aperture diameter D of the circular aperture with a tapered Gaussian and a uniform field distribution illuminating a reflector with a taper of $Te^r[-11dB]$, as a function of F/D_r.

$$d = (1.02 + 0.0135Te^r_{dB})\frac{\lambda F}{D_r} \tag{5.19}$$

and for double sampling:

$$d = 2(1.02 + 0.0135Te^r_{dB})\frac{\lambda F}{D_r} \tag{5.20}$$

Therefore, if a taper of $Te^r[-11dB]$ in the reflector is considered, the distance between antenna feeds (equivalent to the maximum aperture size) will be $d = 1.17\lambda\frac{F}{D_r}$ for single sampling and $d = 2.31\lambda\frac{F}{D_r}$ for double sampling. With this taper, the optimum diameter of the aperture has been studied in order to efficiently illuminate the reflector for the different field distributions discussed. Figure 5.11 and Figure 5.12 shows this aperture diameter and its the corresponding aperture efficiency of these feed illuminations.

Comparing the aperture's diameter to the distance between feeds d, a ratio of occupation of the cell can be obtained by:

$$Occupation(\%) = \frac{D}{d} \tag{5.21}$$

Figure 5.13 shows the occupation of the cell for each aperture taper as a function of the F/D_r of the reflector. It has been calculated for a taper of -11 dB at the reflector. Notice that for a Gaussian field distribution, a radius radius $D > 4/\lambda$ grants a spillover of less than 0.5 dB. Moreover, an increase of 5% in the beamwidth for the -12 dB taper feed aperture and double spacing conditions can be obtained with a Gaussian feed illumination compared to a uniform distribution. This means that the array spacing can be increased by a 5% giving some room for the fabrication of the array elements.

Different things can be deduced from this analysis:

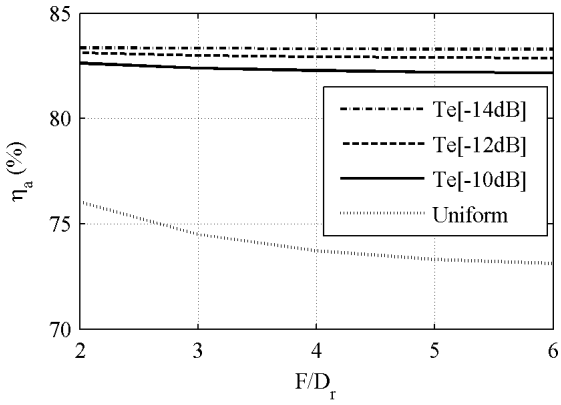

Figure 5.12: Maximum aperture efficiency achieved with a circular aperture with a tapered Gaussian and a uniform field distribution illuminating a reflector with a taper of $Te^r[-11dB]$, as a function of F/D_r.

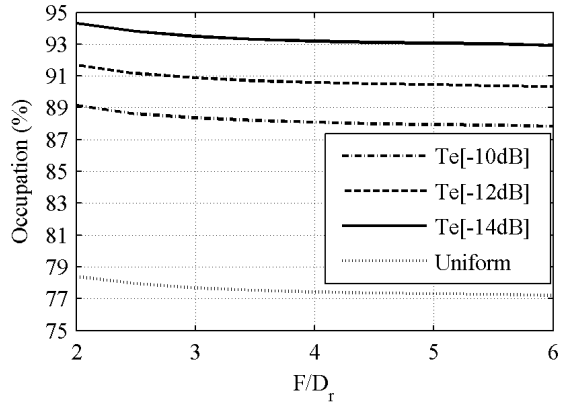

Figure 5.13: Occupation of the cell for a circular aperture with a tapered Gaussian and a uniform illumination illuminating a reflector with a taper of $Te^r[-11dB]$, as a function of F/D_r.

- The efficiency for a single sampling condition is worse in terms of spill over. Double sampling condition is essential to design a FPA with a high aperture efficiency.
- Higher aperture efficiencies can be obtained with tapered aperture field distributions (radiation patterns have lower sidelobes). By increasing the taper of the aperture the efficiency increases however, the occupation of the cell also increases. A fabrication limitation can restrict the cell occupation of the cell, and consequently the efficiency of the system.
- The sampling rules derived from this study are employed to design a specific FPA with the optimal distance between antennas, aperture diameters, efficiency of the reflector and efficiency of the antenna.

- With a Gaussian tapered field distribution and a double sampling condition, one can obtain spillover and taper efficiencies of 90% (aperture efficiencies of 83%).

5.3 Micro-lens Focal Plane Array Design

In this section, the study of the micro-lens antenna designed in chapter 5 used as a FPA to illuminate a reflector of a given f-number is presented. Figure 5.14 shows the basic scheme of the micro-lens antenna. The design will be focused at 550 GHz as in the previous chapter. The same antenna feed (waveguide+iris+air gap) as the one described will be used in the analysis.

Figure 5.15a and b show the optimum diameter of the lens aperture in order to efficiently illuminate a reflector for a given f-number. The spillover of obtained is around $So^r = 0.25\ dB$ for the three tapers. It can be observed that the results are very similar to the ones obtained in the previous section when a Gaussian illumination feed was used. This conclusion is understandable as the gaussicity of this micro-lens antenna is very high (above 80% as shown in chapter 5).

With these graphs and the graphs provided in chapter 5, one is able to fabricate a

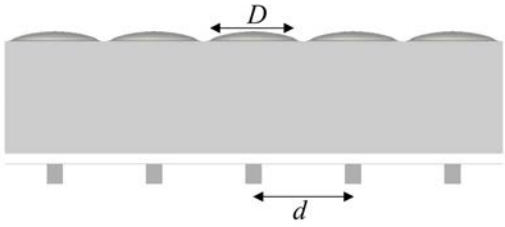

Figure 5.14: Micro-lens antenna array basic scheme.

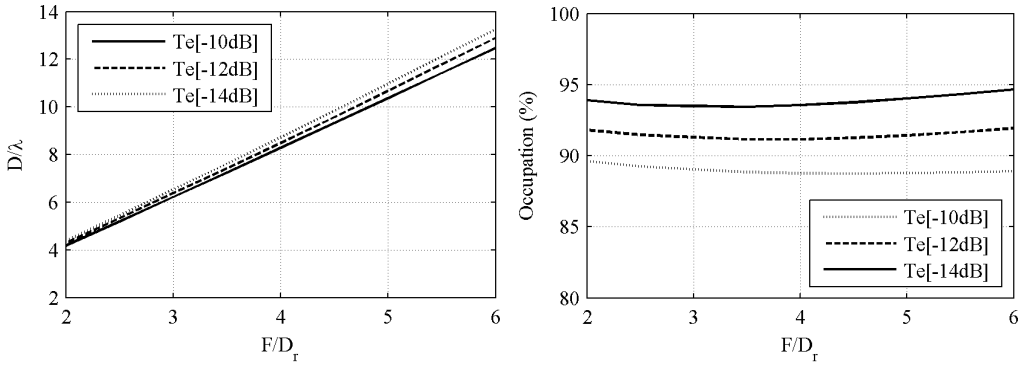

(a) **(b)**

Figure 5.15: (a) Micro-lens diameter illuminating a reflector of F/D_r with taper $Te^r[-11dB]$. (b) Occupation of the micro-lens array illuminating a reflector of F/D_r with taper $Te^r[-11dB]$.

micro-lens antenna array for any given f-number and frequency. This results have been used to design different FPA at different frequencies and for different f-number imaging systems for specific projects in the Jet Propulsion Laboratory, USA. In the following section, a specific micro-lens array design example will be presented for an space mission.

5.4 Design of a FPA for the SOFIA Mission

The SOFIA mission is a space project carried by the Jet Propulsion Laboratory consisting in a modified Boeing 747SP jetliner that carries a telescope with an effective diameter of 2.5 m to altitudes as high as 14 km. By flying above the Earth's atmosphere, the attenuation caused by the water vapor can be avoided allowing scientist to gather and study information about the stars and planets, as well interstellar cosmic elements of the Milky Way Galaxy.

The FPA of SOFIA will host thousands of THz antennas (pixel elements) to achieve a spatial resolutions higher than the state of the art instruments. In this section, the design of an antenna is presented, working as FPA for a double sampling condition with a $Te^r[-11\ dB]$ reflector taper, an f-number of $F/D_r = 19$ and a frequency range from 1.8 THz to 2.1 THz, being the central frequency 1.95 THz. Note that the lens dimensions depends on the primary feed taper that is chosen. Ideally, the largest possible taper would reduce spill over losses. However this means a larger lens diameter and consequently a smaller spacing between them. Therefore, three tapers -10,-12 and -14 dB of the antenna have been studied that allow flexibility of selection depending on the fabrication capabilities of the micro-lens array.

5.4.1 Antenna Feed

The antenna is feed is based in the same design proposed in the previous section. However in this case, two double slots have been used as the iris in order to obtain a double polarization and propagating the two TE_{10} of the square waveguide.

The basic scheme of the iris is found in Figure 5.1. As it is shown the edges of the slots have been rounded with a radius R_c due to the fact that sharp edges could not

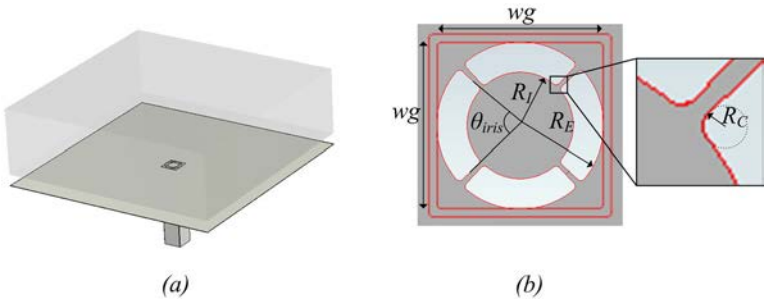

Figure 5.16: Iris design of the SOFIA antenna feed.

SOFIA Iris Dimensions

f	$1.95THz$	F/D	19
t	$2.2\mu m$	wg	$112\mu m$
s	$2.7\mu m$	h	$79\mu m$
R_E	$56\mu m$	R_C	$2.8\mu m$
R_I	$35\mu m$	θ_{iris}	$86deg$

Table 5.1: Dimensions of the designed iris at 1.9 THz.

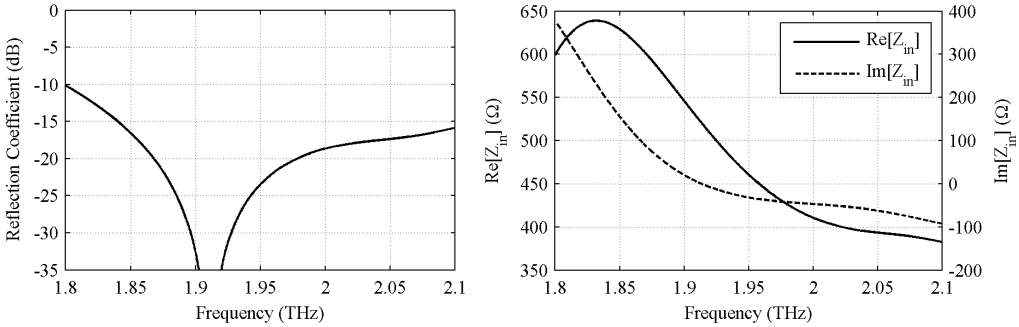

Figure 5.17: (Left) Reflection coefficient and impedance (Right) on the antenna feed in Figure 5.16

be obtained in the fabrication process. Moreover, the separation of the slots should be greater than the membrane thickness which should be from $1\mu m$ to $3\mu m$. The dimension of the slots have been optimized considering these fabrication constraints and the final dimensions of the iris are found in table 5.1.

As it is shown in Figure 5.17(Left) a good matching below -15 dB is obtained in the whole frequency band of interest. The input impedance of the antenna is shown in Figure 5.17(Left), where the resistance is matched with the waveguide impedance of the mode TE_{10} (for a square waveguide of 112 μm it corresponds to 518 Ω). Both results, the reflection coefficient and input impedance have been obtained by the simulation of the waveguide with the iris and an infinite silicon medium on top, using MW CST.

5.4.2 Micro-Lens FPA

As it has been already introduced, the micro-lens is designed to be coupled to the SOFIA optical system of $F/D_r = 19$. The optimal dimensions of the micro-lens obtained in chapter 5 were extrapolated for high f-number reflectors. As Figure 5.18 shows, the diameter of the micro-lens aperture that would efficiently illuminate an optics system of f-number $F/D_r = 19$ would be around 6.4 mm (or 40.5λ). In table the final dimensions of the micro-lens are presented for -10, -12, -14 dB antenna field tapers.

Once the dimensions of the micro-lens are obtained and before proceeding with the fabrication, the antenna disposition in the FPA grid is studied. In the previous analysis, the beam separation and the illumination efficiency were optimized for a linear FPA as

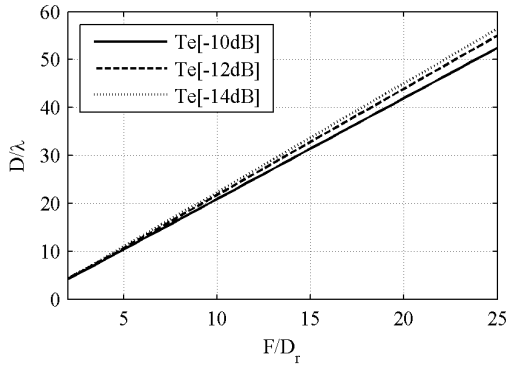

Figure 5.18: Micro-lens aperture diameter illuminating a reflector with a taper of $Te[-11dB]$, as a function of F/D_r

SOFIA Micro-Lens Dimensions

	D/λ	D (mm)	W/λ	W (mm)	R/λ	R (mm)	H/λ	H (μm)
$Te[-10\ dB]$	40.23	6.19 mm	103.91	15.66 mm	79.42	12.22 mm	2.584	397.6 μm
$Te[-12\ dB]$	41.47	6.38 mm	100.59	15.48 mm	76.38	11.75 mm	2.866	441.0 μm
$Te[-14\ dB]$	42.82	6.58 mm	97.61	15.02 mm	73.65	11.33 mm	3.181	489.5 μm

Table 5.2: Dimensions of the microlens antenna for different tapers at 1.9 THz and for a $F/D_r = 19$.

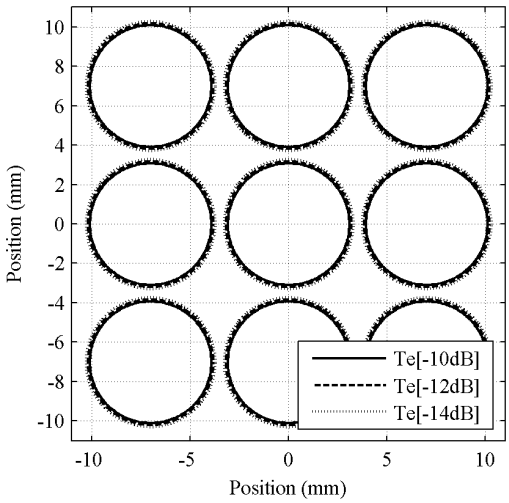

Figure 5.19: Square grid footprint for a FPA of $F/D_r = 19$.

the one shown in Figure 5.14. A more realistic scheme would contemplate the spacing and the sampling of a two dimensional array for the antenna disposition in the FPA, designed to cover the whole field of view of the image.

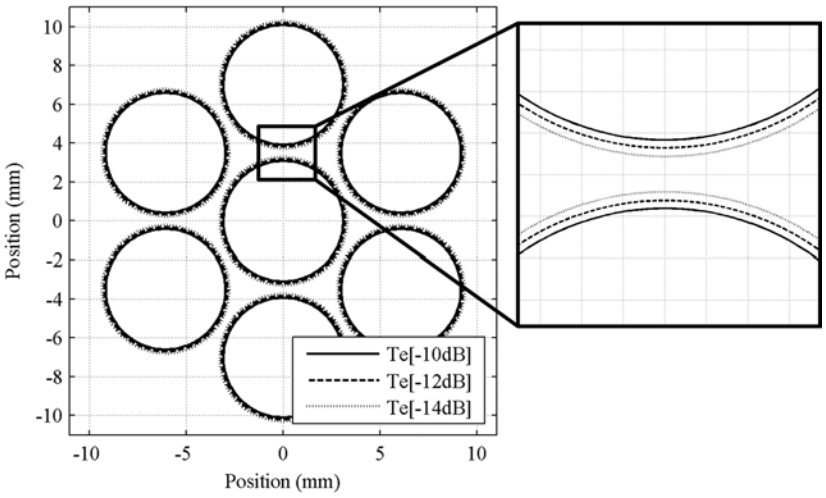

Figure 5.20: Hexagonal grid footprint for a FPA of $F/D_r = 19$.

The initial footprint of the imaging plane is shown in Figure 5.19 where the micro-lenses are placed at a distance d from each other in a $d_x = d_y$ direction in a squared grid. However, as it is shown in the scheme, there are important unsampled spots (specially along the 45 deg direction) in the field of view.

In order to improve the field of view coverage, an hexagonal grid provides a better coverage compared to the square grid maintaining the same illumination efficiency. Figure 5.20 shows the hexagonal grid disposition of the micro-lenses placed at a distance $d_x = d\cos 30$ and $d_y = d\sin 30$. Note the footprint is shown for three different antenna tapers (-10, -12 and -14 dB). Ideally, the largest possible taper would reduce spill over losses. However this means a larger lens diameter and consequently a smaller spacing between them. The grid spacing is limited by the capabilities and accuracy of the fabrication process of the micro-lens as it will be presented in the next chapter.

6

Chapter 6
Micro-Lens Antenna Prototypes - Fabrication and Measurements

Monolithic[1] Integrated Circuits (MIC) can be referred as one of the key technological achievements of the last decade because of their ability to integrate multifunction circuits on a single chip. From the antenna point of view, it is important that the antennas can be integrated in the same fabrication process within the rest of the device electronics in order to reduce the size and improve the performance (low losses) of the overall systems.

In chapters 4 and 5, the design of a micro-lens antenna compatible with silicon micromachining techniques has been presented. This antenna allows a wafer level integration for array manufacturing and full integration with the rest of the components of the transceiver. There are two possible ways to fabricate an array of the micro-lens antennas

[1]The following sections contain portions, sometimes verbatim, of the publications [JA1, JA3] of the author.

presented: using advanced laser micro-fabrication techniques or using optical photolithography. The laser technique allows fabrication of advanced three dimensional geometries. The drawback is that such a technique is a linear process which may not be cost-efficient for large arrays in applications like the imager radar. The photolithographic technique instead allows the fabrication of all the elements of the array at once. This following chapter is focused on the fabrication process of this antenna and the measurements of the built prototypes. Two prototypes have been assembled: one using photolithography techniques and another one using laser micro-fabrication. The results obtained for both prototypes are presented below.

6.1 Micro-Lens Antenna Fabrication

In this section, the micro-lens antenna fabrication process is presented. The antenna array presented in the previous chapter can be assembled in three parts as it is graphically shown in Figure 6.1a: a high resistivity silicon wafer containing the shallow lenses, several layers of high resistivity silicon wafers that define the height of the lens, W, and a gold platted double Silicon on Insulator (SOI) wafer containing the primary feed composed by the waveguide, iris and cavity. In the following sections, the fabrication process for the two main antenna parts are described in detail.

6.1.1 Fabrication of the Leaky Wave Waveguide Feed

This feed is composed of a rectangular waveguide loaded by a double slot iris and a resonant air cavity as described previously. These three elements can be fabricated on the same double SOI wafer, using a three-steps etch process.

The wafer consists on a very thin membrane of 17 μm of silicon for the iris, with two SiO_2 layers on the top and the bottom to act as etch-stops. The top SiO_2 layer is covered with a silicon wafer of 272 μm of thickness which is determined by the height of the air cavity, the bottom etch-stop is mounted on a silicon wafer with a thickness of 995 μm to create to square waveguide (see Figure 6.2). These three elements were fabricated using conventional photolithography techniques, combined with inducted coupled plasmas for SiO_2 etches and Deep Reactive Ion Etching (DRIE) for deep selective silicon trenches. By working around the pressure and the plasma power in DRIE, we were able to achieve a very selective recipe of 300 : 1, allowing the fabrication of clean and perfectly controlled iris membranes. After fabrication, these wafers were sputtered with a 2 μm thick layer of gold.

6.1.2 Fabrication of the Silicon Shallow Lens

In this section, we present the fabrication of an antenna prototype that could be used with the optical system described in [15]. Such system was characterized by an f-number of 2 implying a lens diameter of approximately 2.5 mm

Since we utilize the mass production feature of silicon micro-machining technique, we could micro-fabricate almost unlimited numbers of silicon shallow lens arrays onto

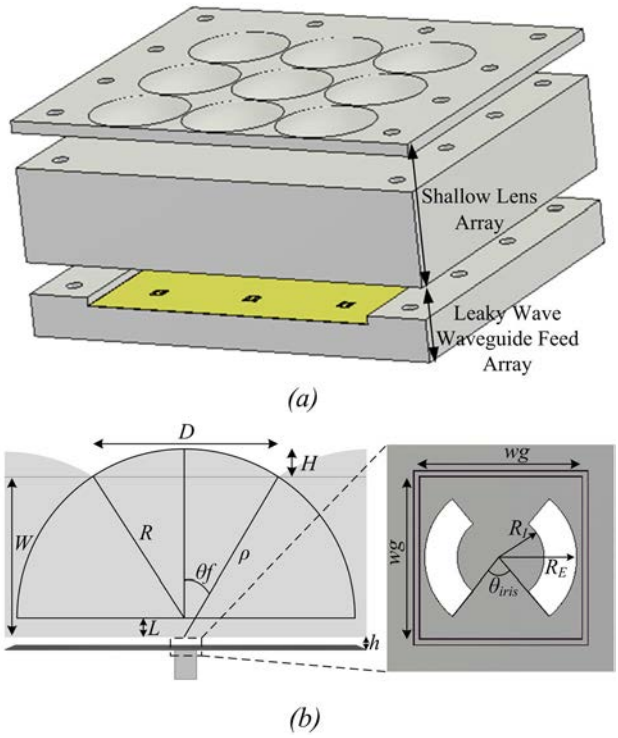

Figure 6.1: Geometry of an array of shallow lenses illuminated by a leaky wave waveguide feed array: (a) three dimensional and (b) side views.

silicon substrate by using both thermal reflow of photoresist and selective Reactive Ion Etching (RIE). The basic idea of microfabricating silicon shallow lenses is to transfer the lens shape made into photoresist onto the silicon wafer by RIE as it is shown in Figure 6.3. The process consists in four steps:

1. Pattern the photoresist in the silicon wafer with the desired lens aperture.
2. Reflow the photoresist pattern with heat in order to obtain the lens profile.
3. Etch the photoresist and silicon simultaneously by using a RIE process in order to transfer photoresist lens onto silicon substrate.
4. The process finishes when a complete etching is achieved and the lens profile is transferred to the silicon wafer.

In this proposed technique, we have controllability on both diameter and curvature of silicon lens. First of all, the diameter of the lens depends on the thickness of the photoresist that we can coat and pattern. So far, the diameter of 6 mm photoresist lens with 400 μm in height has been successfully micro-fabricated. Based on our experiences, diameters larger than 1 cm photoresist shallow lens array would be feasible. The curvature of the shallow lens can be controlled by two process variables:

Amount of photoresist It determines the curvature of the photoresist lens. Since we

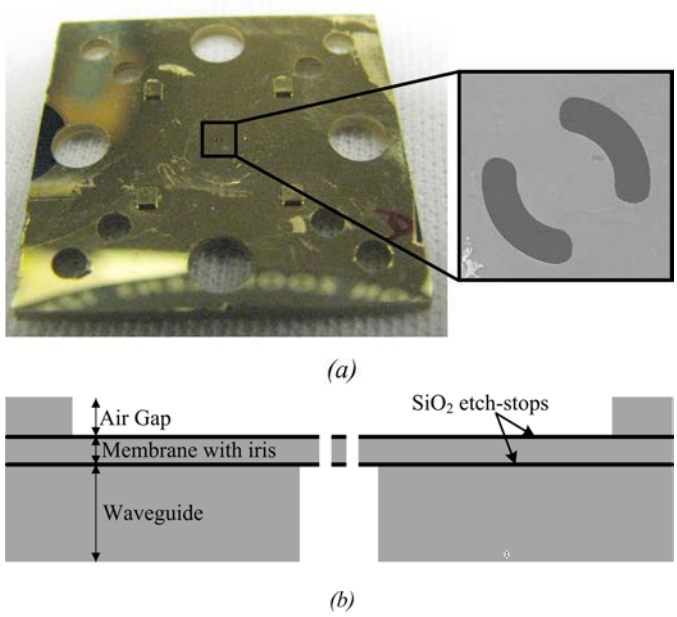

Figure 6.2: (a) Photograph of the fabricated leaky wave waveguide feed and close-up on the double slot iris in SEM. (b) Diagram of the double SOI wafer.

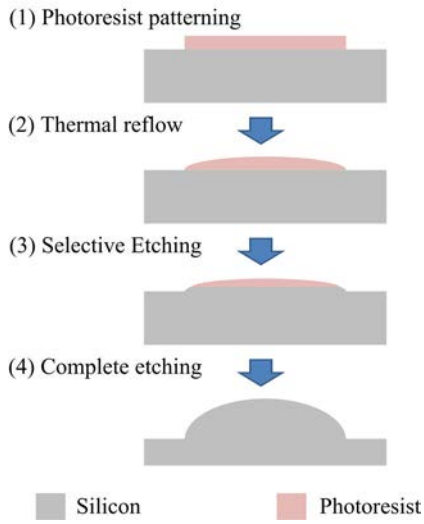

Figure 6.3: Sketch of the micro-fabrication process of the silicon shallow lenses.

transfer photoresist lens onto the silicon substrate, it will directly control the curvature of silicon shallow lens.

Etching selectivity between photoresist and silicon Photoresist lens is formed by thermal reflow. In order to transfer the exact photoresist curvature onto silicon, we

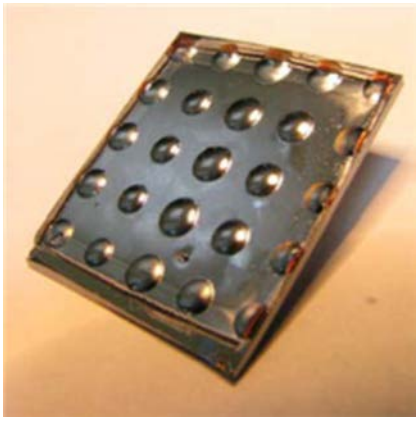

Figure 6.4: Fabricated array of silicon shallow lenses.

need to have etching selectivity of 1 : 1 between silicon and photoresist. However, by varying the etching selectivity, we could control the curvature of the silicon lens. For example, if photoresist etches at half etch rate of silicon etch rate, the curvature of the silicon lens will be two times higher. Thus, we could utilize the plasma etching process parameters such as gas ratio between CF_4 and O_2, bias power, and RF power in order to control the etching selectivity.

An array of 5x5 silicon shallow lens has been micro-fabricated as it is shown in Figure 6.4. The lens located in the center of the array has been characterized and analyzed. First of all, we have measured the 3-D profile of shallow lens surface as it is shown in the inset of Figure 6.5. It has a nice smooth curvature and a diameter of 2.5 mm. Secondly, we have measured the height of silicon shallow lens. In this case, the original height of photoresist was $210\mu m$. Because of the etching selectivity of 1.3 between photoresist and silicon, the height of silicon shallow lens is about $280\mu m$. Thirdly, we have measured the surface roughness of silicon shallow lens using a Dektak surface profilometer with a vertical resolution of 15 nm (see Figure 6.5). The peak-to-peak surface roughness is less than 0.5 μm which is adequate in THz frequency. For example, the surface roughness should be less than $7\mu m$ at 600 GHz range.

In order to evaluate the fabrication accurateness, the lens fabricated surface was analyzed by doing a fit into a perfect sphere surface, i.e. the designed surface. The best fitting sphere was obtained by minimizing the error of the fabricated surface and a certain sphere surface of radius R, diameter D and height H using the optimization toolbox in Matlab. The dimensions of the best fitting sphere are $R = 3.90\ mm$, $D = 2.93\ mm$ and $H = 285.6\ \mu m$, obtained by minimizing the error between both surfaces. The standard deviation was calculated to be $\sigma = 18.36\ \mu m = 0.11\lambda_d$, which may inflict severe aberrations the radiation pattern of the antenna and in the optical system. As it is shown in Figure 6.6, the edges of the lens do not provide a good fit with the designed sphere, containing the higher error. In order to diminish the lens surface distortion, the bottom part of the lens (area shown in gray in Figure 6.6) were the error was considerably higher was not taken into account and only the top part of the lens was illuminated by the antenna feed, reducing the error to $\sigma = 5.4\ \mu m = 0.04\lambda_d$. Hence, an effective diameter

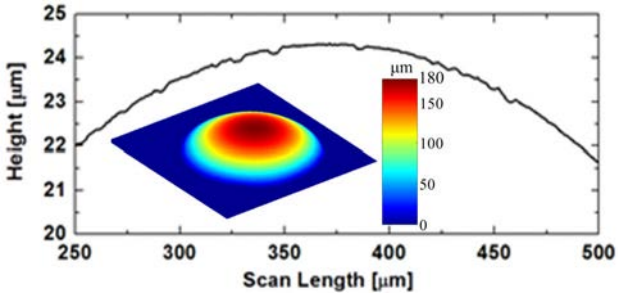

Figure 6.5: 3-D plot and top of the surface profile of the silicon shallow lens profile. It shows less than $1\mu m$ peak-to-peak surface roughness.

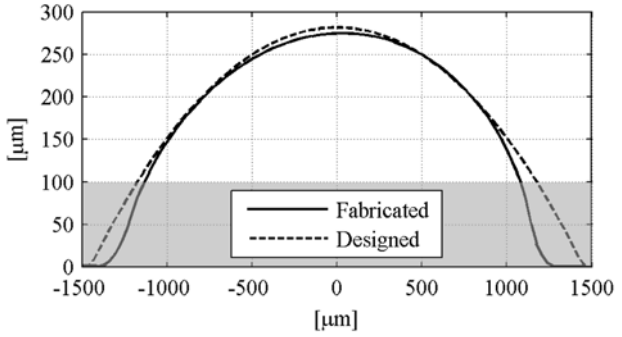

Figure 6.6: Surface profile 1D cut of the shallow lens surface and the best fitted sphere cut.

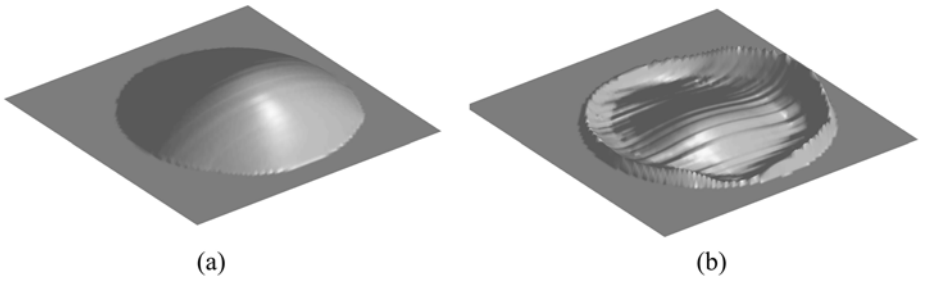

Figure 6.7: 3D view and of the (a) fabricated lens surface and the (b) surface distortion between the shallow lens surface and the perfect sphere.

of 2.38 mm was considered in the antenna design instead of the original 2.93 mm. This adjustment in the illumination will be achieved by an adjustment of the thickness of the lens W that in this case, it will be designed to obtained a field taper of -14 dB at the border of this new effective lens aperture.

Figure 6.7b shows the surface distortion of the shallow lens calculated as the difference between the fabricated (see Figure 6.7a) and the designed surface (notice that 100 μm of the bottom part of the shallow lens has been ignored as it has previously been explained).

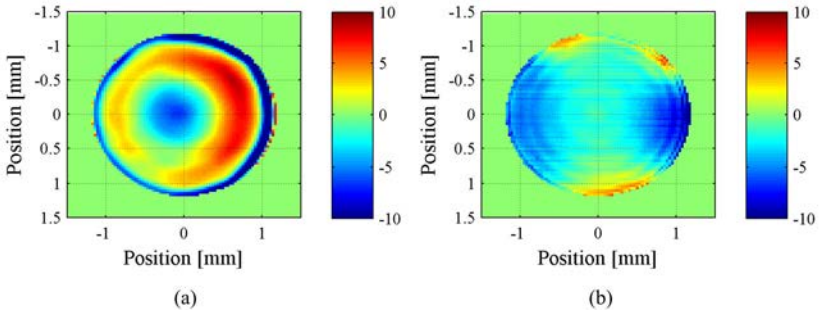

Figure 6.8: (a) 2D view of the reconstructed Zernike polynomial decomposition of the error surface of the lens. (b) Difference between the reconstructed Zernike polynomial decomposition and the error surface of the lens.

This surface distortion was decomposed in optical aberrations and studied using a Zernike polynomials expansion in order to evaluate the behavior and performance of the fabricated lens profile. In Appendix 3 further details about the effects of the lens surface distortions on the radiated fields of the micro-lens antenna are presented. Zernike polynomials were used to define and classify the deviations from a zero mean surface error; in this case, the surface resulting from the difference between the shallow lens and the best fitted sphere surface. 190 polynomials were been used to expand the error surface of the lens profile (see the table of polynomials in Appendix 3), giving an Root Mean Square (RMS) error between the error surface and the Zernike polynomial reconstructed surface of $RMS = 2.2\ \mu m$, which is not significant. Figure 6.8a shows the 2D view of error surface of the lens reconstructed from the Zernike polynomial decomposition. And Figure 6.8b shows the difference between this reconstructed error surface of Zernike polynomial decomposition and the error surface from Figure 6.8b. By decomposing this surface in the Zernike coefficients it was detected that shallow lens suffered mainly from spherical aberrations (25.4% of the global surface distortion) and coma (22.7%). The shallow lens also suffered in a smaller proportion from astigmatism (6.4%) and defocus (2.2%). In Figure 6.9 we can see the corresponding Zernike surfaces of the spherical (a), coma (b) astigmatism (c) and defocus (d) polynomials.

The spherical aberration contribution (see Figure 6.9a) corresponds to the polynomials of $n > 2$ and $m = 0$. It represents in this case the major error with a 25.4% of the total aberration error. Spherical aberration causes beams distant from the lens axis to be focused in a different place than beams close to the axis. The effect of this aberration in the lens is considered as a phase distortion in the aperture fields. In order to understand this effect, the radiation pattern of a lens illuminated with a tapered Gaussian aperture with a field edge taper of 14 dB has been studied. The aberration contributions, in this case the spherical, has been translated as a phase contribution to the aperture field of the lens; and the radiation pattern is then obtained by calculating the FFT of the resulting aperture field. Figure 6.10a and b shows the radiation pattern calculated for the same aperture considering the effect of the spherical aberration (black line) in comparison with the radiation pattern without aberrations (grey line). Note that the x-cut corresponds to the cut along the longitudinal axis of Figure 6.10b and the y-cut corresponds to the transversal cut. It can be observed that the spherical aberrations are translated to an

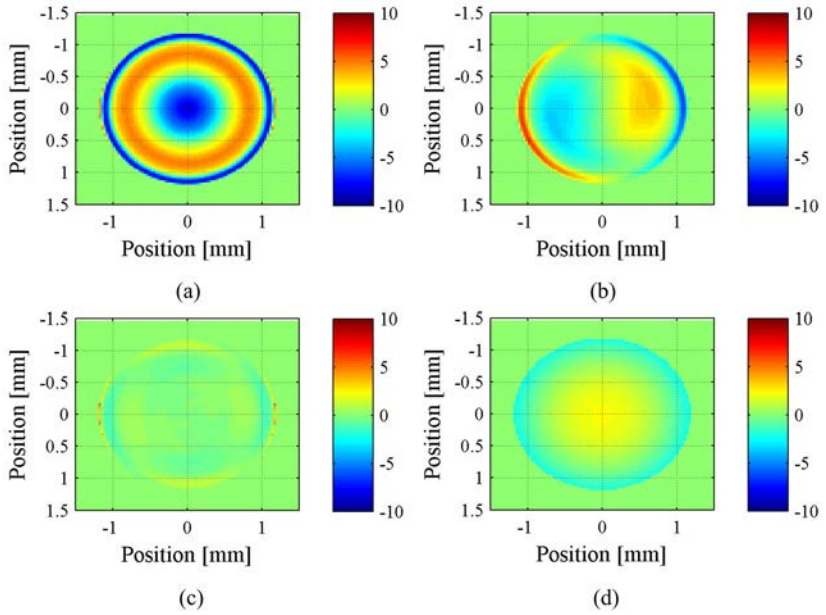

Figure 6.9: Decomposition of the shallow lens surface distortion in Zernike polynomials of (a) Spherical, (b) Coma, (c) Astigmantism and (d) Defocus

increase by 5 dB of the secondary lobes.

The coma aberration contribution (see Figure 6.9b) corresponds to the polynomials of $n > 1$ and $m = \pm 1$. The error that represents this aberration in the total error of the fabricated lens is a 22.6%, which is highly significant. In this case, the rays that pass through the outer margins of the lens are focused at different points, either further from the axis (positive coma) or closer to the axis (negative coma). As it is shown in the radiation pattern of Figure 6.10c and d, the coma aberration performs a tilt in the main and secondary lobules of the field in the y-cut (a cut along the transversal axis) direction.

The astigmatism contribution (see Figure 6.9c) corresponds to the polynomials of $n > 2$ and $m = \pm 2$ and only represents the 6.38% of the total aberration error. And the defocusing contribution (see Figure 6.9d) corresponding to the polynomials of $n = 2$ and $m = 0$) only represents the 2.17%. These two aberrations do not inflict a significant impact in the performance of the radiation pattern.

The radiation pattern including all the aberrations is shown in Figure 6.10e and f compared to the radiation pattern without aberrations. It can be observed that the main contribution of all the aberrations is an increase of the secondary lobes and the tilt in the x-cut; and it corresponds to the combination of the spherical and coma aberrations previously described.

This fabrication process is still under development in order to achieve surface accuracy and repeatability for the fabrication of large arrays of lenses. Up to now, new advances in the reduction of the surface error at the border of the lens and improvements in the uniformity of the surface have been presented in [72]. Preliminary results of the fabrication

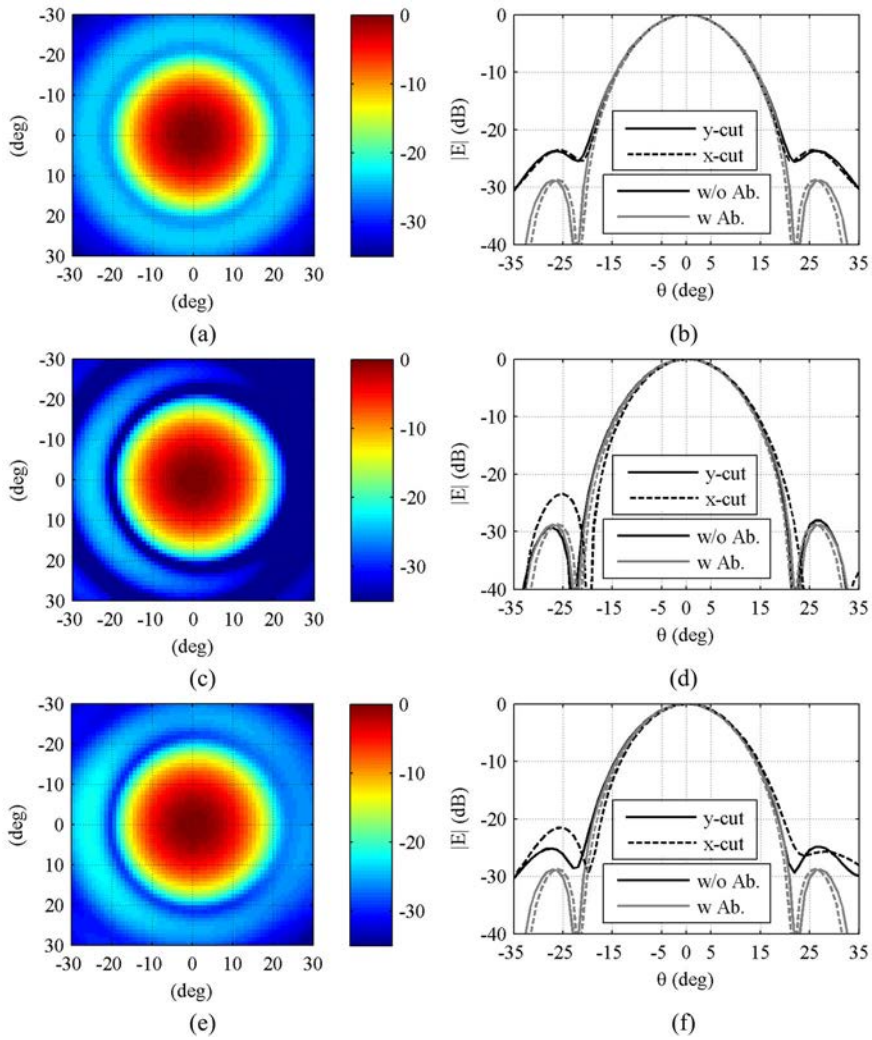

Figure 6.10: Radiation patterns of a Gaussian aperture with a field taper of 14 dB considering (a),(b) Spherical Aberrations; (c), (d) Coma Aberrations; (e), (f) All the aberations.

of large arrays are also presented in [72].

6.2 Micro-lens Antenna Prototypes and Measurements

6.2.1 Micro-lens Antenna Fabricated with Photolithographic Micromachining Techniques

Once the shallow lens surface was fabricated and analysed as described in the previous section, the rest of the antenna dimensions were adjusted to maximize the aperture ef-

Lens Dimensions			
f	550 GHz	h	273 μm
D	2.38 mm	wg	409 μm
W	3.21 mm	tgp	17 μm
R	3.99 mm	θ_{iris}	79 deg
L	-599 μm	R_I	109 μm
θ_f	20.32 deg	R_E	191 μm

Table 6.1: Dimensions of the designed micro-lens antenna photolithography fabricated prototype.

ficiency at 550 GHz, the central frequency of the band. The optimum dimensions for a primary field taper of -14 dB and a diameter of $D = 2.38$ mm are shown in Table 6.1 and were obtained following the design procedure described in chapter 5.

The performance of the designed antenna was evaluated using a PO method over the whole frequency band. Figure 6.11(Left) shows the directivity and the gain as a function of the frequency. The gain includes the spillover losses (defined as the amount of power transmitted by the antenna feed that is not caught inside the aperture of the shallow lens) and the reflection losses inside the lens with and without the use of a matching layer. As it is shown, the use of a matching layer of thickness $\lambda/4$ at the central frequency improves significantly the performance of the antenna and has a good behavior in the whole frequency band as the antenna operates over a relatively small bandwidth. Moreover, the fact that we are employing shallow lenses simplifies the fabrication of this matching layer.

Because the main application of this antenna is to work as a focal plane array, the evaluation of the coupling between the antenna and the optical system is a substantial parameter to be considered. This coupling can be studied by calculating the Gaussicity [69]. As it is shown in Figure 6.11(Right), a high value of Gaussicity is achieved over the whole frequency band.

The designed thickness of the substrate was calculated to be 3.21 mm (see Table 6.1). To achieve the desired thickness, five pieces of high resistivity ($\rho = 10$ $k\Omega \cdot cm$) double side polished silicon wafers were placed in between the primary feed and the shallow lens wafer. Note that these wafers do not need to be aligned. Thus, the antenna thickness was achieved by the use of the five silicon wafers of 550 μm each, the shallow lens wafer of 422 μm and the 100 μm of the bottom part of the shallow lenses that was not illuminated, obtaining an overall thickness of 3.15 mm.

6.2.1.1 Antenna Prototype Measurements

A prototype working at 550 GHz was fabricated (see Figure 6.12) and measured using an ABmm network analyzer [73]. The network analyzer is connected to the antenna through a waveguide as shown in the right side of Figure 6.12(Left). A transition machined in an aluminum split block is used to match the output of the ABmm waveguide to the square waveguide of the antenna. The transition is followed by the antenna feed wafer (the gold

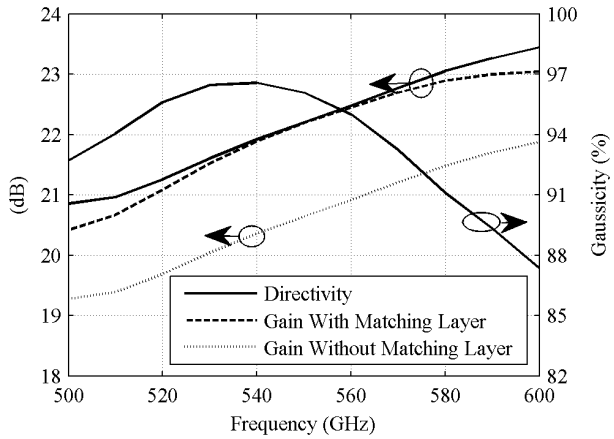

Figure 6.11: Frequency analysis of the designed antenna. (Left) Directivity and gain. (Right) Gaussicity calculated for a Gaussian beam divergence angle of $\theta_0 = 11°$.

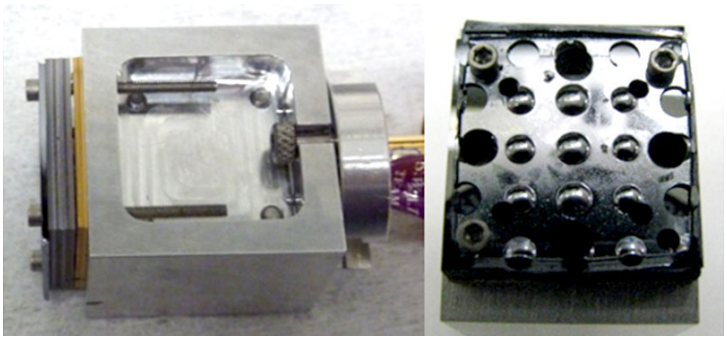

Figure 6.12: Side and top views of the 550GHz antenna prototype.

wafer in Figure 6.12(Left)), the air cavity (corresponding to the space in between the gold wafer and the silicon wafers), and a stack of silicon wafers used to match the lens surface and ended with the micro-machined lens (last silicon wafer in Figure 6.12(Left)). The antenna primary feed and the lens profile used for the prototype are the ones described in the previous section. The top of the lens antenna is shown in Figure 6.12(Right). Note that from the array of lenses only the central lens has been measured. The lens and feed wafers were aligned using holes and metal screws. In order to have a better alignment in the future, a novel wafer to wafer alignment technique using silicon pins is currently being developed and tested.

The measurement set up is shown in Figure 6.13(Left). The ABmm measurement system is composed of two heads: one head where the prototype antenna was connected (see Figure 6.13(Right)) and another head where a standard horn antenna was placed. Two rotating stages were employed to move the antenna in elevation and azimuth in order to scan the far-field. The scanning range was limited to 45 deg approximately, in both planes.

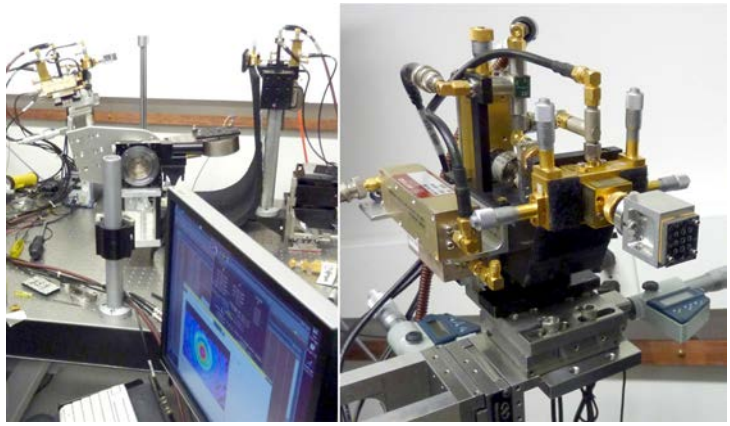

Figure 6.13: (Left) Main view of the measurement set up. (Right) Close up image of the antenna mounted on the ABmm head.

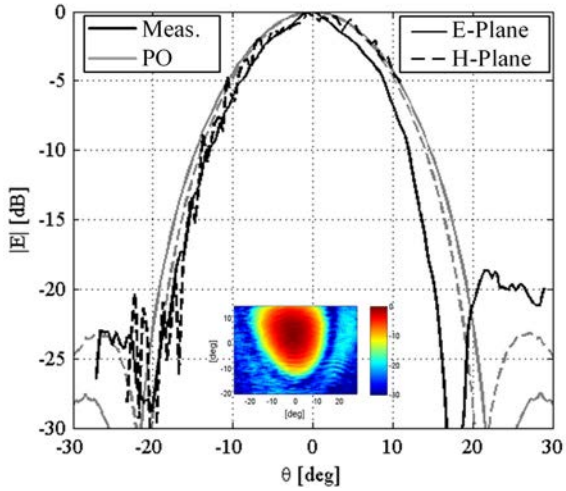

Figure 6.14: Measured radiation pattern at 530 GHz of the micro-lens prototype fabricated using photolithography techniques.

Figure 6.14, 6.15, 6.16 and 6.17 show the main cuts of the measured far field patterns. The measurements are compared to the simulations obtained with the PO for an ideal extended hemispherical lens antenna fed by the leaky wave waveguide described in Table 6.1. The insets of the figures display the measurements of the two dimensional views of the pattern amplitudes. As it can be observed, the lens does not give a complete agreement with the PO simulations. These differences are mainly caused by the aberrations of the shallow lens surface (as it has been explained in the previous section) increasing the secondary lobes because of the presence of spherical aberrations, and also causing an asymmetry in the antenna far field patterns due to the presence of coma aberrations. Also, a possible misalignment between the lens and the primary feed beam could also

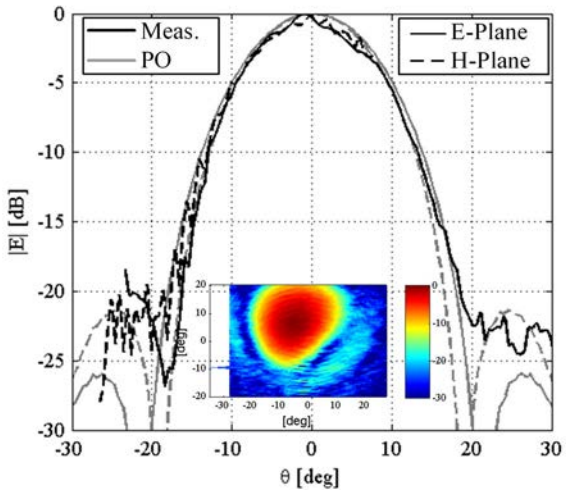

Figure 6.15: Measured radiation pattern at 550 GHz of the micro-lens prototype fabricated using photolithography techniques.

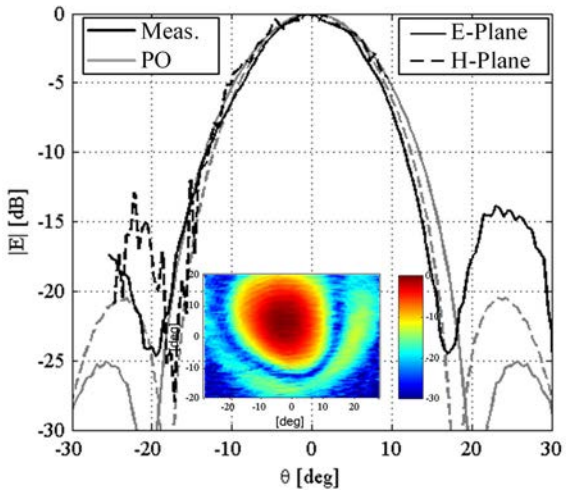

Figure 6.16: Measured radiation pattern at 560 GHz of the micro-lens prototype fabricated using photolithography techniques.

contribute to a tilt in the antenna pointing direction and asymmetry in the antenna far field. Even so, the measured patterns present a well focused beam very similar to the design one enabling the use of such shallow lens antenna for illuminating a reflector.

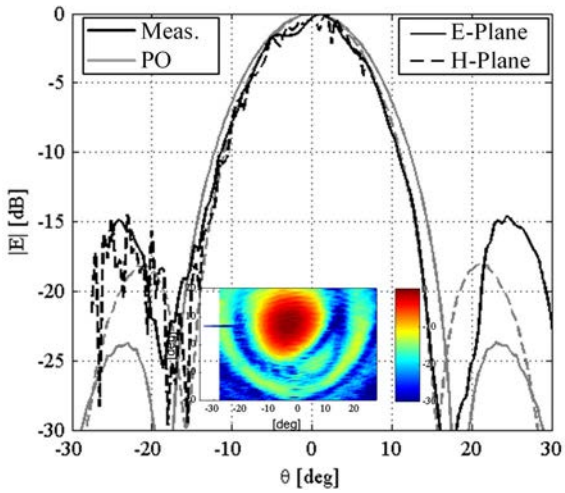

Figure 6.17: Measured radiation pattern at 590 GHz of the micro-lens prototype fabricated using photolithography techniques.

Lens Dimensions

f	550 GHz	h	272 μm
D	5 mm	wg	409 μm
W	11.39 mm	tgp	17 μm
R	10.63 mm	θ_{iris}	79 deg
L	1.06 mm	R_I	109 μm
θ_f	12.37 deg	R_E	191 μm

Table 6.2: Dimensions of the designed micro-lens antenna laser micro-fabricated prototype.

6.2.2 Micro-lens Antenna Fabricated with Laser Micro-machining Techniques

A prototype has been fabricated as a proof of concept of the antenna design methodology shown in chapter 5. The prototype has been designed for a diameter of $5mm$ and a field taper of -10 dB at a central frequency of 550 GHz. The optimum dimensions of the micro-lens antenna are shown in Table 6.2 and were obtained following the design procedure described in chapter 5.

Figure 6.18(Left) shows the directivity and the gain as a function of the frequency. The performance has been evaluated using the PO method explained in chapter 5 over the whole frequency band. The gain includes the spillover losses and the reflection losses inside the lens with and without the use of a matching layer. Like in the previous prototype, the performance of the antenna improves significantly with the use of the matching layer. High Gaussicity is also achieved in the whole frequency band.

The prototype was built with the same procedure as the previous prototype: assem-

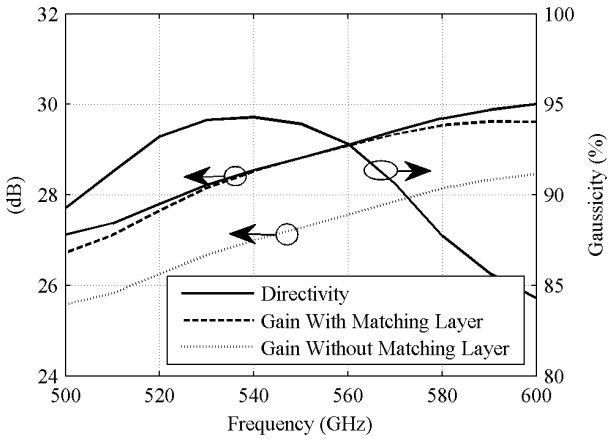

Figure 6.18: Frequency analysis of the designed antenna. (Left) Directivity and gain. (Right) Gaussicity calculated for a Gaussian beam divergence angle of $\theta_0 = 11°$.

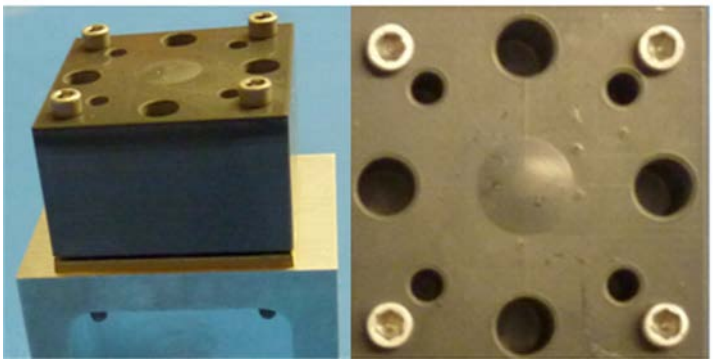

Figure 6.19: (Left) Final assembly of the lens antenna. (Right) Lens surface fabricated with laser micro-machining.

bling a waveguide split aluminum block, a waveguide/slot-iris/air-gap wafer, and a silicon micro-lens; each one fabricated separately (Fig. 6.19). The waveguide, slot iris, and the air cavity are the same as the ones used for the previous prototype. The silicon micro-lens, which is placed on the top of the stack, has been fabricated with a laser micromachining process [62]. Unfortunately a matching layer could not be included in the prototype fabrication. Even so the measured patterns resembled the simulated ones.

Measurements were performed where performed with the same procedure explained in the previous section. The main cuts of the measured far field patterns are shown in Figs. 6.20 through 6.22 at different frequencies. They have been compared to the simulated results obtained with the physical optics. As it can be observed, the lens gives a good performance for the whole band and agrees well with the simulations. The minor divergences between the measurements and the PO simulations can be due to the effects of the multiple reflections.

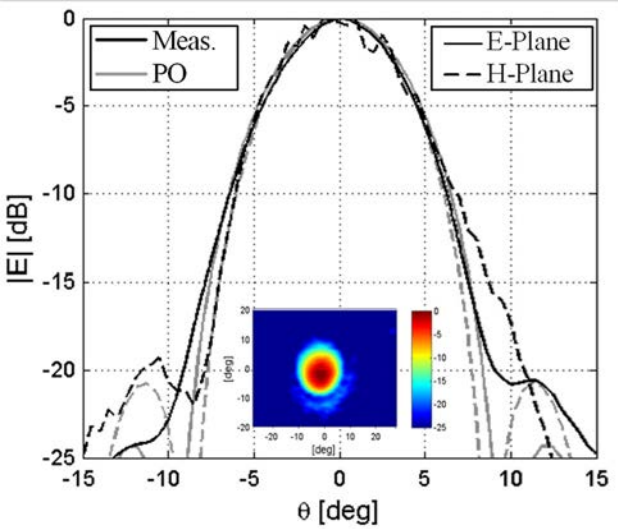

Figure 6.20: Measured radiation pattern at 540 GHz of the micro-lens prototype fabricated using laser micro-machining techniques.

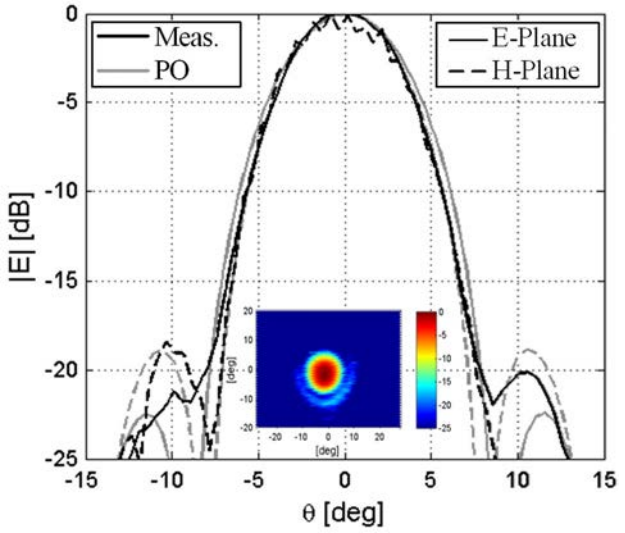

Figure 6.21: Measured radiation pattern at 560 GHz of the micro-lens prototype fabricated using laser micro-machining techniques.

All in all, the use of the lens antennas fabricated with photolithographic processes have a lot of potential in the development of future FPAs. In order evaluate the uniformity and accuracy of the lenses profile, the lens aberration study presented before could be integrated within the fabrication process to facilitate the optimization.

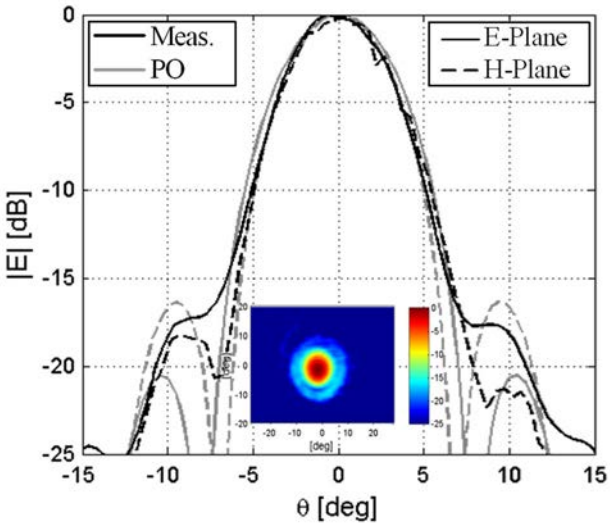

Figure 6.22: Measured radiation pattern at 590 GHz of the micro-lens prototype fabricated using laser micro-machining techniques.

7

Chapter 7
Conclusions

7.1 Main Conclusions

This doctoral thesis has focused on the development of integrated antenna arrays at Terahertz frequencies for imaging applications with a special emphasis on the technologies and the fabrication capabilities that can be potentially used and are currently available. This frequency band has proven its potential for imaging applications thanks to the good compromise between spatial resolution and penetration; however, this push towards high frequencies contains many technological difficulties in all the subsystems involved in the signal generation, transmission and detection. The power budget restrictions and high losses that sources and receivers currently suffer at these frequencies require systems with a high level of integration among all the devices and components of the systems and subsystems. Therefore, the antennas needed for these systems require to be integrated within the same fabrication processes and technologies as the sensing and power converting devices that are used at their terminals.

The current imaging systems require large array of antennas in order to achieve the

high speed image acquisition that is required in most THz applications. This fact increases considerably the difficulty and complexity to achieve highly integrated and efficient antennas. This thesis has characterized and analyzed these difficulties and provided solutions to the development of antenna arrays at millimeter and submillimeter wave frequencies. Due to the different nature and characteristics of the antennas that require near-field and far-field imaging systems, this research has been divided in two main study areas, respectively:

- **Integrated Planar Antenna Arrays**

  This research has focused on the study of a planar antenna array, called retina, for a specific near-field imaging system based on MST at millimeter and submillimeter-wave frequencies. This system has been selected for its capabilities to perform high speed imaging and because it does not require a high frequency distribution line network. However, it is hindered by different technological difficulties: the selection of an antenna geometry that achieves high efficiency, the selection of the adequate active element and its integration with the antenna. In this thesis, these challenges have been addressed and studied in-depth. Not only that: while other researchers have been focused on the optimization of the antenna impedance solely, this thesis has developed a design methodology that integrates all the different aspects of the system.

  The performance of the system has been defined by the maximization of the differential transmission coefficient which will determine the SNR of the system and, as a consequence, the dynamic range of the image. Furthermore, this parameter can be dissected among the following three properties. First, the ME that indicates the matching level between the antenna and the active element impedances. Second, the surface wave efficiency which quantifies the amount of power loss due to the surface wave modes that propagate inside the substrate as a result of the lack of scalability of its thickness at millimeter and submillimeter wave frequencies. Third, the coupling efficiency among the illuminator, the retina and the collector. These three parameters allow the understanding of the system efficiency and therefore they will help in the design process of the system.

  The retina is a planar array of antennas that couples the radiation to both sides for the array (from the illuminator to the collector) and requires, therefore, a front-to-back ratio close to one. Because planar antennas at millimeter and submillimeter wave frequencies suffer from high losses due to the surface wave modes inside substrate, these losses have been analyzed and quantified for the different antennas, as well as the number of modes propagated. The selected antenna geometry is composed of two ground planes on both sides of the substrates in order to use thicker substrates and a double slot printed on each ground plane that suppresses the TM mode and generates a front-to-back ratio close to one. To our knowledge, this topology has never been employed, and high performances can be achieved, i.e a radiation efficiency of 95% for substrates with a thickness until $\lambda_g/2$. Moreover, this geometry is compatible with the integration of the active element.

  Different switching technologies currently or potentially available at these high frequencies have been considered in order to study and analyze their capabilities and their integration possibilities: PIN diodes, Schottky diodes and RF-MEMS. At

millimeter wave frequencies, PIN diodes can be easily obtained in the market; however, its size begins to be significantly large and the package considerably bulky in comparison with the dimensions of the antenna. This fact degrades the overall performance of the system, as it was observed in the low coupling efficiency obtained in the retina prototype at 100 GHz. On the other hand, at submillimeter wave frequency bands the Schottky diode is the switching technology that is currently being developed and can be utilized. Simulations of the prototype at 300 GHz using this diode showed a higher coupling efficiency due to the smaller size and packaging of the device. However, the performance, i.e the impedance obtained, still needs improvement as a lower ME was achieved compared to the PIN diode. Finally, RF-MEMS switches is a technology with a high potential for millimeter and submillimeter wave frequencies due to its small size, low power consumption and the possibility to be monolithically integrated with the antenna. However, the fabrication process is highly complex and highly unreliable, which was observed in the low yield that was obtained in the RF-MEMS measurements.

High precision fabrication processes such as laser micro-machining and photolithographic techniques were required for the fabrication of all the developed prototypes. The fabrication and assembling tolerances and capabilities play an important role in the antenna development at such high frequencies. Different measurement set ups were fabricated and assembled to validate the different premises presented in the thesis. The alignment of the different components of the system setup and its calibration were significantly challenging due to the small magnitude of all the devices and components. These inaccuracies can strongly affect the performance of the measurements results. Different experimental results were obtained with the fabricated systems, including a set of tomographic images of a canonical scenario with a good agreement with the simulations.

- **Integrated Focal Plane Antenna Arrays**

  A FPA is an array of antennas placed at the focal plane of an imaging system where each antenna points to a different part of the field of view, allowing multiple pixel scanning and increasing the survey speed of the imaging acquisition. The development of FPAs at submillimeter wave frequencies is highly on demand due to the enormous progress in designing integrated heterodyne receivers. These receivers integrate arrays of submillimeter-wave diode-based mixers and multipliers with MIC amplifiers on the same wafer stack. For this stackable multi-pixel terahertz camera technology to work, one would need an antenna array which allows wafer level integration compatible with silicon micro-fabrication techniques for bulk array manufacturing and directive antennas that are able to illuminate a reflector efficiently.

  The antenna geometry employed in this case is based on A leaky wave antenna with silicon micro-lenses has been proven in this thesis to be a viable solution which works well at these frequencies. This antenna achieves high efficiency and high gaussicity in order to be coupled correctly to the optical system. Moreover, this antenna can be fabricated with silicon micro-fabrication techniques. Detailed and thorough design guidelines for this antenna have been performed, allowing to have an antenna with an efficiency above 90% and fabricated in array at THz frequencies.

Basically, two possibilities are available to fabricate such an antenna array: advanced laser micro-fabrication and photolithographic fabrication. Laser micro-fabrication allows the fabrication of 3-D geometries. The drawback is that such a technique is a linear process where the cost depends on the laser time, and this may not be very cost-efficient for large arrays. The photolithographic technique allows instead the fabrication of arrays of antennas on a single wafer and in parallel by reflowing a photoresist material and then etching the silicon.

Two antenna prototypes were fabricated using these fabrication techniques. The radiation pattern of these antennas was measured and compared to the simulated ones. Very accurate profiles can be achieved with laser micro-machining processes, as it could be observed in the agreement in the radiation pattern measured of the antenna prototype fabricated. On the other hand, the agreement achieved between the measured and the simulated radiation pattern of the prototype fabricated with photolithographic processes is not so good due to the difference in surface between the fabricated and the measured lens. However, it still provided a focused beam with good aperture efficiency. A study of the aberrations of the lens was developed in order to evaluate the performance of the lens profile.

All in all, future FPAs should consider the use of these lens antennas fabricated with photolithographic processes which allows the fabrication of a high number of lenses in a single process. If high uniformity is needed in the array, one could consider the integration of the lens aberration study in the fabrication process for further optimization.

7.2 Future Research Lines

Several research lines can be thought as a continuation of the work developed during this doctoral thesis that make use of some or several of the conclusions drawn from it.

The design methodology developed for the near field imaging system based on MST could be extended to other types of systems such as the development of heterodyne receivers. Heterodyne receivers at millimeter and submillimeter-wave frequencies commonly employ planar antennas where, for example, a Schottky diode is placed on top of the antenna to mix the THz signal and convert it to a lower frequency. The diode characterization and matching techniques employed in this thesis can be oriented to its use for the heterodyne receiver.

The Complementary Metal Oxide Semiconductor (CMOS) technology, which is pushing up in frequency (at the moment is working at around 400 GHz), becomes a very interesting potential technology that can now be considered in submillimeter wave band. This technology would allow the fabrication of compact, cost-effective terahertz transceivers by integrating the antenna within the whole transceiver electronics. The micro-lens antenna presented in this thesis could be an excellent candidate of antenna that could be used for this type of systems for its integration capabilities and the high performances demonstrated.

The use of the advanced fabrication processes, i.e the silicon micro-fabrication processes, can be extended to design other new antenna geometries. For instance, this pho-

tolithographic technology has been employed in the fabrication of low degree angle walls that could be employed in the fabrication of directive horns. It consists of stacking gold plated silicon wafers with tapered holes. This technique is still in an early stage of development and an improvement in this angle controllability is required.

Finally, the systems presented in this thesis could be employed at higher frequencies. A retina working at 600 GHz using Schottky diodes could be developed with the same guidelines as explained in this thesis. The micro-lens antenna presented can be also scaled to a higher frequency. In fact, a prototype at 2 THz is currently being fabricated and pending to be measured, which opens up the possibilities to design other systems based on this antenna for radio-astronomy applications.

A

Appendix A
Antenna Prototype at 300 GHz

This section presents the prototype fabrication of the antenna previously designed. The antenna is intended to be patterned on a substrate of 150 μm of quartz wafer of 50.8 mm of diameter. A gold metallization of 0.5 μm of gold deposited by evaporation on each side of the wafer. The patterning of the wafer will is performed with lithographic processes which have a precision of 1 μm.

For this prototype, the goal was to perform a set of measurements of one antenna in order to analyze the performance and characterize both, the antenna and the diode. Figure A.1 shows the final antenna prototype state of the art that is intended to be fabricated. As it was required in the previous design at 100 GHz, a special waveguide adapter is needed in order to allocate the antenna within the two waveguides working as a collector and illuminator. Two WR-3.4 waveguides are used containing a standard UG-387 flange. One of the waveguide faces contains the pattern of the profile of the retina and in another face of the other waveguide contains the pattern of the filter and an extra cavity. Note that in this case, the overall space of the retina was minimized so the bias pad could not be outside the waveguide flange, therefore, an extra cavity was profiled in the waveguide face in order to allocate the biasing contact pad preventing the short-circuit.

The mask distribution of the retina within the quartz wafer is shown in Figure A.2. Eight individual antenna prototypes were placed in the top part of the wafer which are enough in order to provide duplicity in case of mistakes. The bottom part of the wafer contains a prototype of retina at 100 GHz that was intended to be used for other measurements. Besides the prototypes, different marks were distributed around the mask. First, different sets of alignment masks in order to provide the alignment between the top

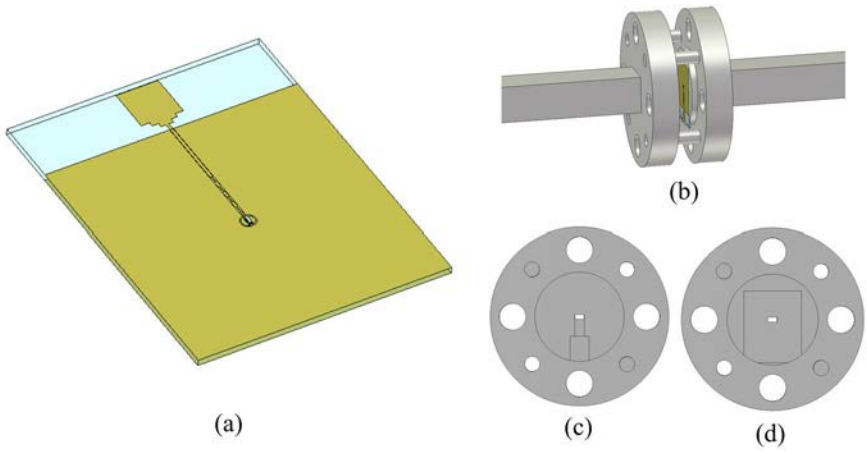

Figure A.1: (a) One element antenna prototype. (b),(c),(d) Different views of the designed adapter that holds the prototype.

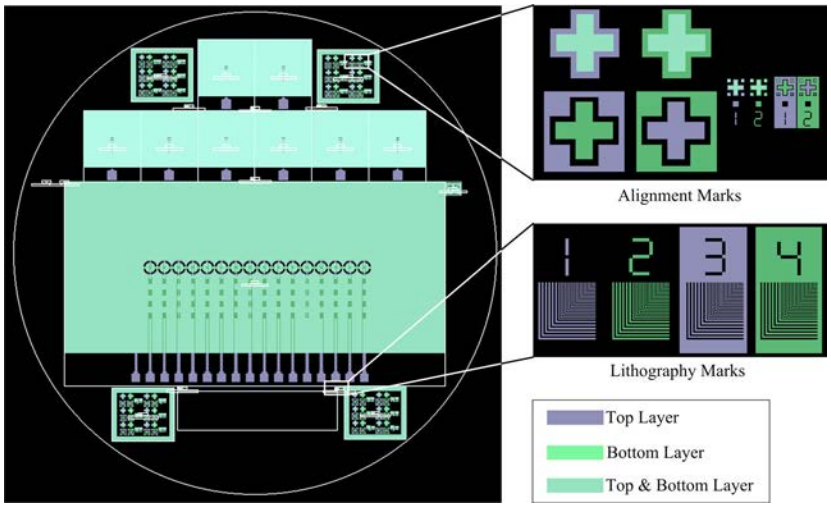

Figure A.2: Mask set distribution containing the design of the prototypes.

layer and the bottom layer. Last, lithography marks that would help to see the etching quality of the fabrication process.

In the first place, the fabrication was intended to be in the cleanroom facility of the UPC, however, due to the lack of capabilities to provide the top-bottom layer alignment the possibility was discarded. Another facility in Chalmers University was considered, still, due to budgetary restrictions this option was also dismissed.

B

Appendix B
Lens Analysis

B.1 Physical Optics - Secondary Field Calculation

A PO Analysis has been used to perform the study and optimization of the micro-lens presented in this thesis. The PO Analysis is a method that provides an approximation to the surface currents J_s and M_s over a lens large in terms of the wavelength [74, 75]. By integrating these currents, the radiated field also known as secondary patterns of the lens antenna can be obtained.

Using Love's Equivalence Principle [76, 77], the transmitted fields of the lens can be used to determine the equivalent magnetic and electric sheet currents on the outside of the lens surface (see Figure B.1):

$$\begin{aligned} \vec{J}_s &= \hat{n} \times \vec{H}^t \\ \vec{M}_s &= -\hat{n} \times \vec{E}^t \end{aligned} \tag{B.1}$$

where $\hat{n}$ is the normal vector to the surface and E^t and H^t are the radiated fields from

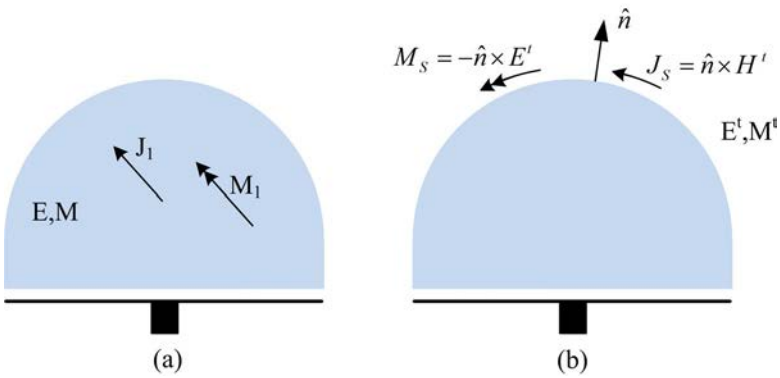

Figure B.1: Love's Equivalence Principle scheme. (a) Actual problem (b) Equivalent problem.

the antenna feed transferred outside the dielectric boundary of the lens.

In order to determine the transmitted fields to the hemispherical surface fields a ray optics procedure is used. The PO supposes that these currents can be approximated directly by the incident field $\vec{E}$. Thus, the incident field is decomposed in their parallel and perpendicular components to the plane of incidence and multiplied by its appropriate Fresnel transmission coefficient:

$$\begin{aligned} \vec{E}^t_{||} &= E_{||}\tau_{||}\hat{\imath}^t_{||} \\ \vec{E}^t_{\perp} &= E_{\perp}\tau_{\perp}\hat{\imath}_{\perp} \end{aligned} \tag{B.2}$$

being the total field $\vec{E}^t = \vec{E}^t_{||} + \vec{E}^t_{\perp}$. The magnetic field can be calculated as $\vec{H}^t = i^t_r \times \vec{E}^t/\zeta$. This incident field is calculated using the field obtained by the antenna feed and assuming a plane wave coming from the center of the antenna feed to each point of the lens. The Fresnel transmission coefficients are defined as:

$$\begin{aligned} \tau_{||} &= \frac{2\sqrt{\epsilon_r}\cos\theta_i}{\cos\theta_i + \sqrt{\epsilon_r}\cos\theta_t} \\ \tau_{\perp} &= \frac{2\sqrt{\epsilon_r}\cos\theta_i}{\cos\theta_t + \sqrt{\epsilon_r}\cos\theta_i} \end{aligned} \tag{B.3}$$

being ϵ_r the micro-lens dielectric, θ_i the angle of incidence and θ_t the angle of transmission. And the propagation vectors are defined as:

$$\begin{aligned} \hat{\imath}^t_r &= \hat{\imath}_{r'}\sqrt{\epsilon_r} + \hat{\imath}_r\sqrt{\epsilon_r}\cos\theta_i\sqrt{1 + \frac{1-\epsilon_r}{\epsilon_r\cos^2\theta_i}} \\ \hat{\imath}^t_{||} &= \hat{\imath}_{\perp} \times \hat{\imath}^t_r \end{aligned} \tag{B.4}$$

Note that the perpendicular and parallel electric components are defined (with respect to this normal vector) as: $\hat{\imath}_{\perp} = \hat{\imath}_r \times \hat{\imath}_{r'}$ and $\hat{\imath}_{||} = \hat{\imath}_{\perp} \times \hat{\imath}_{r'}$ respectively. The propagation vector of the incident field is $\hat{\imath}_{r'} = \hat{\imath}_x \sin\theta'\cos\phi' + \hat{\imath}_y \sin\theta'\sin\phi' + \hat{\imath}_z\cos\theta'$. Then, the normal vector to the hemisphere surface is:

$$\hat{n} = \hat{\imath}_r = \hat{\imath}_x \sin\theta\cos\phi + \hat{\imath}_y \sin\theta\sin\phi + \hat{\imath}_z\cos\theta \tag{B.5}$$

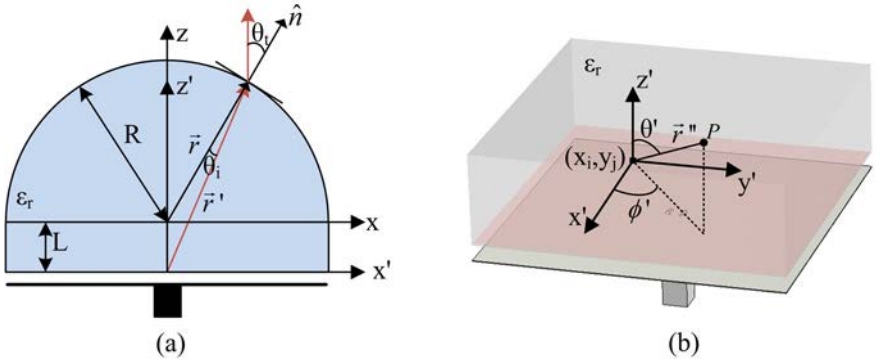

Figure B.2: (a) Scheme of the micro-lens antenna with the different coordinated systems. (b) Scheme of the antenna feed simulated in CST, the red plane represents the aperture grid.

Finally, from the currents in equation B.1, the far fields patterns of the micro-lens antenna are then determined by integrating over the lens surface:

$$\vec{E}_\theta = -\jmath\frac{ke^{-jkr^t}}{4\pi r^t}\int\int_S (M_s^\phi + \zeta J_s^\theta)e^{jkR\cos\varphi}dS$$
$$\vec{E}_\phi = \jmath\frac{ke^{-jkr^t}}{4\pi r^t}\int\int_S (M_s^\theta - \zeta J_s^\phi)e^{jkR\cos\varphi}dS \tag{B.6}$$

where R is the radius of the lens sphere, $\vec{M}_s = M_s^\theta\hat{\imath}_\theta + M_s^\phi\hat{\imath}_\phi$, $J_s = J_s^\theta\hat{\imath}_\theta + J_s^\phi\hat{\imath}_\phi$, $dS = R^2\sin\theta d\theta d\phi$ and $\cos\varphi = \hat{\imath}_r\cdot\hat{\imath}_r^t$.

B.2 Primary Field Calculation

The PO technique described uses as an input the primary field of the antenna feed, which is the incident field radiated by the antenna feed within the lens inner surface. In this thesis, the antenna feed fields have been obtained by simulating the antenna feed 3-D structure with CST. In Figure B.2b the simulated structure is shown. The infinite silicon medium is achieved by setting absorbing boundaries in the model. The aperture field is obtained over the $x'y'$ and $z' = 0$ grid (this plane is marked in red in Figure B.2b) which will allow to compute the currents using the free space green's function thanks to the use of the equivalence principle [76, 77].

The magnetic current $\vec{M}_a$ are calculated using Equation B.1 using $\hat{n} = \hat{\imath}_z$ and the field obtained from CST. Then, the magnetic field can be calculated at any point by using the Green function, thus, it can be expressed as:

$$\vec{H}(\vec{r}) = \int\int_S \bar{\bar{g}}^{hm}(\vec{r},\vec{r}\,') * \vec{M}_a(\vec{r}\,')d\vec{r}\,' \tag{B.7}$$

being $\bar{\bar{g}}^{hm}(\vec{r},\vec{r}\,')$ the spacial green function defined as:

$$\bar{\bar{g}}^{\,hm}(\vec{r},\vec{r}\,') = -j\frac{1}{\zeta k}\begin{bmatrix} k^2+\frac{\delta^2}{\delta x^2} & \frac{\delta^2}{\delta x\delta y} & \frac{\delta^2}{\delta x\delta z} \\ \frac{\delta^2}{\delta y\delta x} & k^2+\frac{\delta^2}{\delta y^2} & \frac{\delta^2}{\delta y\delta z} \\ \frac{\delta^2}{\delta z\delta x} & \frac{\delta^2}{\delta z\delta y} & k^2+\frac{\delta^2}{\delta z^2} \end{bmatrix}\frac{e^{-jk|\vec{r}-\vec{r}\,'|}}{4\pi|\vec{r}-\vec{r}\,'|} \tag{B.8}$$

The same could be done for the electric field using $\bar{\bar{g}}^{em}(\vec{r},\vec{r}\,')$

An important consideration to take into account is the fact that the lens can be in the near-field or the far-field of the antenna feed, because it will cause a variation in the amplitude and the phase of the resulting illumination. In the case of the far-field, the magnetic field can be obtained by [48]:

$$\vec{H} = jk\cos\theta\widetilde{G}^{hm}(k\sin\theta\cos\phi, k\sin\theta\sin\phi)\widetilde{M}_a(k\sin\theta\cos\phi, k\sin\theta\sin\phi)\frac{e^{-jkr}}{2\pi r} \tag{B.9}$$

where $\widetilde{M}_a(k\sin\theta\cos\phi, k\sin\theta\sin\phi)$ is the Fourier Transform of the magnetic current distribution in the aperture $\vec{M}_a$ and $\widetilde{G}^{hm}(k\sin\theta\cos\phi, k\sin\theta\sin\phi)$ is the spectral Green's function for a magnetic current defined as:

$$\widetilde{G}^{hm} = -\frac{1}{k\zeta}\frac{1}{8\pi^2}\frac{1}{k_z}\begin{bmatrix} k^2-k_x^2 & -k_xk_y & -k_xk_z \\ -k_xk_y & k^2-k_y^2 & -k_yk_z \\ -k_xk_z & -k_yk_z & k^2-k_z^2 \end{bmatrix} \tag{B.10}$$

being $k_x = k\sin\theta\cos\phi$ and $k_y = k\sin\theta\sin\phi$. Note that the reference system x, y, z is placed in the center of the hemisphere and the x', y', z' is associated with the antenna feed (see Figure B.2b). The relationship between them is $x = x'$, $y = y'$ and $z = z' - L$. Further details of this development can be found in [48].

Due to the fact that this thesis is using leaky wave antenna feeds which achieve high directivity, the lens will be in most of cases in the near-field. Moreover, in this case the lens is placed in the radiative region of the near-field (not in the reactive near-field) and therefore the PO can still be used. Therefore, the field from the antenna feed can still be represented by plane waves with an angular distribution that depends on the distance. Thus, the primary fields over the near field will be calculated using a pre-tabulation of the Green's function in the space domain and the component r of the field will be ignored. In the radiative region, the calculation of Equation B.9 can be simplified assuming that each infinitesimal contribution of the integral is in the far-field. Therefore, Equation B.9 can be expressed as [78]:

$$\vec{H} = \sum_i\sum_j jk\cos\theta'\widetilde{G}^{hm}(k\sin\theta'\cos\phi', k\sin\theta'\sin\phi')\frac{e^{-jk|\vec{r}\,'-\vec{r}\,''|}}{2\pi|\vec{r}\,'-\vec{r}\,''|}\vec{m}_a(x_i,y_j)\Delta x_i\Delta y_j \tag{B.11}$$

Note that in this case the reference system is centered at each point of the aperture, then the summation of the field components is performed in x, y, z before switching to θ and ϕ.

All in all, the far field can be calculated once independently of the geometry of the lens, as the dependency in r is eliminated (i.e e^{-jkr}/r)and it is added later when the equivalent currents are computed over the lens. On the other hand, the near-field is required to be calculated for each lens geometry.

C

Appendix C

Effect of Lens Surface Distortions on the Radiated Field of a Micro-lens Antenna

The micro-lens surface fabricated with a photolithographic process did not achieve a surface totally spherical. These distortions of the surface cause variations in the radiated fields of the antenna which can be quantified and calculated by assuming that the physical aberration is proportional to a phase distortion on the field. In this Appendix the analysis followed in this thesis is explained in detail.

First, the analysis begins by defining the surface to evaluate; it is defined as the difference between the fabricated lens profile and the sphere profile that best fits the fabricated lens. This surface is decomposed in a Zernike polynomial expansion. Zernike polynomials are employed in optics to describe the physical distortion of lenses and reflectors [75, 79]. Zernike polynomials form a complete set of functions or modes that are orthogonal over a

Zernike Polynomial Modes

j	n	m	$Z_n^m(\rho,\phi)$	Aberration Name
1	0	0	1	Constant term
2	1	1	$2\rho\cos\phi$	Tilt in x-direction.
3	1	-1	$2\rho\sin\phi$	Tilt in y-direction.
4	2	0	$\sqrt{3}(2\rho^2-1)$	Defocus (longitudinal position)
5	2	-2	$\sqrt{6}\rho^2\sin 2\phi$	Astigmatism
6	2	2	$\sqrt{6}\rho^2\cos 2\phi$	Astigmatism
7	3	-1	$\sqrt{8}(3\rho^3-2\rho)\sin\phi$	Coma
8	3	1	$\sqrt{8}(3\rho^3-2\rho)\cos\phi$	Coma
9	3	-3	$\sqrt{8}\rho^3\sin 3\phi$	-
10	3	3	$\sqrt{8}\rho^3\cos 3\phi$	-
11	4	0	$\sqrt{5}(6\rho^4-6\rho^2+1)$	Spherical aberration
12	4	2	$\sqrt{10}(4\rho^4-3\rho^2)\cos 2\phi$	Astigmatism 2nd order
13	4	-2	$\sqrt{10}(4\rho^4-3\rho^2)\sin 2\phi$	Astigmatism 2nd order
14	4	4	$\sqrt{10}\rho^4\cos 4\phi$	-
15	4	-4	$\sqrt{10}\rho^4\sin 4\phi$	-

Table C.1: Zernike polynomials expansion.

circle of unit radius and are convenient for serving as a set of basis functions. This makes them suitable for accurately describing wave aberrations as well as for data fitting. They are in general a complex valued function; however, for this study only the real parts are considered. They can be written as:

$$Z_n^m(\rho,\phi) = R_n^m(\rho)\cos(m\phi) \tag{C.1}$$

where m and n are positive integers with $n \geq m$, ϕ is the azimuthal angle and ρ is the radial distance $0 \leq \rho \leq 1$. Note that $|Z_n^m(\rho,\phi)| \leq 1$. And the radial polynomial $R_n^m(\rho)$ is defined as:

$$R_n^m(\rho) = \sum_{k=0}^{(n-m)/2} \frac{(-1)^k(n-k)!}{k!((n+m)/2-k)!((n-m)/2-k)!}\rho^{n-2k} \tag{C.2}$$

The first few Zernike modes, ordered by Noll index j are described in table C.1. 3-D plots of some of the Zernike polynomials are shown in Figure C.1.

The Zernike polynomial expansion of a surface is an efficient technique to describe its distortion. The aberration function Φ can be expressed in terms of the Zernike polynomials as:

$$\Phi(\rho,\phi) = \sum_{n,m} \alpha_n^m R_n^m(\rho)\cos(m\phi) \tag{C.3}$$

for $0 \leq \rho \leq 1$ and $0 \leq \phi \leq 2\pi$ and being α_n^m the Zernike coefficient of the polynomial (n,m). In the case of the surface evaluated from the fabricated lens, 190 Zernike polynomials have been used to expand the surface. The Zernike coefficients were calculated using least squares estimation. The decomposition of the Zernike polynomials is shown in Table C.2. Note that the polynomials are sorted by the coefficient α_n^m which will be equivalent to the percentage of contribution of each polynomial.

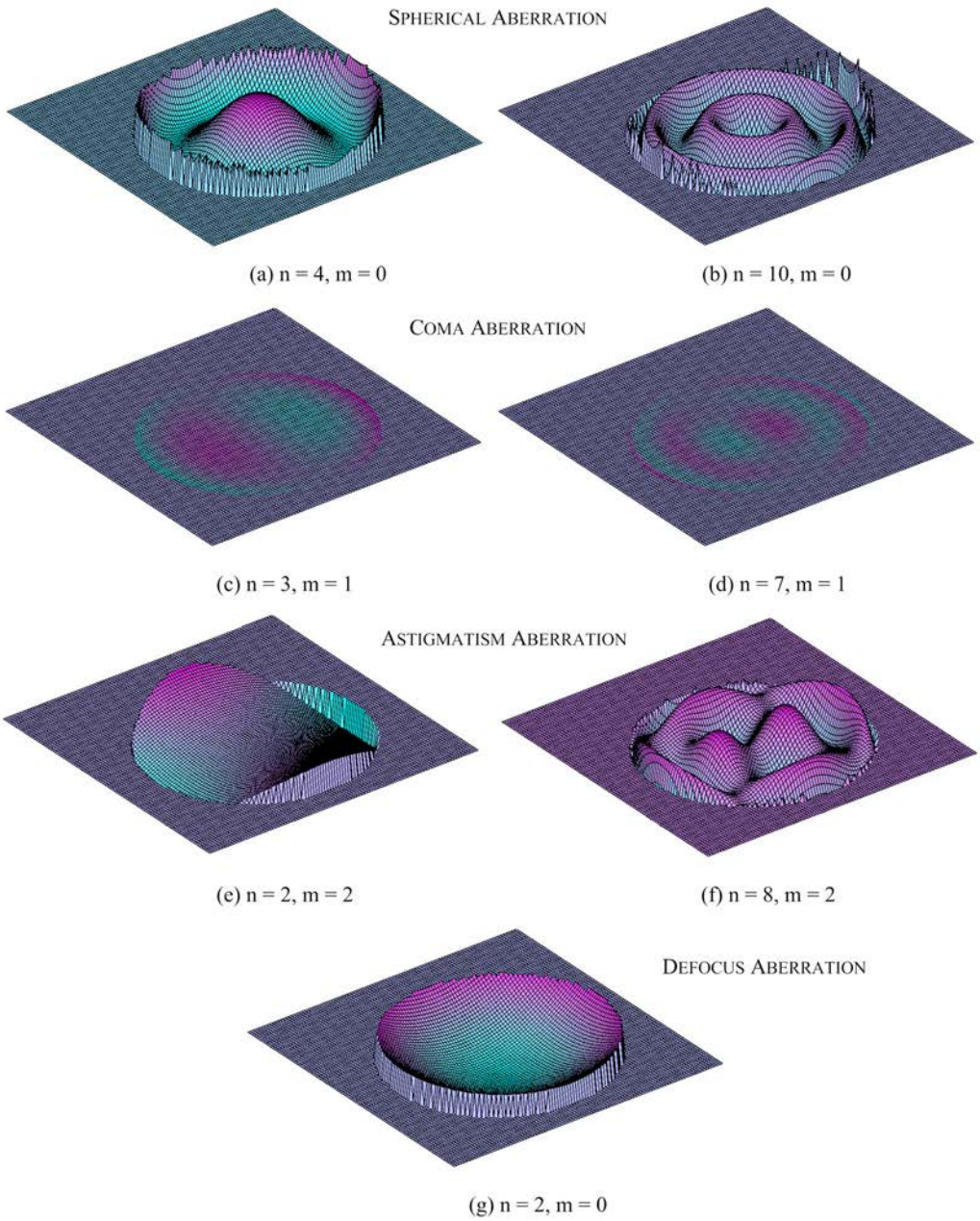

Figure C.1: 3-D surface representation of the Zernike polynomials.

This aberration function indicates the displacement of the surface in the z-axis in the aperture plane of the lens. The aperture plane of the lens is defined as the plane in the xy-axis and $z = 0$ as shown in Figure C.2a. Thus, this displacement is translated into a phase variation (using e^{jkz} being z the former displacement) which is multiplied to

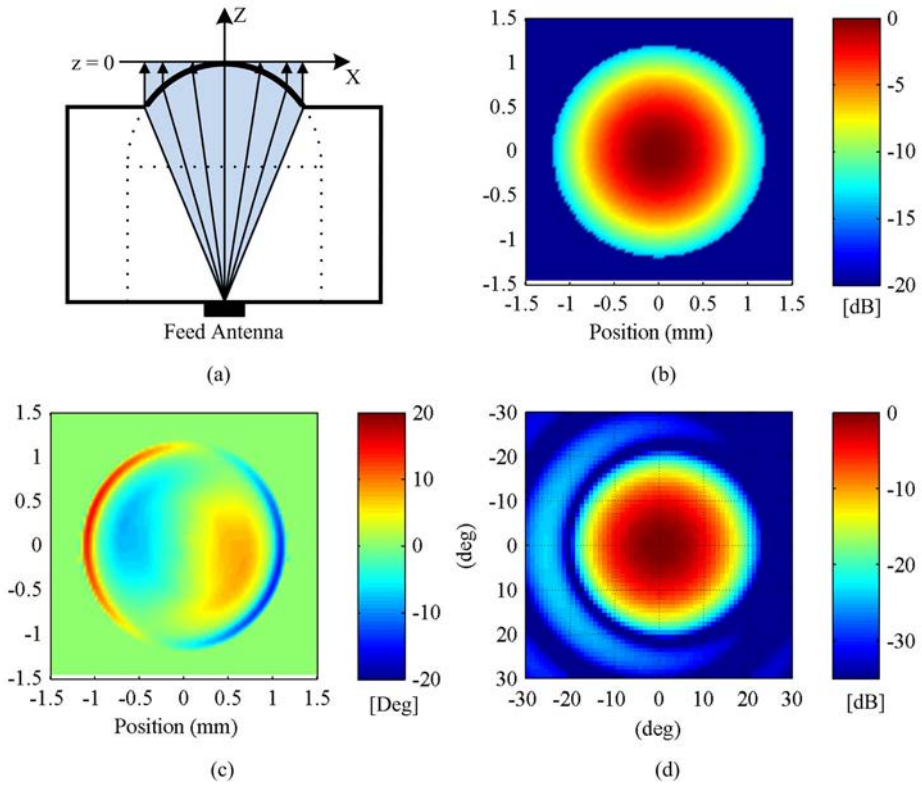

Figure C.2: (a) Scheme of the micro-lens illumination in the aperture plane. (c) Coma aberration translated to a phase variation. (d) 2-D radiation pattern of the micro-lens antenna considering the coma aberration.

the field distribution at the aperture plane ($g(\rho, \phi)$). Then, the radiation pattern can be obtained by calculating the FFT of this resulting field distribution:

$$f(\theta, \phi) = \mathcal{F}\{g(\rho, \phi)e^{jk\Phi(\rho,\phi)}\} \tag{C.4}$$

An example is presented in Figure C.2b,c,d, where a Gaussian field distribution of taper -14 dB is used as an illumination of a lens suffering from a coma aberration (see Figure C.1c). This coma aberration displacement is converted to a phase variation plane which is shown in Figure C.2c. The radiation pattern of the micro-lens antenna is shown in Figure C.2d using the FFT of the combination of the gaussian field distribution plane (Figure C.2b) and the phase variation plane (Figure C.2c).

Zernike Polynomial Expansion

#	n	m	α_n^m	#	n	m	α_n^m	#	n	m	α_n^m	#	n	m	α_n^m
1	4	0	6.5279	49	18	-4	0.5359	97	17	-13	0.2159	145	16	14	0.0913
2	8	0	4.8599	50	13	-3	0.5345	98	20	-6	0.2130	146	15	-13	0.0896
3	3	1	4.7747	51	7	-5	0.5295	99	15	9	0.2083	147	18	12	0.0879
4	10	0	4.2581	52	17	5	0.5199	100	20	-10	0.2071	148	12	-2	0.0860
5	6	0	3.4142	53	16	4	0.4903	101	17	3	0.2061	149	20	-16	0.0848
6	7	1	3.0651	54	13	9	0.4864	102	10	8	0.2039	150	16	8	0.0838
7	9	1	2.5627	55	12	6	0.4767	103	11	9	0.2032	151	13	-5	0.0821
8	12	0	2.1790	56	13	-11	0.4646	104	17	-11	0.2025	152	16	12	0.0817
9	2	0	2.1738	57	15	-1	0.4616	105	20	18	0.2008	153	17	9	0.0794
10	7	-3	1.7225	58	12	4	0.4424	106	16	2	0.2007	154	18	4	0.0754
11	15	1	1.6701	59	11	7	0.4226	107	18	8	0.1969	155	15	7	0.0749
12	8	2	1.6523	60	16	-6	0.4212	108	15	-7	0.1957	156	20	-2	0.0736
13	17	1	1.6439	61	12	-10	0.4183	109	16	6	0.1939	157	16	-10	0.0731
14	18	0	1.5865	62	19	17	0.4095	110	14	-8	0.1932	158	14	8	0.0724
15	7	-1	1.4180	63	9	7	0.4065	111	14	6	0.1925	159	14	0	0.0723
16	5	3	1.3978	64	18	-6	0.4012	112	11	-9	0.1908	160	13	7	0.0720
17	5	1	1.3891	65	20	2	0.3908	113	20	-4	0.1862	161	19	-9	0.0718
18	8	-4	1.3738	66	18	-8	0.3863	114	18	-10	0.1841	162	12	-4	0.0698
19	20	0	1.2915	67	15	3	0.3852	115	10	-2	0.1734	163	18	-2	0.0694
20	7	5	1.2601	68	14	2	0.3616	116	17	13	0.1726	164	15	-9	0.0680
21	9	5	1.2434	69	12	8	0.3536	117	13	5	0.1705	165	4	2	0.0656
22	16	0	1.2340	70	14	-10	0.3526	118	20	-12	0.1673	166	13	-7	0.0577
23	6	-4	1.2268	71	17	-5	0.3519	119	6	-2	0.1615	167	16	-12	0.0569
24	6	2	1.2139	72	17	-15	0.3361	120	14	-12	0.1614	168	14	-2	0.0506
25	3	-1	1.1823	73	12	2	0.3326	121	8	4	0.1589	169	18	10	0.0492
26	19	1	0.9798	74	13	3	0.3306	122	11	-7	0.1548	170	19	13	0.0478
27	8	-6	0.9613	75	12	-6	0.3277	123	11	-3	0.1495	171	19	-13	0.0477
28	11	1	0.9224	76	15	-11	0.3264	124	14	12	0.1493	172	18	14	0.0449
29	10	-6	0.8234	77	16	-14	0.3109	125	16	-8	0.1446	173	19	-1	0.0434
30	10	2	0.8015	78	17	-9	0.3073	126	19	-3	0.1417	174	18	6	0.0404
31	9	-1	0.7883	79	18	2	0.3052	127	19	-11	0.1393	175	11	-5	0.0368
32	10	-4	0.7863	80	6	4	0.3042	128	15	-5	0.1390	176	16	-2	0.0367
33	9	-3	0.7711	81	9	3	0.3002	129	20	12	0.1373	177	20	14	0.0350
34	10	-8	0.7516	82	20	-8	0.2977	130	19	15	0.1361	178	10	4	0.0329
35	16	-4	0.7376	83	19	5	0.2959	131	5	-1	0.1345	179	11	3	0.0324
36	17	-3	0.7244	84	4	-2	0.2929	132	19	-5	0.1342	180	19	11	0.0303
37	14	4	0.7121	85	20	8	0.2874	133	18	-14	0.1308	181	20	10	0.0289
38	13	1	0.6882	86	20	-18	0.2854	134	17	15	0.1305	182	18	-12	0.0241
39	5	-3	0.6806	87	20	4	0.2715	135	13	11	0.1277	183	19	-17	0.0231
40	15	-3	0.6779	88	14	-6	0.2682	136	18	16	0.1160	184	19	3	0.0198
41	12	-8	0.6503	89	13	-1	0.2651	137	14	10	0.1146	185	17	-7	0.0159
42	15	5	0.6025	90	17	7	0.2509	138	20	16	0.1141	186	17	11	0.0143
43	7	3	0.5997	91	12	10	0.2477	139	8	-2	0.1127	187	15	11	0.0110
44	9	-5	0.5973	92	15	13	0.2307	140	16	10	0.1088	188	9	-7	0.0103
45	14	-4	0.5784	93	19	7	0.2297	141	19	-7	0.1022	189	20	6	0.0067
46	17	-1	0.5732	94	18	-16	0.2276	142	13	-9	0.1013	190	19	-15	0.0058
47	11	5	0.5436	95	19	9	0.2244	143	11	-1	0.1013				
48	10	6	0.5401	96	8	6	0.2219	144	20	-14	0.0969				

Table C.2: Zernike polynomial expansion of the error surface.

List of Acronyms

CMOS Complementary Metal Oxide Semiconductor

CNC Computer Numerical Control

CNF Cornell Nanoscale Science and Technology Facilities

CNM National Microelectronics Centre

DRIE Deep Reactive Ion Etching

EBG Electromagnetic Band Gap

FFT Fast Fourier Transform

FPA Focal Plane Array

HEB Hot Electron Bolometer

ITMA Instituto Tecnologico de Materiales

KID Kinetic Inductance Detector

ME Modulation Efficiency

MIC Monolithic Integrated Circuits

MIC Monolithic Microwave Integrated Circuits

MST Modulated Scatterer Technique

PCB Printed Circuit Board

PEC Perfect Electric Conductor

PIC Programmable Integrated Circuit

PMMA Poly-Methyl Methacrystalate

PO Physical Optics

QCL Quantum Cascade Laser

RF-MEMS Radio-Frequency Microelectromechanical Systems

RIE Reactive Ion Etching

RMS Root Mean Square

SEM Scanning Electron Microscope

SIS Superconductor Insulator Superconductor

SNR Signal to Noise Ratio

SOI Silicon on Insulator

UAB Universitat Autonoma de Barcelona

UPC Universitat Politecnica de Catalunya

USB Universal Serial Bus

USU Utah State University

VNA Vector Network Analyzer

List of Figures

List of Tables

Bibliography

[1] P. H. Siegel, "Terahertz technology," *IEEE Transactions on Microwave Theory and Techniques*, vol. 50, no. 3, pp. 910–928, 2002. [Online]. Available: http://ieeexplore.ieee.org/stamp/stamp.jsp?arnumber=989974 1

[2] M. Tonouchi, "Cutting-edge terahertz technology," *Nature photonics*, vol. 1, no. 2, pp. 97–105, 2007. [Online]. Available: http://www.nature.com/nphoton/journal/v1/n2/abs/nphoton.2007.3.html 1

[3] H.-B. Liu, H. Zhong, N. Karpowicz, Y. Chen, and X.-C. Zhang, "Terahertz spectroscopy and imaging for defense and security applications," *Proceedings of the IEEE*, vol. 95, no. 8, pp. 1514–1527, 2007. [Online]. Available: http://ieeexplore.ieee.org/stamp/stamp.jsp?arnumber=4337845 2

[4] P. H. Siegel, "Terahertz technology in biology and medicine," *IEEE Transactions on Microwave Theory and Techniques*, vol. 52, no. 10, pp. 2438–2447, 2004. [Online]. Available: http://ieeexplore.ieee.org/stamp/stamp.jsp?arnumber=1341664 2

[5] ——, "THz applications for outer and inner space," in *Electromagnetic Compatibility, 2006. EMC-Zurich 2006. 17th International Zurich Symposium on*, 2006, pp. 1–4. [Online]. Available: http://ieeexplore.ieee.org/stamp/stamp.jsp?arnumber=1629544 2

[6] Lee, B. S. Williams, S. Kumar, Q. Hu, and J. L. Reno, "Real-time imaging using a 4.3-THz quantum cascade laser and a 320 × 240 microbolometer focal-plane array," *IEEE Photonics Technology Letters*, vol. 18, no. 13, pp. 1415–1417, 2006. 2

[7] N. Karpowicz, H. Zhong, J. Xu, K.-I. Lin, J.-S. Hwang, and X.-C. Zhang, "Non-destructive sub-thz cw imaging," pp. 132–142, 2005. [Online]. Available: +http://dx.doi.org/10.1117/12.590539 2

[8] P. Day, H. Leduc, A. Goldin, T. Vayonakis, B. Mazin, S. Kumar, J. Gao, and J. Zmuidzinas, "Antenna-coupled microwave kinetic inductance detectors," *Nuclear Instruments and Methods in Physics Research Section A: Accelerators, Spectrometers, Detectors and Associated Equipment*, vol. 559, no. 2, pp. 561 – 563, 2006. [Online]. Available: http://www.sciencedirect.com/science/article/pii/S0168900205024824 2

[9] Mehdi, G. Chattopadhyay, E. Schlecht, J. Ward, J. Gill, F. Maiwald, and A. Maestrini, "Terahertz multiplier circuits," in *Microwave Symposium Digest, 2006. IEEE MTT-S International*, 2006, pp. 341–344. [Online]. Available: http://ieeexplore.ieee.org/stamp/stamp.jsp?arnumber=4014898 2

[10] Vassilev, D. Henke, I. Lapkin, O. Nystrom, R. Monje, A. Pavolotsky, and V. Belitsky, "Design and characterization of a 211–275 GHz sideband separating mixer for the apex telescope," *IEEE Microwave and Wireless Components Letters*, vol. 18, no. 1, pp. 58–60, 2008. [Online]. Available: http://ieeexplore.ieee.org/stamp/stamp.jsp?arnumber=4408590 2

[11] Semenov, H.-W. Hubers, H. Richter, M. Birk, M. Krocka, U. Mair, Y. B. Vachtomin, M. I. Finkel, S. V. Antipov, B. M. Voronov, K. V. Smirnov, N. S. Kaurova, V. N. Drakinski, and G. N. Gol'tsman, "Superconducting hot-electron bolometer mixer for terahertz heterodyne receivers," *IEEE Transactions on Applied Superconductivity*, vol. 13, no. 2, pp. 168–171, 2003. [Online]. Available: http://ieeexplore.ieee.org/stamp/stamp.jsp?arnumber=1211568 2

[12] P. H. Siegel, P. de Maagt, and A. I. Zaghloul, "Antennas for terahertz applications," in *Antennas and Propagation Society International Symposium 2006, IEEE*, 2006, pp. 2383–2386. [Online]. Available: http://ieeexplore.ieee.org/stamp/stamp.jsp?arnumber=1711074 3

[13] J.-C. Bolomey, B. J. Cown, G. Fine, L. Jofre, M. Mostafavi, D. Picard, J. P. Estrada, P. G. Friederich, and F. L. Cain, "Rapid near-field antenna testing via arrays of modulated scattering probes," *IEEE Transactions on Antennas and Propagation*, vol. 36, no. 6, pp. 804–814, 1988. 3

[14] M. A. Abou-Khousa, M. T. Ghasr, S. Kharkovsky, D. Pommerenke, and R. Zoughi, "Modulated elliptical slot antenna for electric field mapping and microwave imaging," *IEEE Transactions on Antennas and Propagation*, vol. 59, no. 3, pp. 733–741, 2011. 3

[15] K. Cooper, R. J. Dengler, N. Llombart, B. Thomas, G. Chattopadhyay, and P. H. Siegel, "THz imaging radar for standoff personnel screening," *IEEE Transactions on Terahertz Science and Technology*, vol. 1, no. 1, pp. 169–182, 2011. [Online]. Available: http://ieeexplore.ieee.org/stamp/stamp.jsp?arnumber=6005328 3, 67, 77, 94

[16] A. Moussessian, M. C. Wanke, Y. Li, J.-C. Chiao, S. J. Allen, T. W. Crowe, and D. B. Rutledge, "A terahertz grid frequency doubler," *IEEE Transactions on Microwave Theory and Techniques*, vol. 46, no. 11, pp. 1976–1981, 1998. [Online]. Available: http://ieeexplore.ieee.org/stamp/stamp.jsp?arnumber=734524 4, 131

[17] C.-Y. Chi and G. M. Rebeiz, "A quasi-optical amplifier," *IEEE Microwave and Guided Wave Letters*, vol. 3, no. 6, pp. 164–166, 1993. [Online]. Available: http://ieeexplore.ieee.org/stamp/stamp.jsp?arnumber=219802 4

[18] D. Rutledge, M. Kim, E. Sovero, M. De Lisio, J. Hacker, J.-C. Chiao, S.-J. Li, D. Gagnon, and J. Rosenberg, "Performance and applications of a 1-element hbt grid amplifier," in *Microwave Conference Proceedings, 1993. APMC '93., 1993 Asia-Pacific*, vol. 1, 1993, pp. 1–38–1–41 vol.1. 4

[19] P. Arcioni, M. Bozzi, G. Conciauro, and L. Perregrini, "Design and optimization of quasioptical frequency multipliers," *International Journal of Infrared and Millimeter Waves*, vol. 20, no. 5, pp. 913–928, 1999. [Online]. Available: http://dx.doi.org/10.1023/A%3A1021778318847 4

[20] G. Chattopadhyay, C.-L. Kuo, P. Day, J. J. Bock, J. Zmuidzinas, and A. E. Lange, "Planar antenna arrays for cmb polarization detection," in *Infrared and Millimeter Waves, 2007 and the 2007 15th International Conference on Terahertz Electronics. IRMMW-THz. Joint 32nd International Conference on*, 2007, pp. 184–185. [Online]. Available: http://ieeexplore.ieee.org/stamp/stamp.jsp?arnumber=4516451 5, 131

[21] M. M. Kangas, M. Ansmann, B. Horgan, N. Lemaster, R. Leonardi, A. Levy, P. Lubin, J. Marvil, P. McCreary, and T. Villela, "A 31 pixel flared 100-GHz high-gain scalar corrugated nonbonded platelet antenna array," *IEEE Antennas and Wireless Propagation Letters*, vol. 4, pp. 245–248, 2005. [Online]. Available: http://ieeexplore.ieee.org/stamp/stamp.jsp?arnumber=1492381 6, 131

[22] J. Leech, B. K. Tan, G. Yassin, P. Kittara, S. Wangsuya, J. Treuttel, M. Henry, M. L. Oldfield, and P. G. Huggard, "Multiple flare-angle horn feeds for sub-mm astronomy and cosmic microwave background experiments," *Astronomy & Astrophysics*, vol. 532, p. A61, Aug. 2011. 6, 131

[23] V. M. Lubecke, K. Mizuno, and G. M. Rebeiz, "Micromachining for terahertz applications," *IEEE Transactions on Microwave Theory and Techniques*, vol. 46, no. 11, pp. 1821–1831, 1998. [Online]. Available: http://ieeexplore.ieee.org/stamp/stamp.jsp?arnumber=734493 6, 7, 131

[24] J. Nibarger, J. Beall, D. Becker, J. Britton, H.-M. Cho, A. Fox, G. Hilton, J. Hubmayr, D. Li, J. McMahon, M. Niemack, K. Irwin, J. Lanen, and K. Yoon, "An 84 pixel all-silicon corrugated feedhorn for cmb measurements," *Journal of Low Temperature Physics*, vol. 167, no. 3-4, pp. 522–527, 2012. [Online]. Available: http://dx.doi.org/10.1007/s10909-011-0428-z 7, 131

[25] A. Iacono, A. Freni, A. Neto, and G. Gerini, "In-line x-slot element focal plane array of kinetic inductance detectors," in *Antennas and Propagation (EUCAP), Proceedings of the 5th European Conference on*, 2011, pp. 3316–3320. [Online]. Available: http://ieeexplore.ieee.org/stamp/stamp.jsp?arnumber=5782292 8, 131

[26] "IRAM - Institut de Radioastronomie MillimÃľtrique," Available: http://www.iram-institute.org/. 8

[27] N. Llombart, B. Thomas, M. Alonso, C. Lee, G. Chattopadhyay, L. Jofre, and I. Mehdi, "Silicon based antennas for thz integrated arrays," in *Antennas and Propagation (EUCAP), Proceedings of the 5th European Conference on*, 2011, pp. 3176–3179. 9

[28] T. H. Buttgenbach, "An improved solution for integrated array optics in quasi-optical mm and submm receivers: the hybrid antenna," *IEEE Transactions on Microwave Theory and Techniques*, vol. 41, no. 10, pp. 1750–1760, 1993. [Online]. Available: http://ieeexplore.ieee.org/stamp/stamp.jsp?arnumber=247920 9

[29] S. Yates, J. Baselmans, A. Endo, R. Janssen, L. Ferrari *et al.*, "Photon noise limited radiation detection with lens-antenna coupled Microwave Kinetic Inductance Detectors," 2011. 9

[30] S.-K. Lee, M.-G. Kim, K.-W. Jo, S.-M. Shin, and J.-H. Lee, "A glass reflowed microlens array on a si substrate with rectangular through-holes," *Journal of Optics A: Pure and Applied Optics*, vol. 10, no. 4, p. 044003, 2008. [Online]. Available:

http://stacks.iop.org/1464-4258/10/i=4/a=044003 9, 131

[31] A. Cullen and J. C. Parr, "A new perturbation method for measuring microwave fields in free space," *Proceedings of the IEE-Part B: Radio and Electronic Engineering*, vol. 102, no. 6, pp. 836–844, 1955. [Online]. Available: http://ieeexplore.ieee.org/stamp/stamp.jsp?arnumber=5242923 13

[32] J. H. Richmond, "A modulated scattering technique for measurement of field distributions," *IRE Transactions on Microwave Theory and Techniques*, vol. 3, no. 4, pp. 13–15, 1955. 13, 14

[33] G. Hygate and J. F. Nye, "Measuring microwave fields directly with an optically modulated scatterer," *Measurement Science and Technology*, vol. 1, no. 8, p. 703, 1990. [Online]. Available: http://stacks.iop.org/0957-0233/1/i=8/a=006 14

[34] Satimo, "Stargate 64," Available: http://www.satimo.com. 14

[35] A. Joisel, K. J. Bois, A. D. Benally, J.-C. Bolomey, and R. Zoughi, "Embedded modulating dipole scattering for near-field microwave inspection of concrete: preliminary investigations," pp. 208–214, 1999. [Online]. Available: +http://dx.doi.org/10.1117/12.365700 14

[36] J. Bolomey, A. Izadnegahdar, L. Jofre, C. Pichot, G. Peronnet, and M. Solaimani, "Microwave diffraction tomography for biomedical applications," *IEEE Transactions on Microwave Theory and Techniques*, vol. 30, no. 11, pp. 1998–2000, 1982. [Online]. Available: http://ieeexplore.ieee.org/stamp/stamp.jsp?arnumber=1131357 14

[37] M. T. Ghasr, M. A. Abou-Khousa, S. Kharkovsky, R. Zoughi, and D. Pommerenke, "Portable real-time microwave camera at 24 GHz," *IEEE Transactions on Antennas and Propagation*, vol. 60, no. 2, pp. 1114–1125, 2012. 14

[38] J.-C. Bolomey and F. E. Gardiol, *Engineering Applications of the Modulated Scatterer Technique*, A. House, Ed. Artech House, 2001. 14, 131

[39] S. Capdevila, "Rfid multiantenna systems for wireless communications and sensing," Ph.D. dissertation, Universidad Politecnica de Catalunya, 2013. 16, 17

[40] J. C. Bolomey, S. Capdevila, L. Jofre, and J. Romeu, "Electromagnetic modeling of rfid-modulated scattering mechanism. application to tag performance evaluation," *Proceedings of the IEEE*, vol. 98, no. 9, pp. 1555–1569, 2010. 17

[41] S. Capdevila, L. Jofre, J. Romeu, and J. C. Bolomey, "Multi-loaded modulated scatterer technique for sensing applications," *IEEE Transactions on Instrumentation and Measurement*, vol. 62, no. 4, pp. 794–805, 2013. [Online]. Available: http://ieeexplore.ieee.org/stamp/stamp.jsp?arnumber=6469221 17

[42] G. Rebeiz, W. Regehr, D. Rutledge, R. Savage, and J. Luhmann, NevilleC., "Submillimeter-wave antennas on thin membranes," *International Journal of Infrared and Millimeter Waves*, vol. 8, no. 10, pp. 1249–1255, 1987. [Online]. Available: http://dx.doi.org/10.1007/BF01011076 19

[43] Filipovic, S. S. Gearhart, and G. M. Rebeiz, "Double-slot antennas on extended hemispherical and elliptical silicon dielectric lenses," *IEEE Transactions on Microwave Theory and Techniques*, vol. 41, no. 10, pp. 1738–1749, 1993. [Online]. Available: http://ieeexplore.ieee.org/stamp/stamp.jsp?arnumber=247919 19, 64, 65,

71

[44] Ederra, R. Gonzalo, B. Alderman, P. G. Huggard, B. P. de Hon, M. C. Van Beurden, A. Murk, L. Marchand, and P. de Maagt, "Sub-millimeter-wave imaging array at 500 GHz based on 3-D electromagnetic-bandgap material," *IEEE Transactions on Microwave Theory and Techniques*, vol. 56, no. 11, pp. 2556–2565, 2008. [Online]. Available: http://ieeexplore.ieee.org/stamp/stamp.jsp?arnumber=4657393 20

[45] D. Sievenpiper, L. Zhang, R. F. J. Broas, N. G. Alexopolous, and E. Yablonovitch, "High-impedance electromagnetic surfaces with a forbidden frequency band," *IEEE Transactions on Microwave Theory and Techniques*, vol. 47, no. 11, pp. 2059–2074, 1999. [Online]. Available: http://ieeexplore.ieee.org/stamp/stamp.jsp?arnumber=798001 20

[46] M. A. Hickey, M. Qiu, and G. V. Eleftheriades, "A reduced surface-wave twin arc-slot antenna for millimeter-wave applications," *IEEE Microwave and Wireless Components Letters*, vol. 11, no. 11, pp. 459–461, 2001. 20, 66

[47] O. Meide Qiu, G. V. Eleftheriades, and M. Hickey, "A reduced surface-wave twin arc-slot antenna element on electrically thick substrates," in *Antennas and Propagation Society International Symposium, 2001. IEEE*, vol. 3, 2001, pp. 268–271. [Online]. Available: http://ieeexplore.ieee.org/stamp/stamp.jsp?arnumber=960083 20

[48] N. Llombart, "Development of integrated printed array antennas using ebg substrates," Ph.D. dissertation, Universidad Politecnica de Valencia, 2006. 20, 21, 122

[49] A. Neto and N. Llombart, "Wideband localization of the dominant leaky wave poles in dielectric covered antennas," *IEEE Antennas and Wireless Propagation Letters*, vol. 5, no. 1, pp. 549–551, 2006. [Online]. Available: http://ieeexplore.ieee.org/stamp/stamp.jsp?arnumber=4064868 21

[50] R. Rogers and D. Neikirk, "Use of broadside twin element antennas to increase efficiency on electrically thick dielectric substrates," *International Journal of Infrared and Millimeter Waves*, vol. 9, no. 11, pp. 949–969, 1988. [Online]. Available: http://dx.doi.org/10.1007/BF01010768 23

[51] E. G. V. and M. Qiu, "Efficiency and gain of slot antennas and arrays on thick dielectric substrates for millimeter-wave applications: a unified approach," *IEEE Transactions on Antennas and Propagation*, vol. 50, no. 8, pp. 1088–1098, 2002. [Online]. Available: http://ieeexplore.ieee.org/stamp/stamp.jsp?arnumber=1034999 23

[52] J. M. Rius, C. Pichot, L. Jofre, J. C. Bolomey, N. Joachimowicz, A. Broquetas, and M. Ferrando, "Planar and cylindrical active microwave temperature imaging: numerical simulations," *IEEE Transactions on Medical Imaging*, vol. 11, no. 4, pp. 457–469, 1992. 26

[53] L. Jofre, A. Broquetas, J. Romeu, S. Blanch, A. P. Toda, X. Fabregas, and A. Cardama, "UWB tomographic radar imaging of penetrable and impenetrable objects," *Proceedings of the IEEE*, vol. 97, no. 2, pp. 451–464, 2009. 26, 28

[54] C. Balanis, *Advanced Engineering Electromagnetics*, ser. CourseSmart Series. Wiley, 2012. [Online]. Available: http://books.google.es/books?id=cRkTuQAACAAJ 26

[55] R. Harrington, *Time-harmonic electromagnetic fields*, ser. McGraw-Hill electrical and electronic engineering series. McGraw-Hill, 1961. [Online]. Available: http://books.google.es/books?id=FtpPAAAAMAAJ 28

[56] *Ma-com Technology Solutions, PIN Diode Data Sheet*, Available: http://www.macomtech.com/dataSheets/MA4AGBLP912.pdf. 33, 34, 132

[57] "ADS - Advanced Design System," Available: http://www.home.agilent.com/en/pc-1297113/advanced-design-system-ads?&cc=ES&lc=eng. 34

[58] "HFSS - Ansys HFSS Simulation Software," Available: http://www.hfss.com. 41

[59] G. Rebeiz, *RF MEMS: Theory, Design, and Technology*. Wiley, 2004. [Online]. Available: http://books.google.es/books?id=nu2KGmkZ2rwC 52

[60] I. Mehdi, B. Thomas, C. Lee, G. Chattopadhyay, R. Lin, E. Schlecht, A. Peralta, J. Gill, K. Cooper, N. Llombart, and P. Siegel, "Radiometer-on-a-chip: a path toward super-compact submillimeter-wave imaging arrays," pp. 767 105–767 105–9, 2010. [Online]. Available: +http://dx.doi.org/10.1117/12.850229 63, 77

[61] J. W. Britton, J. P. Nibarger, K. W. Yoon, J. A. Beall, D. Becker, H.-M. Cho, G. C. Hilton, J. Hubmayr, M. D. Niemack, and K. D. Irwin, "Corrugated silicon platelet feed horn array for CMB polarimetry at 150 GHz," vol. 7741, 2010. 64

[62] Y. Lankwarden, A. Endo, J. Baselmans, and M. Bruijn, "Development of nbtin-al direct antenna coupled kinetic inductance detectors," *Journal of Low Temperature Physics*, vol. 167, no. 3-4, pp. 367–372, 2012. [Online]. Available: http://dx.doi.org/10.1007/s10909-012-0503-0 64, 107

[63] D. F. Filipovic, G. P. Gauthier, S. Raman, and G. M. Rebeiz, "Off-axis properties of silicon and quartz dielectric lens antennas," *IEEE Transactions on Antennas and Propagation*, vol. 45, no. 5, pp. 760–766, 1997. [Online]. Available: http://ieeexplore.ieee.org/stamp/stamp.jsp?arnumber=575618 64

[64] N. Llombart, A. Neto, G. Gerini, M. Bonnedal, and P. de Maagt, "Impact of mutual coupling in leaky wave enhanced imaging arrays," *IEEE Transactions on Antennas and Propagation*, vol. 56, no. 4, pp. 1201–1206, 2008. [Online]. Available: http://ieeexplore.ieee.org/stamp/stamp.jsp?arnumber=4483601 66, 67

[65] N. Llombart, G. Chattopadhyay, A. Skalare, and I. Mehdi, "Novel terahertz antenna based on a silicon lens fed by a leaky wave enhanced waveguide," *IEEE Transactions on Antennas and Propagation*, vol. 59, no. 6, pp. 2160–2168, 2011. [Online]. Available: http://ieeexplore.ieee.org/stamp/stamp.jsp?arnumber=5751648 67, 68, 70, 73, 74, 75

[66] "CST - Computer Simulation Technology," Available: http://www.cst.com. 68

[67] A. Neto, S. Maci, and P. J. I. de Maagt, "Reflections inside an elliptical dielectric lens antenna," *IEE Proceedings Microwaves, Antennas and Propagation*, vol. 145, no. 3, pp. 243–247, 1998. [Online]. Available: http://ieeexplore.ieee.org/stamp/stamp.jsp?arnumber=710407 72

[68] M. J. M. van der Vorst, P. J. L. de Maagt, and M. H. A. J. Herben, "Effect of internal reflections on the radiation properties and input admittance of integrated lens antennas," *IEEE Transactions on Microwave Theory and Techniques*, vol. 47, no. 9, pp. 1696–1704, 1999. [Online]. Available: http://ieeexplore.ieee.org/stamp/

stamp.jsp?arnumber=788611 72

[69] A. V. Boriskin, R. Sauleau, and A. I. Nosich, "Performance of hemielliptic dielectric lens antennas with optimal edge illumination," *IEEE Transactions on Antennas and Propagation*, vol. 57, no. 7, pp. 2193–2198, 2009. [Online]. Available: http://ieeexplore.ieee.org/stamp/stamp.jsp?arnumber=4907139 76, 102

[70] K. Cooper, R. J. Dengler, N. Llombart, T. Bryllert, G. Chattopadhyay, E. Schlecht, J. Gill, C. Lee, A. Skalare, I. Mehdi, and P. H. Siegel, "Penetrating 3-D imaging at 4- and 25-m range using a submillimeter-wave radar," *IEEE Transactions on Microwave Theory and Techniques*, vol. 56, no. 12, pp. 2771–2778, 2008. [Online]. Available: http://ieeexplore.ieee.org/stamp/stamp.jsp?arnumber=4682606 77

[71] M. J. Griffin, B. M. Swinyard, and L. G. Vigroux, "Spire - herschel's submillimetre camera and spectrometer," pp. 686–697, 2003. [Online]. Available: +http://dx.doi.org/10.1117/12.461152 81

[72] C. Lee, G. Chattopadhyay, K. Cooper, and I. Mehdi, "Curvature control of silicon microlens for THz dielectric antenna," in *Infrared, Millimeter, and Terahertz Waves (IRMMW-THz), 2012 37th International Conference on*, 2012, pp. 1–2. [Online]. Available: http://ieeexplore.ieee.org/stamp/stamp.jsp?arnumber=6380111 100, 101

[73] "Ab millimiter," Available: http://www.abmillimetre.com/. 102

[74] G. Eleftheriades and G. Rebeiz, *Double-Slot Antennas on Extended Hemispherical Silicon Lenses–General Treatment*, ser. University of Michigan Report; RL903 Series. Books on Demand. [Online]. Available: http://books.google.es/books?id=hgw_NgAACAAJ 119

[75] K. Pontoppidan and Ticra, *GRASP9 - Technical Description.* TICRA, 2008. [Online]. Available: http://books.google.es/books?id=ZgRQtwAACAAJ 119, 123

[76] A. Love, "The integration of the equations of propagation of electric waves." *Proceedings of the Royal Society of London*, vol. 68, no. 442-450, pp. 19–21, 1901. 119, 121

[77] C. Balanis, *ANTENNA THEORY: ANALYSIS AND DESIGN, 3RD ED (With CD).* Wiley India Pvt. Limited, 2009. [Online]. Available: http://books.google.es/books?id=ibDCbwAACAAJ 119, 121

[78] N. Llombart and G. Chattopadhyay, "Extended hemispherical silicon lens excited by a leaky wave waveguide feed," in *Antennas and Propagation (EuCAP), 2010 Proceedings of the Fourth European Conference on*, 2010, pp. 1–4. [Online]. Available: http://ieeexplore.ieee.org/stamp/stamp.jsp?arnumber=5504962 122

[79] M. Born, E. Wolf, and A. Bhatia, *Principles of Optics: Electromagnetic Theory of Propagation, Interference and Diffraction of Light.* Cambridge University Press, 1999. [Online]. Available: http://books.google.es/books?id=aoX0gYLuENoC 123

List of Publications

[JA1] M. Alonso-DelPino, N. Llombart, G. Chattopadhyay, C. Lee, C. Jung-Kubiak, L. Jofre, and I. Mehdi, "Design guidelines for a terahertz silicon micro-lens antenna," *Antennas and Wireless Propagation Letters, IEEE*, vol. 12, pp. 84–87, 2013. 63, 93

[JA2] C. Lee, G. Chattopadhyay, C. Jung, T. Reck, K. Cooper, A. Peralta, R. Lin, I. Mehdi, M. del Pino, and N. Juan, "Silicon microlens antenna for multi-pixel thz heterodyne detector arrays," in *Antennas and Propagation (EuCAP), 2013 7th European Conference on*, 2013, pp. 1745–1746.

[JA3] N. Llombart, C. Lee, M. Alonso-delPino, G. Chattopadhyay, C. Jung-Kubiak, L. Jofre, and I. Mehdi, "Silicon micromachined lens antenna for thz integrated heterodyne arrays," *Terahertz Science and Technology, IEEE Transactions on*, vol. PP, no. 99, pp. 1–9, 2013. 93

[JA4] M. Alonso, V. Garg, C. Guerra, J. Romeu, N. Llombart, and L. Jofre, "Real time 100 ghz mst imaging retina," in *Antennas and Propagation (EUCAP), 2012 6th European Conference on*, 2012, pp. 3557–3560.

[JA5] M. Alonso, V. Garg, E. Nova, J. Abril, J. Romeu, N. Llombart, and L. Jofre, "Retina design for 100ghz mst imaging system," in *Antennas and Propagation Society International Symposium (APSURSI), 2012 IEEE*, 2012, pp. 1–2.

[JA6] M. Alonso, V. Garg, J. Romeu, N. Llombart, and L. Jofre, "Tomographic imaging retina at 100 ghz," in *Infrared, Millimeter, and Terahertz Waves (IRMMW-THz), 2012 37th International Conference on*, 2012, pp. 1–2.

[JA7] ——, "Retina design for tomographic imaging at 100 GHz," in *XXVII Simposio de la URSI (Union Cientifica Internacional de Radio) Conference on*, sept. 2012, pp. 1 –2.

[JA8] M. Alonso, C. Guerra, E. Nova, J. Abril, J. Romeu, N. Llombart, and L. Jofre, "100 ghz retina for thz tomographic imaging," in *Infrared, Millimeter and Terahertz Waves (IRMMW-THz), 2011 36th International Conference on*, 2011, pp. 1–2.

[JA9] M. Alonso, N. Llombart, C. Lee, C. Jung, G. Chattopadhyay, L. Jofre, and

I. Mehdi, "Silicon micro-lens antennas for thz integrated arrays," in *Infrared, Millimeter and Terahertz Waves (IRMMW-THz), 2011 36th International Conference on*, 2011, pp. 1–1.

[JA10] L. Jofre, J. Romeu, S. Capdevila, J. Abril, E. Nova, and M. Alonso, "The challenging world of terahertz radiation and imaging," in *Antennas and Propagation (EUCAP), Proceedings of the 5th European Conference on*, 2011, pp. 3470–3475.

[JA11] N. Llombart, B. Thomas, M. Alonso, C. Lee, G. Chattopadhyay, L. Jofre, and I. Mehdi, "Silicon based antennas for thz integrated arrays," in *Antennas and Propagation (EUCAP), Proceedings of the 5th European Conference on*, 2011, pp. 3176–3179. 9

[JA12] M. Alonso, C. Guerra, E. Nova, J. Abril, J. Romeu, N. Llombart, and L. Jofre, "100 GHz retina for THz tomographic imaging," in *XXVI Simposio de la URSI (Union Cientifica Internacional de Radio) Conference on*, sept. 2011, pp. 1 –2.

Master Thesis Supervised

[MA1] V. Garg, "100 GHz MST retina for real time near field imaging," Master's thesis, Universitat Politècnica de Catalunya (UPC), 2008.